Applied Computational Electromagnetics Society

Journal

January 2012
Vol. 27 No. 1

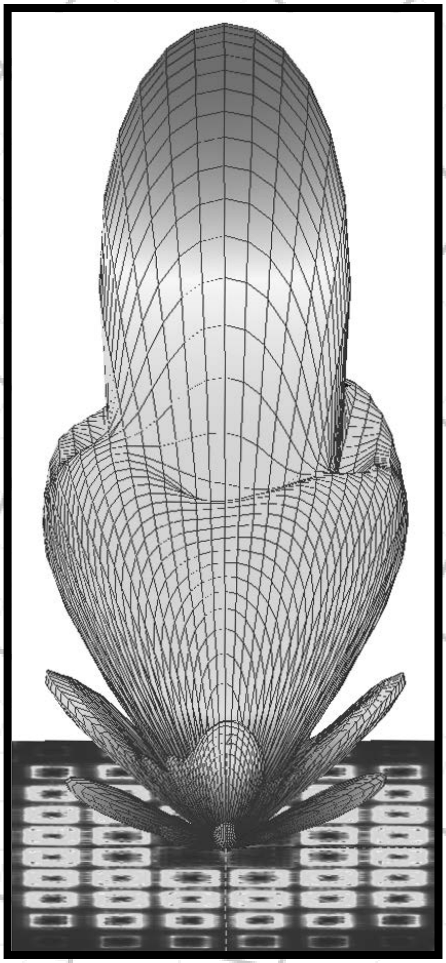

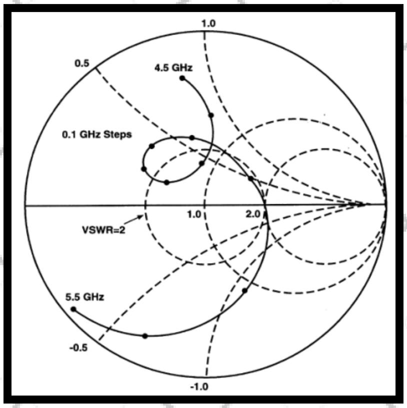

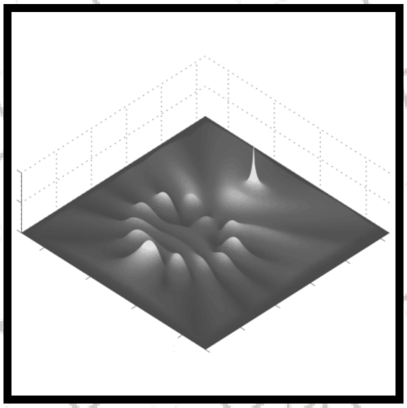

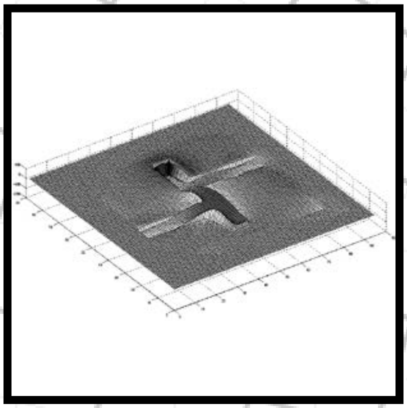

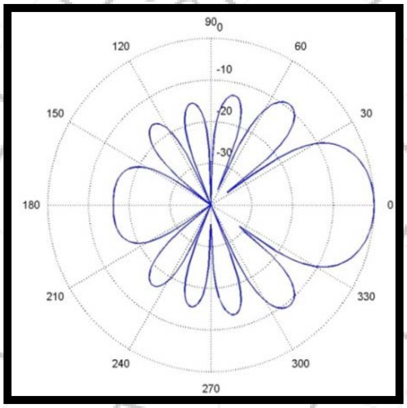

ISSN 1054-4887

GENERAL PURPOSE AND SCOPE: The Applied Computational Electromagnetics Society ***(ACES)*** Journal hereinafter known as the ***ACES Journal*** is devoted to the exchange of information in computational electromagnetics, to the advancement of the state-of-the art, and the promotion of related technical activities. The primary objective of the information exchange is to inform the scientific community on the developments of new computational electromagnetics tools and their use in electrical engineering, physics, or related areas. The technical activities promoted by this publication include code validation, performance analysis, and input/output standardization; code or technique optimization and error minimization; innovations in solution technique or in data input/output; identification of new applications for electromagnetics modeling codes and techniques; integration of computational electromagnetics techniques with new computer architectures; and correlation of computational parameters with physical mechanisms.

SUBMISSIONS: The ***ACES Journal*** welcomes original, previously unpublished papers, relating to applied computational electromagnetics. Typical papers will represent the computational electromagnetics aspects of research in electrical engineering, physics, or related disciplines. However, papers which represent research in applied computational electromagnetics itself are equally acceptable.

Manuscripts are to be submitted through the upload system of ***ACES*** web site http://aces.ee.olemiss.edu See "Information for Authors" on inside of back cover and at ***ACES*** web site. For additional information contact the Editor-in-Chief:

Dr. Atef Elsherbeni
Department of Electrical Engineering
The University of Mississippi
University, MS 386377 USA
Phone: 662-915-5382
Email: atef@olemiss.edu

SUBSCRIPTIONS: All members of the Applied Computational Electromagnetics Society are entitled to access and download the ***ACES Journal*** any published journal article available at http://aces.ee.olemiss.edu. Printed issues of the ***ACES Journal*** are delivered to institutional members. Each author of published papers receives a printed issue of the ***ACES Journal*** in which the paper is published.

Back issues, when available, are $50 each. Subscription to ***ACES*** is through the web site. Orders for back issues of the ***ACES Journal*** and change of address requests should be sent directly to ***ACES*** office at:

Department of Electrical Engineering
The University of Mississippi
University, MS 386377 USA
Phone: 662-915-7231
Email: aglisson@olemiss.edu

Allow four weeks advance notice for change of address. Claims for missing issues will not be honored because of insufficient notice, or address change, or loss in the mail unless the ***ACES*** office is notified within 60 days for USA and Canadian subscribers, or 90 days for subscribers in other countries, from the last day of the month of publication. For information regarding reprints of individual papers or other materials, see "Information for Authors".

LIABILITY. Neither ***ACES***, nor the ***ACES Journal*** editors, are responsible for any consequence of misinformation or claims, express or implied, in any published material in an ***ACES Journal*** issue. This also applies to advertising, for which only camera-ready copies are accepted. Authors are responsible for information contained in their papers. If any material submitted for publication includes material which has already been published elsewhere, it is the author's responsibility to obtain written permission to reproduce such material.

APPLIED COMPUTATIONAL ELECTROMAGNETICS SOCIETY JOURNAL

January 2012
Vol. 27 No. 1
ISSN 1054-4887

The ACES Journal is abstracted in INSPEC, in Engineering Index, DTIC, Science Citation Index Expanded, the Research Alert, and to Current Contents/Engineering, Computing & Technology.

The illustrations on the front cover have been obtained from the research groups at the Department of Electrical Engineering, The University of Mississippi.

THE APPLIED COMPUTATIONAL ELECTROMAGNETICS SOCIETY
http://aces.ee.olemiss.edu

EDITOR-IN-CHIEF

Atef Elsherbeni
University of Mississippi, EE Dept.
University, MS 38677, USA

ASSOCIATE EDITORS-IN-CHIEF

Sami Barmada
University of Pisa. EE Dept.
Pisa, Italy, 56126

Fan Yang
University of Mississippi, EE Dept.
University, MS 38677, USA

Mohamed Bakr
McMaster University, ECE Dept.
Hamilton, ON, L8S 4K1, Canada

Yasushi Kanai
Niigata Inst. of Technology
Kashiwazaki, Japan

Mohammed Hadi
Kuwait University, EE Dept.
Safat, Kuwait

Mohamed Abouzahra
MIT Lincoln Laboratory
Lexington, MA, USA

EDITORIAL ASSISTANTS

Matthew J. Inman
University of Mississippi, EE Dept.
University, MS 38677, USA

Anne Graham
University of Mississippi, EE Dept.
University, MS 38677, USA

EMERITUS EDITORS-IN-CHIEF

Duncan C. Baker
EE Dept. U. of Pretoria
0002 Pretoria, South Africa

Allen Glisson
University of Mississippi, EE Dept.
University, MS 38677, USA

David E. Stein
USAF Scientific Advisory Board
Washington, DC 20330, USA

Robert M. Bevensee
Box 812
Alamo, CA 94507-0516, USA

Ahmed Kishk
University of Mississippi, EE Dept.
University, MS 38677, USA

EMERITUS ASSOCIATE EDITORS-IN-CHIEF

Alexander Yakovlev
University of Mississippi, EE Dept.
University, MS 38677, USA

Erdem Topsakal
Mississippi State University, EE Dept.
Mississippi State, MS 39762, USA

EMERITUS EDITORIAL ASSISTANTS

Khaled ElMaghoub
University of Mississippi, EE Dept.
University, MS 38677, USA

Mohamed Al Sharkawy
Arab Academy for Science and
Technology, ECE Dept.
Alexandria, Egypt

Christina Bonnington
University of Mississippi, EE Dept.
University, MS 38677, USA

JANUARY 2012 REVIEWERS

Ahmed Abdelrahman
Rodolfo Araneo
Manuel Arrebola
Mohamed Bakr
Adalbert Beyer
Toni Bjorninen
Deb Chatterjee
William Coburn
Jorge Costa
Veysel Demir
Yiming Deng
Grant Ellis
Khaled ElMahgoub
Ali Farahbaksh
Randy Haupt
Mousa Hussein
Ashraf Islam
Amir Jafargholi
Shambhu Jha
Yasushi Kanai
Leo Kempel
Fadi Khalil
Ahmed Kishk
Xiuping Li
Zi-Liang Liu
Samir Mahmoud
Anthony Martin
Claudio Montiel
Antonino Musolino
William Palmer
Rui Qiang
Mehdi Salehi
Rolf Schuhmann
Harvey Schuman
Katherine Siakavara
Apirat Siritaratiwat
Fernando Teixeira
Theodoros Tsiboukis
Ahmet Turk
Alexander Yakovlev
Yaxin Yu
Saber Zainud-Deen

THE APPLIED COMPUTATIONAL ELECTROMAGNETICS SOCIETY

JOURNAL

Vol. 27 No. 1 January 2012

TABLE OF CONTENTS

Enhanced Parallel FDTD Method Using SSE Instruction Sets

Lihong Zhang [1, 2], Xiaoling Yang [3], and Wenhua Yu [3]

[1] School of Information Engineering
Communication University of China, Beijing, 100024, China
pzyzlh@yahoo.cn

[2] Fundamentals Department
Chinese People’s Armed Police Force Academy, Langfang Hebei, 065000, China

[3] Penn State University
University Park, PA, 16802, USA
ybob@2comu.com, wxy6@psu.edu

Abstract **─** To accelerate the simulation of the parallel FDTD method, this paper proposes an effective hardware acceleration technique based on the SSE instruction sets, and puts forward a three-level data parallel algorithm based on MPI, OpenMP and SSE instructions. To demonstrate the acceleration effect of this technique, this paper develops two types of codes using C language: one is based on MPI + OpenMP, another is based on MPI + OpenMP + SSE, and then draws a comparison between the computing time of the two types of codes in the numerical experiments for the same electromagnetic radiation problems. The experimental results show that this acceleration technique can achieve an acceleration rate of 2.44 for the ideal case on a PC cluster and 2.37 for the practical problem on a 2-CPU workstation without requiring any extra hardware investment, and provide an efficient and economical technique for the electromagnetic simulations.

Index Terms **─** CPML, FDTD, MPI, OpenMP, and SSE.

I. INTRODUCTION

Finite difference time domain (FDTD) method is firstly proposed by Yee in 1966 [1], and has grown into a relatively complete method system after development through decades. In the FDTD method, the electric (magnetic) field somewhere in space can be calculated by the explicit way through its previous value at the same location and the four magnetic (electric) fields around it at the half time step earlier. The updating equation of magnetic field component along the *z*-axis is given in (1) [2]. The updating equations of the other two components are similar to (1).

$$H_z\Big|^{n+1}_{i+\frac{1}{2},j+\frac{1}{2},k} = D_a\Big|_{i+\frac{1}{2},j+\frac{1}{2},k} H_z\Big|^{n}_{i+\frac{1}{2},j+\frac{1}{2},k} - D_b\Big|_{i+\frac{1}{2},j+\frac{1}{2},k} \left(\frac{E_y\Big|^{n+\frac{1}{2}}_{i+1,j+\frac{1}{2},k} - E_y\Big|^{n+\frac{1}{2}}_{i,j+\frac{1}{2},k}}{\Delta x} - \frac{E_x\Big|^{n+\frac{1}{2}}_{i+\frac{1}{2},j+1,k} - E_x\Big|^{n+\frac{1}{2}}_{i+\frac{1}{2},j,k}}{\Delta y}\right). \quad (1)$$

Compared with other numerical methods, the FDTD method becomes more and more popular for the practical and complex problems because of its simplicity and flexibility. Moreover, the main advantage of the FDTD method is that it is parallel in nature and it can be parallelized more efficiently than finite element method (FEM) or method of moments (MoM) [3]. Therefore, a variety of parallel algorithms have been proposed to reduce the computation time of FDTD electromagnetic simulation[4-5], such as parallel techniques based on message passing interface (MPI) [6] and OpenMP [7]. Recently, a large number of publications have been on the graphic processing unit (GPU) acceleration [8-13].

In this paper, we propose an effective hardware acceleration technique of parallel FDTD simulation using streaming SIMD (single

Submitted On: July 27, 2011
Accepted On: Dec 18, 2011

instruction multiple data) extensions (SSE) instruction sets [14] and develop a 3D parallel FDTD procedure based on C language, MPI library, OpenMP, and SSE instruction sets. The procedure has been validated through an ideal case and a practical problem.

II. SSE INSTRUCTION SETS

Each core in the multi-core processor has its own cache, floating point unit (FPU) and vector arithmetic logic unit (VALU), as shown in Fig. 1. Unlike the FPU, the VALU allows us to operate on four data at the same time. We use the VALU that includes a 128-bit vector unit through the SSE instruction sets to accelerate the parallel conformal FDTD code, as shown in Fig. 2[15].

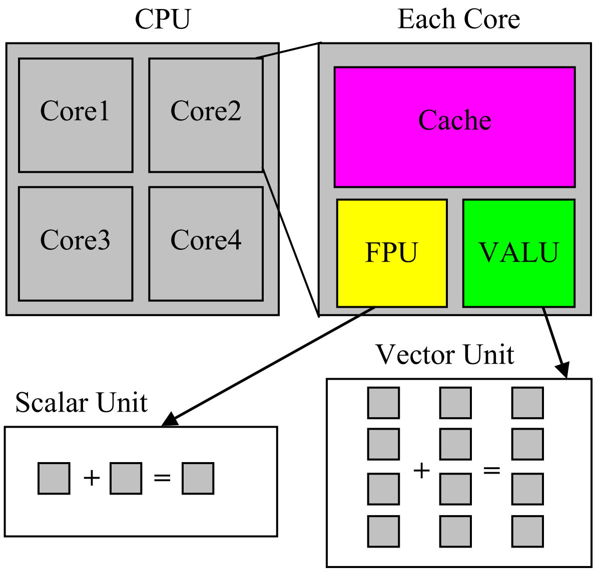

Fig. 1. CPU architecture including FPU and VALU.

SIMD was introduced into the Intel architecture with the MultiMedia eXtensions (MMX) technology. MMX technology allows SIMD computations to be performed on the packed byte, word, and double word integers. The Pentium III processor extended the SIMD computation model with the introduction of the SSE. SSE allows the SIMD computations to be performed on operands that contain four packed single-precision floating-point data elements. The operands can be in memory or in a set of eight 128-bit registers [14]. Figure 3 is a typical SIMD computation procedure.

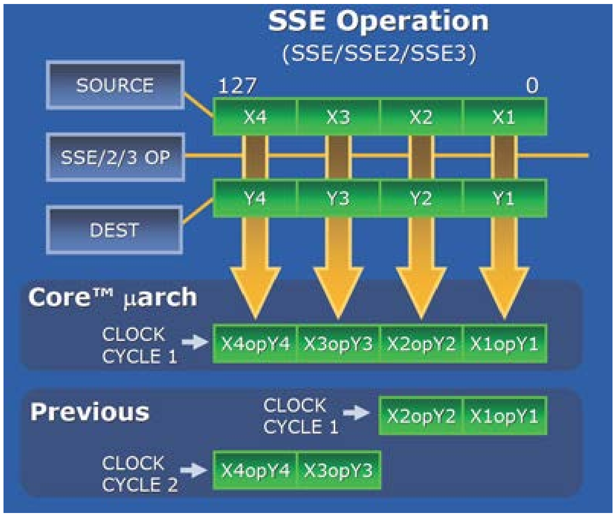

Fig. 2. Concept flowchart in VALU.

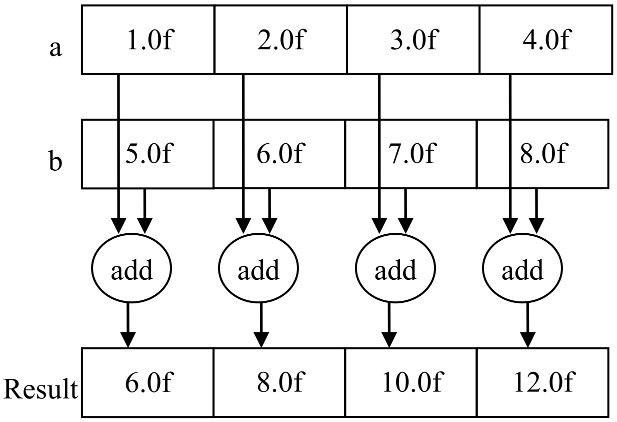

Fig. 3. Flowchart of the SIMD computation.

Recently, Intel Corporation extends previous SIMD offerings (MMX instructions and Intel streaming SIMD extensions) to advanced vector extensions (AVX). The 128-bit SIMD registers for SSE have been expanded to 256 bits. By this mean, SIMD computation procedure works as shown in Fig. 4[16]. Intel AVX is designed to support 512 or 1024 bits in the future.

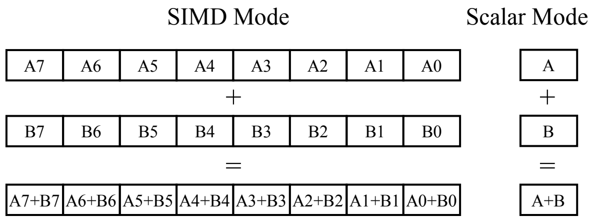

Fig. 4. SIMD computation for AVX.

III. FDTD CODE IMPLEMENTATION

A. FDTD memory allocation

A 3-D array in the FDTD code is allocated using the *malloc* function in C language, and *_aligned_malloc*(*size*, *alignment*) function in this paper. The parameter *size* in this function is the size of the requested memory allocation; the parameter *aligment* is the alignment value and is equal to 16 because that the SSE instruction sets require their memory operands to be aligned to 16-byte (16B) boundaries. For example, if we need a 3-D array *array_name*[*x_size*, *y_size*, *z_size*], we can first define a 1D array *array_name_tmp*[*N*] whose size is *N*=*x_size***y_size***z_size*, and then map the 1-D memory address to 3-D array *array_name*. The pseudo-code segment is demonstrated as below:

```
// allocate the 1-D memory
array_name_tmp = (float*)_aligned_malloc(
   sizeof ( float ) * x_size * y_size * z_size, 16 );
array_name =  ( float *** )_aligned_malloc (
  sizeof ( float** ) * x_size, 16 );
    for( i = 0; i < x_size; i++){
        array_name[i] = ( float ** )_aligned_malloc
            ( sizeof ( float* ) * y_size, 16 );
              for( j = 0; j < y_size; j++){
                 // map the 1-D memory address to 3-D array
            map_address = i * y_size * z_size + j * z_size;
              array_name[i][j] =
  &array_name_tmp[map_address];
          }
    }
```

In the C programming language, the data inside the memory is contiguous in *y*-*z* plane. Suppose that the *y_size* and *z_size* are equal to 8, the data structure of the array *array_name* in the *y*-*z* plane is shown in Fig. 5. The memory addresses of the data elements (0,0,0), (0,0,1)…(0,0,7) is contiguous, likewise, the addresses of (0,1,0), (0,1,1)…(0,1,7) is contiguous too. The address of (0,0,7) is contiguous with the element (0,1,0). When we calculate the electric and magnetic fields in the *y*-*z* plane, we only need to know the address of the first element (supposed to be (0,0,0)) and the total number of elements (supposed to be 64), and then the 64 elements (0,0,0), (0,0,1), (0,0,2)…(0,7,7) are sequentially read in memory. In this case, the memory access is contiguous and therefore the cache hit ratio is relatively high.

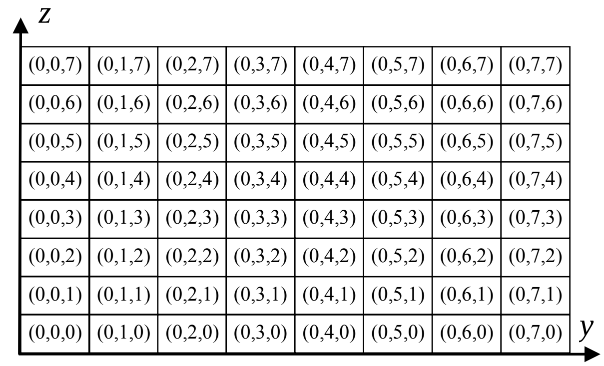

(0,0,7)	(0,1,7)	(0,2,7)	(0,3,7)	(0,4,7)	(0,5,7)	(0,6,7)	(0,7,7)
(0,0,6)	(0,1,6)	(0,2,6)	(0,3,6)	(0,4,6)	(0,5,6)	(0,6,6)	(0,7,6)
(0,0,5)	(0,1,5)	(0,2,5)	(0,3,5)	(0,4,5)	(0,5,5)	(0,6,5)	(0,7,5)
(0,0,4)	(0,1,4)	(0,2,4)	(0,3,4)	(0,4,4)	(0,5,4)	(0,6,4)	(0,7,4)
(0,0,3)	(0,1,3)	(0,2,3)	(0,3,3)	(0,4,3)	(0,5,3)	(0,6,3)	(0,7,3)
(0,0,2)	(0,1,2)	(0,2,2)	(0,3,2)	(0,4,2)	(0,5,2)	(0,6,2)	(0,7,2)
(0,0,1)	(0,1,1)	(0,2,1)	(0,3,1)	(0,4,1)	(0,5,1)	(0,6,1)	(0,7,1)
(0,0,0)	(0,1,0)	(0,2,0)	(0,3,0)	(0,4,0)	(0,5,0)	(0,6,0)	(0,7,0)

Fig. 5. Data structure in the y-z plane.

B. The partition of CPML boundary

The updating equation given in (1) is used to calculate the fields in the computational domain. However, the updating equation inside the PML layers should include two more extra terms, as shown in (2) [2]. The K value inside the computational domain equals to 1, and two Ψ terms in (2) are related to the PML material. Firstly, we update the electric and magnetic fields in the entire domain. We use the SSE instruction sets to load 4 float data into a SSE register at the same time. Secondly, we compute two Ψ terms and update the electric and magnetic fields only in the PML layers. The data division inside the PML layers is shown in Fig. 6.

$$H_z\Big|_{i+\frac{1}{2},j+\frac{1}{2},k}^{n+1} = D_a\Big|_{i+\frac{1}{2},j+\frac{1}{2},k} H_z\Big|_{i+\frac{1}{2},j+\frac{1}{2},k}^{n} - D_b\Big|_{i+\frac{1}{2},j+\frac{1}{2},k} \cdot \left[\begin{array}{l} \dfrac{E_y\Big|_{i+1,j+\frac{1}{2},k}^{n+\frac{1}{2}} - E_y\Big|_{i,j+\frac{1}{2},k}^{n+\frac{1}{2}}}{\mathrm{K}_{x_{i+\frac{1}{2}}}\Delta x} - \dfrac{E_x\Big|_{i+\frac{1}{2},j+1,k}^{n+\frac{1}{2}} - E_x\Big|_{i+\frac{1}{2},j,k}^{n+\frac{1}{2}}}{\mathrm{K}_{y_{i+\frac{1}{2}}}\Delta y} \\ + \Psi_{H_{z,x}}\Big|_{i+\frac{1}{2},j+\frac{1}{2},k}^{n+\frac{1}{2}} - \Psi_{H_{z,y}}\Big|_{i+\frac{1}{2},j+\frac{1}{2},k}^{n+\frac{1}{2}} \end{array} \right] \qquad (2)$$

C. Three-level parallel architecture

The ordinary parallel FDTD code based on the MPI library or OpenMP is the one-level or the two-level parallel technique. In this paper, the FDTD code is the three-level parallel in which SSE is involved.

The first level parallelism is based on MPI in which the computational domain is broken into small sub-domains according to the number of available CPUs or nodes. The field update on the interface of each sub-domain is not independent, namely, the field update on the interface requires the information from its neighbours through the MPI functions. However, the internal field update is independent which results in the high efficient parallel performance.

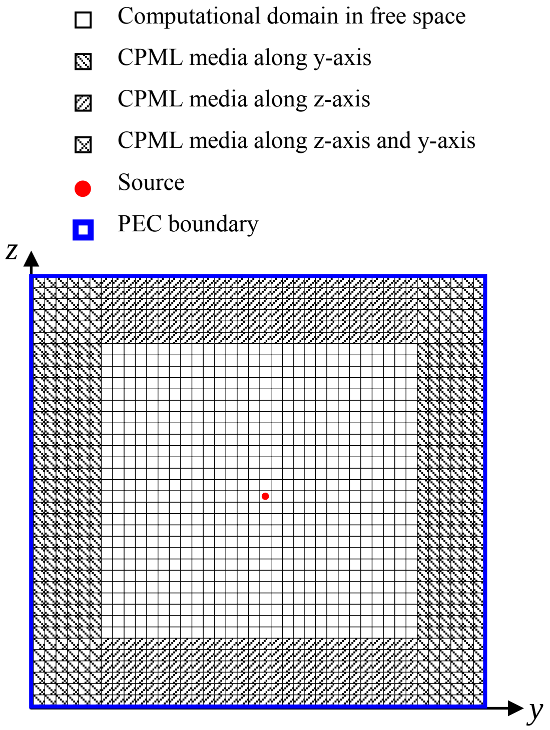

Fig. 6. Division of different regions inside the entire domain.

The second level parallelism is based on OpenMP. In the first place, several threads are generated by OpenMP based on the number of available cores; in the second place, the each thread is assigned to each core for the simulation. The framework of the algorithm is described as follows (In this paper, the parameters *imin* and *imax* are the lowest suffix and largest suffix respectively along *x*-axis of a computational domain; *jmin* and *jmax* are the lowest suffix and largest suffix respectively along *y*-axis; likewise, *kmin* and *kmax* are the lowest suffix and largest suffix respectively along *z*-axis. These six parameters define a cuboid computational domain which will be assigned to core, CPU or node.):

```
#pragma omp parallel private( num_threads, thread_num) {
        thread_num = omp_get_thread_num();
        num_threads = omp_get_num_threads();
        float imaxf = (float)imax / (float)num_threads;
        for ( i = imin + (int)((float)thread_num * imaxf);
           i <= (int)((float)(thread_num + 1) * imaxf);
           i ++) {
               for( j = jmin; j <= jmax; j++){
                for( k = kmin; k <= kmax; k ++ ){
                   //Calculation
                }
            }
        }
}
```

The third level parallelism is based on the SSE instruction sets. As mentioned earlier, ordinary arithmetic operations get one result but the SIMD computations get four results at the same time. This paper will concentrate on the SSE acceleration technique and code implementation.

D. SSE acceleration implementation

We here implement the SSE instruction sets to field update in the FDTD method and the field update inside the PML layers. Due to the data discontinuity inside the memory as shown in Fig. 6, the implementation of SSE inside the PML layer will degrade the performance of SSE. Firstly, we compute the magnetic components in the *z*-axis inside the entire computational domain following steps described below [17-18]:

(1) Define some __m128 variables that SSE requires and assign values to them (as operands of SSE computations);
(2) Load the coefficient into the SSE registers;
(3) Convert the float pointer to the SSE 128 bit pointer;
(4) Unroll the inner loop and reduce the cycle index to one-fourth of original numbers;
(5) Calculate the magnetic fields. The code implementation is described below:

```
// define __m128 variables
__m128 *vhz;
__m128 *vex, *vex_max, *vey, *vey_max;
__m128 vpHi, vpHj;
__m128 vDA = _mm_load1_ps( &DA );
for ( i = imin; i <= imax; i ++){
  // Load coefficient
  vpHi = _mm_load1_ps( &pHi [i] );
  for( j = jmin; j <= jmax; j++){
    // Load coefficient
    vpHj = _mm_load1_ps( &pHj [j] );
    // Convert float pointer to SSE 128 bit pointer
```

```
        vhz = ( __m128 * )hz[i][j];
              vex = ( __m128 * )ex[i][j];
              vex_max = ( __m128 * )ex[i][j+1];
              vey = ( __m128 * )ey[i][j];
              vey_max = ( __m128 * )ey[i+1][j];
              // reduce the cycle index
        for( k = 0, vk = 0; k <= kmax / 4; k += 4, vk++){
       // calculate the magnetic field
         vhz[vk]=_mm_sub_ps(_mm_mul_ps(vDA,vhz[vk]),
         _mm_sub_ps(_mm_mul_ps(vpHi,_mm_sub_ps(vey_max
        [vk],vey[vk])),_mm_mul_ps(vpHj,_mm_sub_ps(vex_max
         [vk], vex[vk]))));
         }
       }
}
```

The update processing of the electric and magnetic fields inside the PML region is similar to those inside the entire computational domain. For example, when we calculate the magnetic field component along *y*-axis in the PML region, we can reference to the steps earlier and the pseudo-code is shown as follows:

```
__m128 *vhx;
__m128 *vez, *vez_max;
__m128 vBeta_PML, vpHj_PML;
__m128 vDB = _mm_load1_ps( &DB );
__m128 *vpusai_hxz;
for ( i = imin; i <= imax; i ++) {
   for( j = jmin_pml; j <= jmax_pml; j++){
      vBeta_PML = _mm_load1_ps(&Beta_PML [j]);
      vpHj_PML = _mm_load1_ps(&pHj_PML [j]);
            vhx = (__m128 *)hx[i][j];
            vez = (__m128 *)ez[i][j];
            vez_max = (__m128 *)ez[i][j+1];
            vpusai_hxz = (__m128 *)pusai_hxz[i][j-jshift];
            for( k = 0, vk = 0; k <= kmax / 4; k += 4, vk++){
        // Calculate Ψ
      vpusai_hxz[vk]=_mm_add_ps(_mm_mul_ps(vBeta_PML
,
     vpusai_hxz[vk]),_mm_mul_ps(vpHj_PML,mm_sub_ps(vez
        _max [vk], vez[vk])));
     // Update the magnetic field in PML domain
        vhx[vk]=_mm_sub_ps(vhx[vk],_mm_mul_ps(vDB,
        vpusai_hxz[vk]));
        }
     }
 }
```

To optimize the procedure and to improve the cache hit ratio, we can combine the calculation of electric and magnetic fields with the treatment of the PML boundary in the following scheme.

```
for ( i = imin; i <= imax; i ++) {
   for( j = jmin; j <= jmax; j++){
            while (vk < vkmax) {
        // calculate the electric or magnetic field
        }
        if ( the value of  j belongs to CPML domain){
         // add the PML boundary
        }
    }
}
```

IV. EXPERIMENTAL RESULTS

To demonstrate the acceleration efficiency by using the SSE instruction sets, we use the FDTD code enhanced with the SSE instruction sets to simulate the simple example that includes only one point source and field distribution output in one surface. The computational domain is separately divided into 40×40×40, 80×80×80, 120×120×120, 160×160×160, and 200×200×200 uniform cells, respectively, and is truncated by a 6-layer CPML. The excitation pulse is taken to be a pure Gaussian pulse and the excitation source is located at the center of the computational domain, as shown in Fig. 6. The numerical experiments were carried out on a PC cluster with Gigabit Ethernet. Every PC of the PC cluster is installed with an Intel Core 2 Duo CPU E7500, 2.93GHz. The experimental results for 600 time steps are summarized in Table 1. We observe from Table 1 that the SSE instruction sets can reduce the computing time of the FDTD simulation. The acceleration factor increases with the growth of the number of cells since the PML region will have less relative contribution to the simulation time when the problem size becomes larger if we fix the number of PML layers to be 6.

The ideal acceleration factor should be 4 since the vector unit based on the SSE instruction sets is four times faster than the floating point unit. However, due to the discontinuous data in the PML boundary, communication between processes and so on, the performance of the code will be reduced. That is to say, without MPI and OpenMP, the performance of the code only based on SSE instruction sets will increase to some extent. In this paper we achieve an acceleration factor of 2.44 when the number of cells is 8 million and a 6-layer PML is applied to truncate the computational domain.

Table 1: Acceleration factor by using SSE instruction sets (Time: Second)

Number Of cells	**Coed Based on**	**Computing time**	**Acceleration factor**
0.064 Mcells	MPI+ OpenMP	3.59	1.65
	MPI+ OpenMp +SSE	2.18	
0.512 Mcells	MPI+ OpenMP	18.21	1.93
	MPI+ OpenMp +SSE	9.45	
1.728 Mcells	MPI+ OpenMP	50.27	2.17
	MPI+ OpenMp +SSE	23.20	
4.096 Mcells	MPI+ OpenMP	110.89	2.36
	MPI+ OpenMp +SSE	46.92	
8 Mcells	MPI+ OpenMP	196.86	2.44
	MPI+ OpenMp +SSE	80.84	

In the practical problems, the simulation factors such as outputs, dispersive media, and near-to-far field transformation will influence the SSE performance due to the discontiguous data structure inside memory. However, it can be improved by optimizing the cache hit ratio.

V. ENGINEERING APPLICATION

In this part, we use the parallel FDTD code accelerated by using the SSE acceleration to simulate a waveguide (WR75) filter problem [19]. The filter includes five cavities and is excited by TE10 mode at one end, as shown in Fig. 7. The output parameter transmission coefficient for the TE10 mode measured at another end. The purpose is to investigate the performance of SSE acceleration on the 2-CPU (16 threads) workstation for the practical problem.

For the sake of comparison, we use the FEM method [20] to simulate the same problem and plot the results in the Fig. 8. It is evident from Fig. 8 to observe the good agreement. It is worthwhile to mention that the results are the same with and without the SSE acceleration.

The parallel FDTD performance with the SSE acceleration is summarized in Table 2. It is observed from Table 2 that the SSE can accelerate the FDTD code 2.37 times for this practical problem.

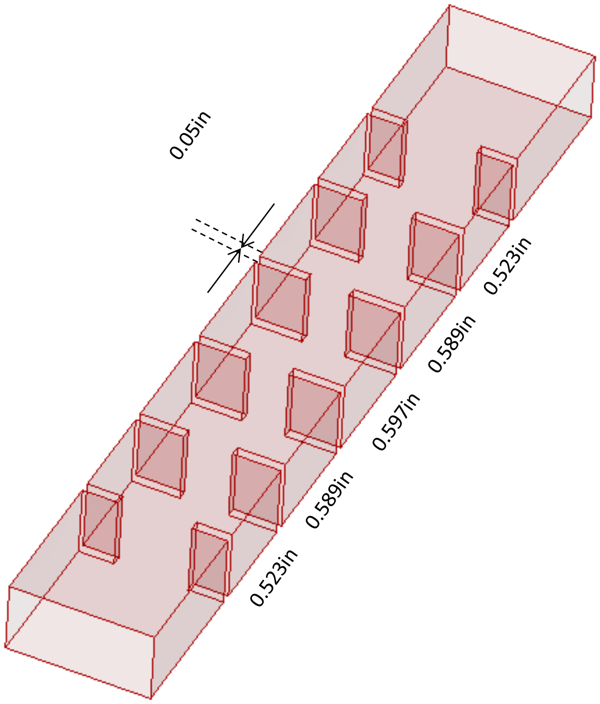

Fig. 7. Configuration of waveguide filter.

VI. CONCLUSION

In this paper, we propose a new hardware acceleration technique based on the SSE instruction sets and gives an implementation on both the PC cluster and workstation platforms. The result shows that this technique can improve the computing efficiency without any extra hardware investment, and provide an efficient and economical technique for the electromagnetic simulations. The further work will be to optimize the data structure inside the memory to further improve the SSE performance and to accelerate the FDTD simulation using AVX.

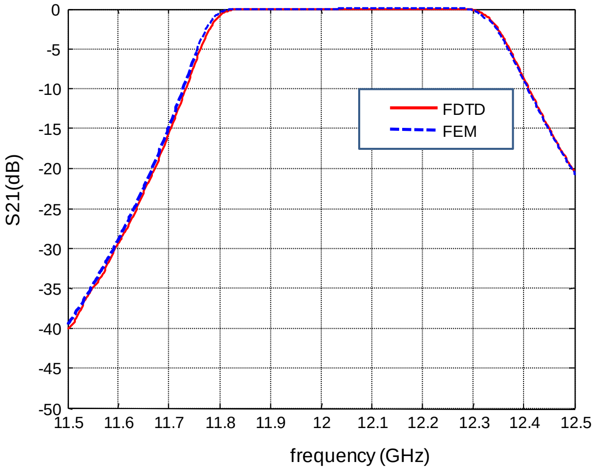

Fig. 8. Transmission coefficient of waveguide filter.

Table 2: Parallel FDTD performance with the SSE acceleration

	FDTD with SSE Acceleration	**FDTD without SSE Acceleration**
Workstation	2×AMD Opteron 6128 2.0GHz	
Memory Usage	37 MB	37 MB
Simulation time	145 sec.	345 sec.

REFERENCES

[1] K. S. Yee, "Numerical Solution of Initial Boundary Value Problems Involving Maxwell´s Equations in Isotropic Media," *IEEE Trans. Antennas Propagat.*, vol. AP-14, pp. 302-307, 1966.

[2] A. Taflove and S. Hagness, *Computational Electrodynamics: The Finite-Difference Time Domain Method*, Artech House, Norwood, May 2005.

[3] W. Yu, R. Mittra, T. Su, et al., *Parallel Finite Difference Time Domain Method*, Communication University of China Press, July, 2005.

[4] W. Yu, et al., "A Robust Parallel Conformal FDTD Processing Package using the MPI Library," *IEEE Antennas and Propagation Magazine*, vol. 47, no. 3, pp. 39-59, June 2005.

[5] Y. Zhang, W. Ding, and C. H. Liang, "Study on the Optimum Virtual Topology for MPI Based Parallel Conformal FDTD Algorithm on PC Clusters," *J. of Electromagn. Waves and Appl.*, vol. 19, no. 13, pp. 1817-1831, 2005.

[6] W. Gropp, E. Lusk, and A. Skjellum, *Using MPI: Portable Parallel Programming with the Message-Passing Interface. 2nd ed.*, MIT Press, Cambridge, Nov., 1999.

[7] https://computing.llnl.gov/tutorials/openMP/

[8] V. Demir and A. Z. Elsherbeni, "Compute Unified Device Architecture (CUDA) based Finite-Difference Time-Domain (FDTD) Implementation," *Applied Computational Electromagnetic Society (ACES) Journal*, vol. 25, no. 4, pp. 303-314, Apr. 2010.

[9] N. Takada, T. Shimobaba, N. Masuda, and T. Ito, "Improved Performance of FDTD Computation using a Thread Block Constructed as a Two-Dimensional Array with CUDA," *Applied Computational Electromagnetic Society (ACES) Journal*, vol. 25, no. 12, pp. 1061-1069, Dec. 2010.

[10] M. Ujaldon, "Using GPUs for Accelerating Electromagnetic Simulations," *Applied Computational Electromagnetic Society (ACES) Journal*, vol. 25, no. 4, pp. 294-302, Apr. 2010.

[11] M. Weldon, L. Maxwell, D. Cyca, M. Hughes, C. Whelan, and M. Okoniewski, "A Practical Look at GPU-Accelerated FDTD Performance," *Applied Computational Electromagnetic Society (ACES) Journal*, vol. 25, no. 4, pp. 315-322, Apr. 2010.

[12] M. J. Inman, A. Z. Elsherbeni, J. G. Maloney, and B. N. Baker, "Practical Implementation of a CPML Absorbing Boundary for GPU Accelerated FDTD Technique," *Applied Computational Electromagnetic Society (ACES) Journal*, vol. 23, no. 1, pp. 16-22, Mar. 2008.

[13] N. Takada, N. Masuda, T. Tanaka, Y. Abe, and T. Ito, "A GPU Implementation of the 2-D Finite-Difference Time-Domain Code using High Level Shader Language," *Applied Compuational Electromagnetic Society (ACES) Journal*, vol. 23, no. 4, pp. 309-316, Dec. 2008.

[14] Intel Corporation, Intel Architecture Optimization Reference Manual, Available: http://www.intel.com/design/pentiumii/manuals/245127.htm.

[15] http://www.tecchannel.de/server/hardware/437111/wechsel_an_der_spitze_intels_neue_core_prozessoren/index9.html

[16] http://software.intel.com/en-us/articles/introduction-to-intel-advanced-vector-extensions/

[17] W. Yu, "A Novel Hardware Acceleration Technique for High Performance Parallel FDTD Method," *Microwave Technology & Computational Electromagnetics (ICMTCE), 2011 IEEE International Conference on*, pp. 441-444, May 2011.

[18] W. Yu, X. Yang, Y. Liu, et al., *Advanced FDTD Methods: Parallelization, Acceleration, and*

Engineering Applications, Artech House, Boston, June 2011.

[19] M. Yu, "Power-Handling Capability for RF Filters," *IEEE Microwave Magazine*, vol. 8, no. 5, pp. 89-97, Oct. 2007.

[20] J. M. Jin, *The Finite Element Method in Electromagnetics*, New York: John Wiley & Sons, 2002.

Lihong Zhang is presently working on her Ph.D. in parallel computing and will graduate next year from Communication University of China. Her research interests include parallel processing techniques, numerical methods and software development.

Xiaoling Yang is a research associate in Material Research Institute of Pennsylvania State University. He received his B.S. and M.S. in Communication and Mathematics from Tianjin University in 2001 and 2004, respectively. He has published three books related to the FDTD method, parallel processing techniques, software development technique, and simulation techniques. He has published over 20 technical papers. His research interests include numerical methods, visual languages and software development.

Wenhua Yu is with 2COMU, Inc. and serves as the president of 2COMU. He was with Pennsylvania State University from 1996 to 2011. He received his Ph.D. in Electrical Engineering from the Southwest Jiaotong University in 1994. He worked at the Beijing Institute of Technology as a Postdoctoral Research Associate from February 1995 to August 1996. He has published six books related to the FDTD method, parallel processing techniques, software development technique, and simulation techniques from 2003 to 2011. He has published over 150 technical papers and four book chapters. He is a senior member of IEEE. His research interests include computational electromagnetic methods, software development techniques, parallel processing techniques, and simulation and design of the antennas, antenna arrays and microwave circuits.

Meshless Radial Basis Functions Method for Solving Hallen's Integral Equation

Sheng-Jian Lai, Bing-Zhong Wang, and Yong Duan

Abstract**—**This paper introduced a meshless method based on radial basis function (RBF) interpolation to solve Hallen's integral equation (HIE) of the thin wire. The unknown current $I_z(z)$ is interpolated by RBF at the center nodes and point matching method is applied to HIE at the collocation nodes. To validate the present method, the input impedance and induced current of dipole antenna are computed with the r^5-RBF and Wu's RBF, respectively. The results show that the present method is a steady numerical approach for solving HIE.

Index Terms**—**Hallen's integral equation, meshless method, point matching method, radial basis functions.

I. INTRODUCTION

In the past several decades, various numerical techniques have been used to solve Hallen's integral equation (HIE) and evaluate electromagnetic field, induced current distribution, and input impedance of thin linear antenna. Mei firstly proposed classical moment method (MOM) to solve HIE [1]. Now, various advanced numerical approaches were applied to HIE, such as high accurate computation[2], hybrid procedure[4], Galerkin's methods [5], high-order numerical solution [6], entire-domain basis functions in Galerkin's methods [7], and some combined algorithm with MOM[3].

The techniques mentioned above are grid-based or mesh-based ones. In recent years, meshfree or meshless methods (MLMs) based on a set of nodes scattering within the problem domain have gained much attention in the engineering communities [8] and significantly developed in the electromagnetic engineering area [9]-[11]. Nicomedes proposed the improve Moving Least Square to solve the combined field integral equation [12]. Galerkin-Bubnov Integral Equation Method [13] was used to solve time-domain HIE. In this paper, we introduce a meshless method based on radial basis function interpolation (MLM-RBF) to solve HIE. RBF interpolation is a powerful technique that was first proposed by Kansa in 1990 to solve partial difference equations (PDEs) [14]. MLM-RBF is a numerical method by which unknown functions of PDEs or integral equations are interpolated at the scattered nodes and point matching method is applied to the equations at the collocation nodes.

Section II describes the MLM-RBF formulation of HIE. It also presents the process of impedance matrix calculation. In Section III, the numerical results using two different RBFs are discussed in detail. Conclusion is given in Section IV.

II. FORMULATION

Figure 1 shows a perfectly conducting long and $\hat{z}$ -oriented thin wire of L in length whose radius R_0 is much less than L and wavelength λ. The HIE of the thin and straight wire can be expressed as [15]

$$E_z^i(z) = \frac{j}{\omega\varepsilon}\left[\frac{\partial}{\partial z^2} + k^2\right]\int_{-L/2}^{L/2} I_z(z')\frac{e^{-jkR}}{4\pi R}dz' \quad (1)$$

where $R = \sqrt{(z-z')^2 + a^2}$ and k represents propagation constant. Through a series of processing steps [15], the above equation can be simplified as

$$\int_{-L/2}^{L/2} I_z(z')\frac{e^{-jkR}}{4\pi R}dz' = D_1 e^{jkz} + D_2 e^{-jkz} + \frac{1}{2\eta}\int_{-L/2}^{L/2} e^{-jk|z-z'|}E_z^i(z')dz' \quad (2)$$

where η is wave impedance, D_1 and D_2 are unknown constants.

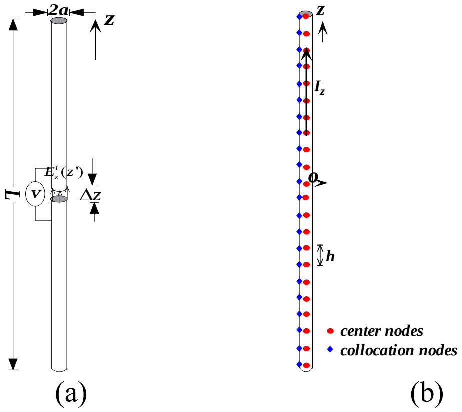

(a) (b)

Fig. 1. Model of thin wire (a) and node distribution (b).

The unknown function I_z in (2) can be interpolated approximately by a series of RBF:

Submitted On: March 10, 2011
Accepted On: Jan 26, 2012

$$I_z(z) \approx \sum_{I=1}^{N} \phi_I(z) a_I = \sum_{I=1}^{N} \phi\left(\left|z - z_I\right|\right) a_I, \quad z \in \left[-L/2, L/2\right] \quad (3)$$

where $\phi_I(\boldsymbol{r})$ is the radial basis function centered at a set of independent points $\boldsymbol{r}_1, \cdots, \boldsymbol{r}_I, \cdots, \boldsymbol{r}_N \in \Omega$ (also called center nodes, see Fig.1 (b)), a_I are unknown coefficients to be computed.

Substituting (3) into (2), we get

$$\sum_{I=1}^{N} a_I \int_{L_I} \phi_I(z') \frac{e^{-jkR}}{4\pi R} dz' = D_1 e^{jkz} + D_2 e^{-jkz} + \frac{1}{2\eta} \int_{-L/2}^{L/2} e^{-jk\left|z - z'\right|} E_z^i(z') dz' \quad (4)$$

where L_I is the integral domain at the center node z_I and $\phi_I(z') = \phi(\left|z' - z_I\right|)$. Then, point-matching method (PMM) is applied to the above equation at a set of collocation nodes $z_1, \cdots, z_J, \cdots, z_M$ ($M \geq N$) (see Fig.1 (b)) which distribute on the wire surface. Thus, we get

$$\sum_{I=1}^{N} a_I \int_{L_I} \phi(\left|z' - z_I\right|) \frac{e^{-jkR_J}}{4\pi R_J} dz' = D_1 e^{jkz_J} + D_2 e^{-jkz_J} + \frac{1}{2\eta} \int_{-L/2}^{L/2} e^{-jk\left|z_J - z'\right|} E_z^i(z') dz' \quad (5)$$

where $R_J = \sqrt{(z_J - z')^2 + a^2}$. The resulting matrix of the above equation is of the form

$$\mathbf{Za} = \left[\mathbf{s}_1, \mathbf{s}_2\right]\left[D_1, D_2\right]^T + \mathbf{b}, \quad (6)$$

where the elements of impedance matrix **Z** are

$$z_{IJ} = \int_{L_I} \phi(\left|z' - z_I\right|) \frac{e^{-jkR_J}}{4\pi R_J} dz', \quad (7)$$

and the vector elements of right-hand side of (6)

$$s_{1J} = e^{jkz_J}, s_{2J} = e^{-jkz_J}$$
$$b_J = \frac{1}{2\eta} \int_{-L/2}^{L/2} e^{-jk\left|z_J - z'\right|} E_z^i(z') dz' \quad (8)$$

A. Calculation of unknown constant D$_1$ and D$_2$

To obtain the unknown vector **a** in (6), the constant D_1 and D_2 should be determined first. This can be done by using the current boundary condition at the ends of the wire, i.e., $I_z(-L/2) = I_z(L/2) = 0$. From(6), we have

$$\mathbf{a} = \mathbf{Z}^{-1}\left[\mathbf{s}_1, \mathbf{s}_2\right]\left[D_1, D_2\right]^T + \mathbf{Z}^{-1}\mathbf{b} \quad (9)$$

Defining $[\mathbf{U}] = [\mathbf{u}_1^T, \mathbf{u}_2^T]$, where $\mathbf{u}_1^T = [1,0,...,0]$ and $\mathbf{u}_2^T = [0,...,0,1]$ and multiplying both sides of (9) by $[\mathbf{U}]^T$, we get

$$\left[\mathbf{U}\right]^T \mathbf{a} = \left[\mathbf{U}\right]^T \mathbf{Z}^{-1}\left[\mathbf{s}_1, \mathbf{s}_2\right]\left[D_1, D_2\right]^T + \left[\mathbf{U}\right]^T \mathbf{Z}^{-1}\mathbf{b} = 0, \quad (10)$$

Solving (10), we get

$$\left[D_1, D_2\right]^T = -\left[\left[\mathbf{U}\right]^T \mathbf{Z}^{-1}\left[\mathbf{s}_1, \mathbf{s}_2\right]\right]^{-1}\left[\mathbf{U}\right]^T \mathbf{Z}^{-1}\mathbf{b} \quad (11)$$

B. Calculation of matrix element

When the collocation node z_J does not locate in the range of the supported domain centered at z_I, the matrix elements of (7) can be computed via an Q-point numerical quadrature [15]:

$$z_{IJ} = \sum_{q=1}^{Q} w_q \phi_I\left(\left|z_{Iq} - z_I\right|\right) \frac{e^{-jkR_{J\_Iq}}}{4\pi R_{J\_Iq}}, \quad I \neq J \quad (12)$$

where $R_{J\_Iq} = \sqrt{(z_J - z_{J\_Iq})^2 + a^2}$.

When z_J locates in the range of the supported domain centered at z_I, as shown in Fig. 2, there exists the quasi-singular integral in (7). To improve the integral accuracy, a very small domain Δ_z centered at z_J is extracted from L_I of (7). Thus, there exist three integral domains in L_I: $[z_I - d_{mI}, z_J - \Delta_z/2]$, $[z_J - \Delta_z/2, z_J + \Delta_z/2]$, and $[z_J + \Delta_z/2, z_I + d_{mI}]$ (see Fig.2), where d_{mI} is the radius of supported domain of RBF centered at z_I. In Δ_z, the integral item $\phi(\left|z' - z_I\right|)$ in (7) is treated as a constant value $\phi(\left|z_J - z_I\right|)$ and the Green's function item is expanded by the small-argument approximation [15]. Thus, (7) in the integral domain Δ_z can be rewritten as:

$$\int_{-\Delta_z/2}^{\Delta_z/2} \phi(\left|z' - z_I\right|) \frac{1 - jkR_J}{4\pi R_J} dz' = \phi(\left|z_J - z_I\right|)\left[\frac{1}{4\pi} \ln\left(\frac{\sqrt{1 + 4a^2/\Delta_z^2} + 1}{\sqrt{1 + 4a^2/\Delta_z^2} - 1}\right) - \frac{jk\Delta_z}{4\pi}\right], I = J \quad (13)$$

In other two domains, (7) is also computed by the Q-point numerical quadrature (12).

Each element in (7) needs to be calculated with the Q-point numerical quadrature, not a simple expression in MOM [15]. Thus, the amount of calculation of MLM-RBF is more than that of MOM in solving HIE.

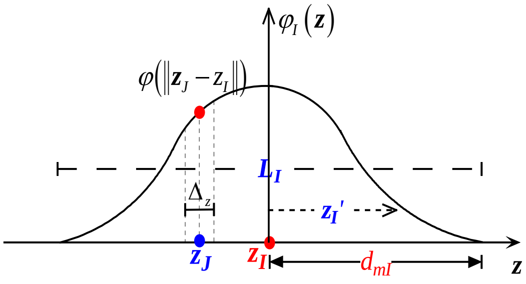

Fig. 2. Collocation node z_J located in the range of the supported domain centered at z_I

From (6), the unknown coefficient vector **a** can be solved. Then substituting **a** into(3), we can get the current distribution of the thin wire.

III. NUMERICAL RESULTS

In order to validate the present method, the input impedance and induced current distribution of a thin wire are calculated by MLM-RBF. Here, a delta-gap source $E_z^i(z') = \delta(z')$ at the center of the wire is adopted, as shown in Fig. 1(a). The length and radius of the wire are set as $L=\lambda/2$ and $a=10^{-3}\lambda$, respectively. Uniform node distribution is adopted on the wire axis and the distance between nodes is h. To analyze the accuracy of the present numerical algorithm, the results of MLM-RBF are compared with those of mesh-based MOM on the condition that the node distribution (grid distribution) is the same. In this work, two different kinds of MOM are taken as referenced methods, which are PMM with pulse basis function and Galerkin's method with triangle basis function. The former is directly used to solve HIE and this process is called Hallen/Pulse approach. The later is used to solve electric field integral equation (EFIE) of arbitrarily shaped thin wired (ATW) model [15] and this process is called ATW/Triangle approach.

There are many different types of RBFs. Here, two typical RBFs are chosen. One is the quintic RBF:

$$\phi_I(\mathbf{r}) = r^5 \tag{14}$$

which is a globally supported RBF without shape parameter. Another is the compactly supported RBF given by Wu [16]:

$$\phi_I(\mathbf{r}) = (1-r)_+^6\left(6+36r+82r^2+72r^3+30r^4+5r^5\right) \tag{15}$$

where $r = \|\mathbf{r}-\mathbf{r}_I\|/d_{mI}$, and

$$(1-r)_+ = \begin{cases} 1-r & 0 \le r \le 1 \\ 0 & other \end{cases} \tag{16}$$

First, we compare the rates of convergence of the input impedance versus the node number by MLM-RBF with those by referenced methods. Figure 3 (a) shows the results of $\mathbf{r}^5$ RBF-based MLM (MLM-r^5-RBF). We can see that, like ATW/Triangle approach, the input impedance of MLM-RBF converges fast to a stable value when the node number is only 12 (i.e. 24 nodes per wavelength). In sharp contrast to r^5-RBF case, the input impedance of the Hallen/Pulse approach converges slowly: more than 200 segments are needed to obtain a good convergence. However, the results of MLM-r^5-RBF could be inaccurate when node number exceeds 90. This is because the condition number of impedance matrix constructed by r^5 RBF is too large (more than 10^{14}) when node number exceeds 90. The r^5 RBF is a power function, its value at the center point is zero. Its conforming impedance matrix is not strictly diagonally dominant matrices that condition number is very large.

In Wu's RBF case (d_{mI}=2.4*h), it can be seen that the input impedance converges more slowly than in r^5 RBF case, but still faster than Hallen/Pulse approach, as shown in Fig. 3 (b). The input resistance computed by Wu's RBF-based MLM (MLM-Wu-RBF) is in good agreement with that by ATW/Triangle approach when node number exceeds 50. For the input reactance of MLM-Wu-RBF, 100 nodes are needed to obtain good convergence results. However, 300 segments are needed for Hallen/Pulse approach. Due to the compactly supported property of Wu's RBF, the generated impedance matrix is strip and sparse. The condition number of the impedance matrix is only 58 when node number reaches 250, which is far less than that of the impedance matrix of r^5 RBF case.

In Wu's RBF case, besides the node number N, there is another parameter d_{mI} to influence the calculation accuracy. Figure 4 shows the input impedance versus d_{mI} of Wu's RBF. From the figure, we can see that the input impedance increases quickly to the peak-value and then decreases slowly as d_{mI} increases. In addition, there exists a range of steady d_{mI} within which the relative errors of peak-value are small. For example, when N=101, the relative error of the peak-value of input resistance is under 1.6% when d_{mI} ranges from 1.8*h to 6*h. From the figure, we can also see that the range of steady d_{mI} widens as the node number increases. General, the d_{mI} parameter of Wu's RBF in HIE is set the 2*h to 5*h that the calculation accuracy is good.

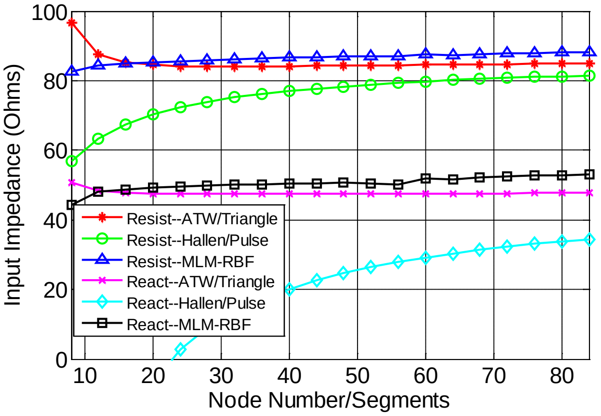

(a) r^5-RBF

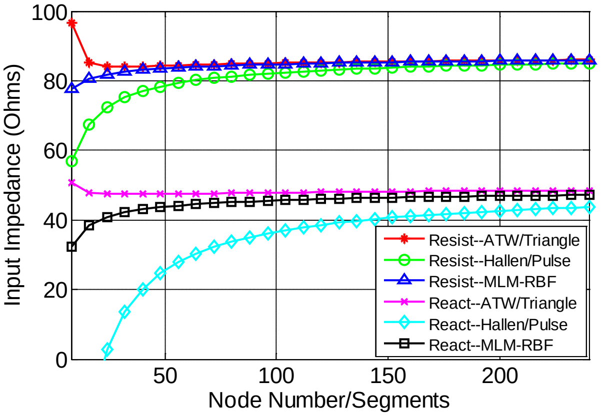

(b) Wu's RBF (d_{mI}=2.4*h)

Fig. 3. Input impedance of a $\lambda/2$ dipole for (a) r^5 RBF and (b) Wu's RBF.

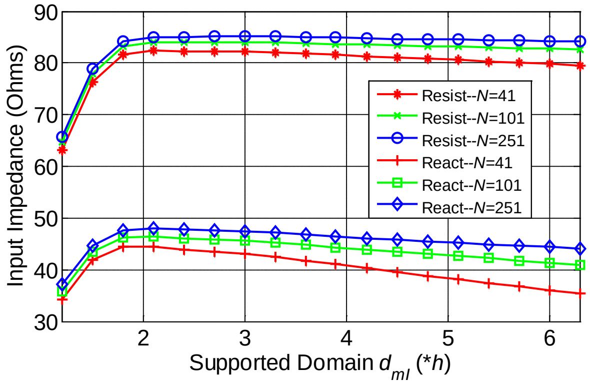

Fig. 4. Input impedance versus supported domain d_{mI} of Wu's RBF.

Then, we compare the induced current distributions between MLM-RBF and reference methods. Figure 5 shows the induced current in r^5 RBF case and induced current versus the d_{mI} in Wu's RBF case when N=41. In r^5 RBF case, the maximum error relative to ATW/Triangle approach at the center node is 4%. In Wu's RBF case, the maximum error at the center node is 8% when d_{mI} ranges from 1.8**h* to 6**h*. When d_{mI}= 2.7**h*, 4.2**h*, and 5.7**h*, the current curves are close to those of ATW/Triangle approach. However, when d_{mI} is not within the steady range (from 1.8**h* to 6**h*), there exist great errors. For example, when d_{mI}= 1.2**h*, the maximum error is 36% at the center node.

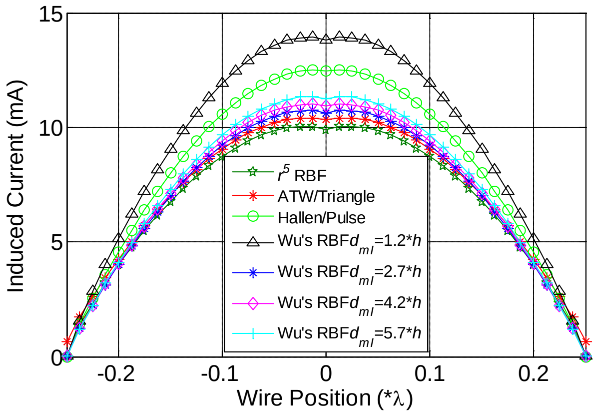

Fig. 5. Induced current distribution on a $\lambda/2$ dipole (node number is 41).

Finally, we consider the generalization of the present method. Taking Wu's RBF for example, we suppose that the d_{mI} is set 2.4**h* and a node number per wavelength is at approximately 15, and then the input impedance versus the dipole length ranging from 0.2λ to 3.5λ is computed; the results are shown in Fig. 6. The results of MLM-Wu-RBF are in good agreement with those of ATW/Triangle approach almost at every data point, which seems to show that MLM-Wu-RBF is a feasible and stable algorithm to solving HIE when d_{mI} is in the steady range.

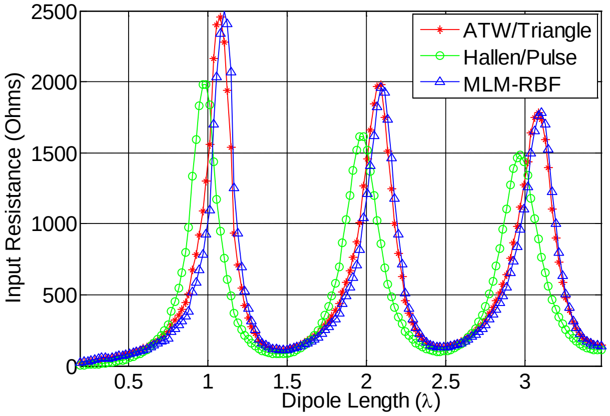

(a) Input Resistance

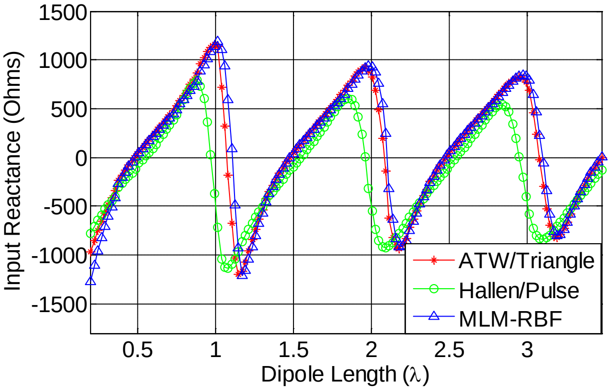

(b) Input Reactance

Fig. 6. Input impedance versus dipole length in Wu's RBF case.

IV. CONCLUSION

In this letter, MLM-RBF is applied to solve HIE of thin wire. The results show that the convergent rates of MLM-RBF are faster than those of MOM. In addition, there exists a steady range of d_{mI} for Wu's RBF within which the results reach certain accuracy. And the steady range of parameter d_{mI} widens as the node number increases. The induced current distributions of r^5 RBF and Wu's RBF within the steady-range parameter d_{mI} are in agreement with the referenced methods. For the r^5 RBF case, the condition number of impedance matrix is too large that some problems cannot be solved. For the Wu's RBF case, when the sample nodes and d_{mI} are set as certain values, the impedances varying with the length of wire are also in agreement with the referenced results, which seems that MLM-RBF can be a general algorithm to computing HIE. But the calculation burden of filling its matrix is somewhat heavier than that of MOM.

REFERENCES

[1] K. K. Mei, "On the Integral Equations of Thin Wire Antennas," *IEEE Trans. Antennas Propag.*, vol. 13, no. 3, pp. 374-378, May 1965.

[2] K. F. A. Hussein, "Accurate Computational Algorithm for Calculation of Input Impedance of Antennas of Arbitrarily Shaped Conducting Surfaces," *Applied*

Computational Electromagnetic Society (ACES) Journal, vol. 22, no. 3, pp. 350–362, November 2007.

[3] R. A. Abd-Alhameed, P. S. Excell, M. A. Mangoud, "Broadband Antenna Response Using Hybrid Technique Combining Frequency Domain MoM and FDTD," *Applied Computational Electromagnetic Society (ACES) Journal,* vol. 20, no. 1, pp. 70–77, Match 2005.

[4] G. Miano, L. Verolino, and V. G. Vaccaro, "A Hybrid Procedure to Solve Hallen's Problem," *IEEE Trans. Electromagn. Compat.,* vol. 38, no. 3, pp. 409-412, Aug. 1996.

[5] G. Fikioris and T. T. Wu, "On the Application of Numerical Methods to Hallen's Equation," *IEEE Trans. Antennas Propag.,* vol. 49, no. 3, pp. 383-392, Mar. 2001.

[6] A. F. Peterson and M. M. Bibby, "High-Order Numerical Solutions of the MFIE for the Linear Dipole," *IEEE Trans. Antennas Propag.,* vol. 52, no. 10, pp. 2684-2691, Oct. 2004.

[7] G. Fikioris and A. Michalopoulou, "On the Use of Entire-Domain Basis Functions in Galerkin Methods Applied to Certain Integral Equations for Wire Antennas with the Approximate Kernel," *IEEE Trans. Electromagn. Compat.,* vol. 51, no. 2, pp. 409-412, May 2009.

[8] G. E. Fasshauer, *Meshfree Approximation Methods with MATLAB*, Singapore: World Scientific Publishing, Chapter 1, 2007.

[9] R. K. Gordon and W. Elliott Hutchcraft, "The Use of Multiquadric Radial Basis Functions in Open Region Problems," *Applied Computational Electromagnetic Society (ACES) Journal,* vol. 21, no. 2, pp. 127–134, July 2006.

[10] S. J. Lai, B. Z. Wang, and Y. Duan, "Meshless Radial Basis Function Method for Transient Electromagnetic Computations," *IEEE Trans. Magn.*, vol. 44, no. 10, pp. 2288–2295, 2008.

[11] X. F. Liu, B. Z. Wang, and S. J. Lai, "Element-Free Galerkin Method for Transient Electromagnetic Field Simulation," *Microwave and Optical Technology Letters,* vol. 50, no. 1, pp. 134-138, Jan. 2008.

[12] W. L. Nicomedes, R. C. Mesquita, and F. J. S. Moreira, "2-D Scattering Integral Field Equation Solution through an IMLS Meshless-Based Approach," *IEEE Trans. Magn.*, vol. 46, no. 8, pp. 2783–2486, 2010.

[13] D. Poljak, B. Jajac, and N. Kovac, "Transient Radiation of a Thin Wire Antenna Buried in a Dielectric Half Space," *Int. Ser. Adv. Boundary Elem.*., vol. 13, pp. 449–456, 2002.

[14] E. J. Kansa, "Multiqudrics - A Scattered Data Approximation Scheme with Applications to Computational Fluid-Dynamics - I Surface Approximations and Partial Derivatives," *Computer Math. Appli.,* vol. 19, pp. 127-145, 1990.

[15] W. C. Gibson, *The method of moments in electromagnetics*, New York: Chapman & Hall/CRC, Chapter 4, 2008.

[16] Z. M. Wu, "Compactly Supported Positive Definite Radial Functions," *Adv. Comput. Math.,* vol. 4, pp. 283-292, 1995.

Two-Step Preconditioner of Multilevel Simple Sparse Method for Electromagnetic Scattering Problems

Xiaoqing Hu, Rushan Chen, Dazhi Ding, Zhenhong Fan, and Yuan Xu

Department of Communication Engineering
Nanjing University of Science and Technology, Nanjing, 210094, China
eerschen@mail.njust.edu.cn

***Abstract* —** In order to efficiently solve the dense complex linear systems arising from electric field integral equations (EFIE) formulation of electromagnetic scattering problems, the multilevel simple sparse method (MLSSM) is used to accelerate the matrix-vector product operations. Because of the nature of EFIE, the resulting linear systems from EFIE formulation are challenging to solve by iterative methods. In this paper, the two-step preconditioner is used to alleviate the low convergence of Krylov subspace solvers, which combine the modified complex shifted preconditioner and sparse approximate inversion (SAI) preconditioner. Numerical examples demonstrate that the two-step preconditioner can greatly improve the convergence of the generalized minimal residual method (GMRES) for the dense complex linear systems and reduce the computationnal time significantly.

***Index Terms* —** Electromagnetic (EM), generalized minimal residual method (GMRES), multilevel simple sparse method (MLSSM), preconditioner.

I. INTRODUCTION

The method of moments (MoM) [1-4] has found widespread application in a variety of electromagnetic problems. The resulting linear systems associated with the discretization of the electric field integral equation (EFIE) are large and dense for electrically large objects in electromagnetic scattering problems. It is basically impractical to solve the EFIE matrix equation using the direct method due to the memory usages of $O(N^2)$ and computational complexity of $O(N^3)$, where N is the number of unknowns. Making such solutions prohibitively expensive for large-scale problems, this difficulty can be circumvented by use of iterative solvers. One of the most popular techniques is the multilevel fast multipole algorithm (MLFMA) [5-6], which has complexity for a given accuracy. The MLFMA has been widely used in recent years to deal with electrically large problems due to its excellent computational efficiency. The multilevel fast far-field algorithm [7] was proposed by L. Rossi in 2000. The adaptive cross approximation method (ACA) is another fast iterative solution algorithm, which was proposed in 2000 by Bebendorf [8]. Similarly, the multilevel UV method has been successfully used to analyze the scattering from rough surfaces [9], propagation over terrain and urban environments, volume scattering from discrete scatterers. As opposed to MLFMA, the ACA and multilevel UV algorithm are purely algebraic and, therefore, do not depend on the Green's function.

The multilevel simple sparse method (MLSSM) was proposed by Canning and Adams [10-11]. Initially, the MLSSM is used to represent the impedance matrix sparsely in fast direct solution [12-14]. Based on the MLSSM, the iterative solution is introduced in [15] for EFIE formulation. It is well-known that EFIE provides a first-kind integral equation, which is ill-conditioned and gives rise to linear systems that are challenging to solve by iterative methods. Although using combined field integral equation (CFIE) can alleviate this difficulty [16], it is not suitable for an object with opened structure. Therefore, it is natural to use preconditioning techniques to improve the condition number of the system and accelerate the convergence rate of iterative solvers before iteration.

There are some simple preconditioners such as the diagonal or diagonal blocks of the coefficient

Submitted On: Nov 10, 2011
Accepted On: Dec 18, 2011

1054-4887 © 2012 ACES

matrix, which can be effective only when the matrix has some degrees of diagonal dominance. Preconditioners based on incomplete LU factorizations have been successfully used on hybrid integral formulations [17], but they are sensitive to indefiniteness in the EFIE matrix, which leads to unstable triangular solvers and very poor preconditioners. Based on the hierarchical matrix, the H-LU preconditioner has been proposed in [18]. The SAI preconditioners are generally less prone to instabilities on indefinite systems [19-21], and outperform more classical approaches such as incomplete LU factorizations. The spectral multigrid and two-step preconditioner are proposed in [22-25], which seem to be efficient to electromagnetic problems.

In order to accelerate the convergence rate of fast iterative solvers of MLSSM, the two-step preconditioner is used in this paper. Firstly, the SAI preconditioner is adopted in the two-step preconditioner. Secondly, the modified complex shifted preconditioner is used to shift the smallest eigenvalues close to one. Numerical experiments demonstrate that the two-step preconditioner of MLSSM is more efficient than SAI preconditioner. Especially, the two-step preconditioner is suitable for multiple right hand vectors problem.

This paper is structured as follows: In Section II, the theory of the MLSSM is outlined. Then, the two-step preconditioner is presented in detail for the efficient solution of the dense linear system in Section III. In Section IV, some numerical results are presented to demonstrate the performance of the two-step preconditioner. Finally, conclusions are presented in Section V.

II. MULTILEVEL SIMPLE SPARSE METHOD OF EFIE

Consider a 3-D arbitrarily shaped perfectly electrically conducting (PEC) object immersed in a medium characterized by permittivity ε and permeability μ. The object is illuminated by an incident wave $\mathbf{E}^i$ that induces current $\mathbf{J}_s$ on the surface *S*. The current $\mathbf{J}_s$ satisfies the electric field integral equation:

$$jk\eta\hat{t}\cdot\int_S \bar{\mathbf{G}}(\mathbf{r},\mathbf{r}')\cdot\mathbf{J}_s(\mathbf{r}')dS' = \hat{t}\cdot\mathbf{E}^i(\mathbf{r}) \ , \tag{1}$$

where

$$\bar{\mathbf{G}}(\mathbf{r},\mathbf{r}') = \left[\bar{\mathbf{I}} + \frac{1}{k^2}\nabla\nabla\right]\frac{e^{-jk|\mathbf{r}-\mathbf{r}'|}}{4\pi|\mathbf{r}-\mathbf{r}'|} \ . \tag{2}$$

The discretization of EFIE with MoM using planar Rao-Wilton-Glisson (RWG) basis functions for surface modeling is presented in [1]. The surface of the object is usually meshed with one-tenth of the wavelength for accuracy. The resulting linear systems from EFIE formulation after Galerkin's testing are briefly outlined as follows:

$$\sum_{n=1}^{N}\mathrm{Z}_{mn}\mathrm{J}_n = \mathrm{V}_m, \qquad m = 1,2,...,N \ , \tag{3}$$

where

$$\mathrm{Z}_{mn} = \frac{jk}{4\pi}\Big(\iint_{S_m}\Lambda_m(\mathbf{r})\cdot\iint_{S_n}\mathrm{G}(\mathbf{r},\mathbf{r}')\Lambda_n(\mathbf{r}')dS'dS - \frac{1}{k^2}\iint_{S_m}\nabla\bullet\Lambda_m(\mathbf{r})\cdot\iint_{S_n}\mathrm{G}(\mathbf{r},\mathbf{r}')\nabla\bullet\Lambda_n(\mathbf{r}')dS'dS\Big) \ , \tag{4}$$

and

$$\mathrm{V}_m = \frac{1}{\eta}\iint_s \Lambda_m(\mathbf{r})\cdot\mathbf{E}^i(\mathbf{r})dS \ . \tag{5}$$

For simplicity, let **Z** denote the coefficient matrix in (3), $\mathbf{J} = \{\mathrm{J}_n\}$ and $\mathbf{V} = \{\mathrm{V}_m\}$ in following. Then, the EFIE matrix equation (3) can be symbolically rewritten as:

$$\mathbf{Z}\bullet\mathbf{J} = \mathbf{V} \ , \tag{6}$$

where **J** is the column vector containing the unknown coefficients of the surface current expansion with RWG basis functions. The impedance matrix **Z** is dense in the sense that all entries are nonzero.

The impedance matrix **Z** resulting from the discretization of EFIE formulation can be represented by the multilevel simply sparse method [14-15] based on a multilevel oc-tree as shown in Fig. 1. In [15], the structure of the MLSSM representation of the impedance matrix **Z** is given in a multilevel recursive manner

$$\mathbf{Z}_l = \hat{\mathbf{Z}}_l + \mathbf{U}_l\mathbf{Z}_{l-1}\mathbf{U}_l^{\mathrm{T}} \ , \tag{7}$$

where $\mathbf{Z}_l$ is the reduced order impedance matrix and consists of only far-field interactions at level $l+1$, which will be compressed in the coarser levels recursively up to level-3. There is no level $L+1$ near-field interaction at the finest level L. Thus, $\mathbf{Z}_L$ is the impedance matrix **Z**. In (7), $\hat{\mathbf{Z}}_l$ is the sparse matrix containing all near-neighbour interactions at level l of the oct-tree which were not represented at the finer level of the tree, $\mathbf{U}_l$ are block diagonal unitary matrices that compress interaction between sources in non-touching groups at level l. The pictorial representation of impedance matrix of EFIE in MLSSM is shown in Fig. 2.

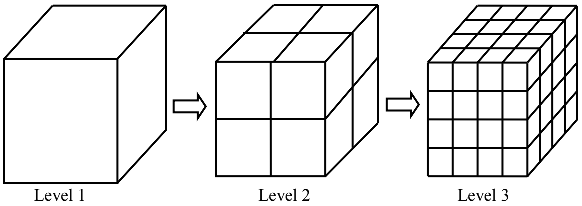

Fig. 1. Construction of an oc-tree.

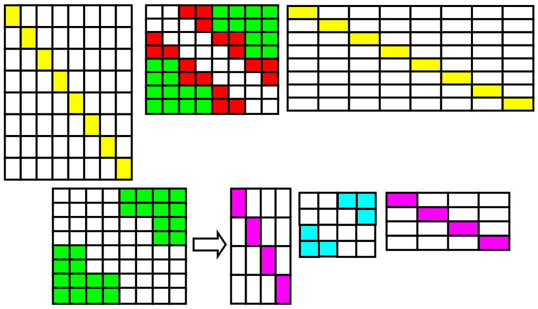

Fig. 2. The pictorial representations of impedance matrix of EFIE in MLSSM.

Based on the MLSSM representation of the impedance matrix **Z**, the efficient matrix vector product (MVP) is implemented as follows:

```
Subroutine MVP ($\mathbf{x}$, $\mathbf{y}$, $l$)
Begin $l = L$: 3: -1
    $\mathbf{y}_1 = \hat{\mathbf{Z}}_l \cdot \mathbf{x}$;
    $\mathbf{y}_2 = (\mathbf{U}_l)^{\mathrm{T}} \cdot \mathbf{x}$;
    Call MVP ($\mathbf{y}_2$, $\mathbf{y}_3$, $l$ -1);
    $\mathbf{y} = \mathbf{y}_1 + \mathbf{U}_l \cdot \mathbf{y}_3$
End
```

III. TWO-STEP PRECONDITIONER

The linear system $\mathbf{Z} \bullet \mathbf{J} = \mathbf{V}$ resulting from EFIE with electromagnetic scattering MLSSM is often an ill-conditioned matrix and results in the low convergence of the Krylov subspace solvers, such as generalized minimal residual method (GMRES) [26]. In linear algebra, the convergence of the Krylov subspace solver is closely related to the condition number of impedance matrix **Z**. Denote the spectrum of **Z** in magnitude by

$$\sigma(\mathrm{Z})=\{|\lambda_1| \le |\lambda_2| \le \cdots \le |\lambda_N|\} \ . \tag{8}$$

Generally speaking, the condition number can be evaluated as follows:

$$\mathrm{cond}(\mathbf{Z}) = |\lambda_N| / |\lambda_1| \ . \tag{9}$$

In order to improve the convergence, the preconditioners are usually incorporated. According to (9), one can conclude that the smallest eigenvalues are responsible for slow convergence. The convergence of Krylov subspace solvers can be accelerated if by any means components in the residuals which correspond to the small eigenvalues can be removed during the iterations.

The SAI preconditioner can improve matrix condition number by clustering most of the large eigenvalues close to one, but leaving a few close to the origin. In [24], the modified complex shifted preconditioner was proposed, which can shift the smallest eigenvalues of impedance matrix **Z** close to a priori fixed constant. Therefore, we adopt the preconditioner in a two-step manner in order to accelerate the convergence of Krylov subspace solvers of MLSSM. Firstly, the SAI preconditioner is used to cluster most large eigenvalues close to one. The EFIE matrix equation (6) is transformed into an equivalent form as follows

$$\mathbf{P}_1\mathbf{Z} \bullet \mathbf{J} = \mathbf{P}_1\mathbf{V} \ , \tag{10}$$

where $\mathbf{P}_1$ is the corresponding SAI preconditioner matrix. Secondly, the modified complex shifted preconditioner is utilized to shift some eigenvalues to one. Then, we obtain the equivalent form as follows

$$\mathbf{P}_2\mathbf{P}_1\mathbf{Z} \bullet \mathbf{J} = \mathbf{P}_2\mathbf{P}_1\mathbf{V} \ , \tag{11}$$

where $\mathbf{P}_2$ is the corresponding modified complex shifted preconditioner matrix. For simplicity, the above combining preconditioner is referred to as two-step preconditioner.

In this paper, the construction of SAI preconditioner matrix $\mathbf{P}_1$ is referred to [21-22]. For the modified complex shifted preconditioner matrix $\mathbf{P}_2$, we have constructed in efficient manners as in [25]

$$\mathbf{P}_2 = \mathbf{I} + \lambda \mathbf{Y}\mathbf{E}^{-1}\mathbf{W}^{\mathrm{H}} \ , \tag{12}$$

where $\mathbf{E} = \mathbf{W}^{\mathrm{H}}\mathbf{Z}\mathbf{Y}$, λ=(1.0,0.0) , **Y** and **W** are rectangular matrices with rank r, which contain r smallest eigenvalues of impedance matrix **Z**.

IV. NUMERICAL RESULTS

In this section, some numerical examples are simulated to demonstrate the efficiency of the two-step preconditioner. All computations are performed on Intel(R) Core(TM) 4 Quad CPU at 2.83 GHz and 8 GB of RAM in single precision. The restarted version of GMRES(m) is applied to solve linear systems, where m is the dimension size of Krylov subspace for GMRES and is set to be 30 in this paper. The iteration process is terminated when the normalized backward error is reduced by 10^{-3} for all examples, and the limit of the maximum number of iterations is set as 10000.

First, we consider the scattering of a perfectly electrically conducting (PEC) sphere with radius 1m at 300 MHz. The incident angles of plane wave are $\theta_i = 0^\circ$, $\phi_i = 0^\circ$. The sets of angles of interest for the bistatic RCS vary from 0 to 180 degree. As shown in Fig. 3, comparison with analytical solution from Mie series is made for the bistatic RCS of the sphere. It can be found that there is an excellent agreement between them and this demonstrates the validation of our MLSSM and the two-step preconditioner.

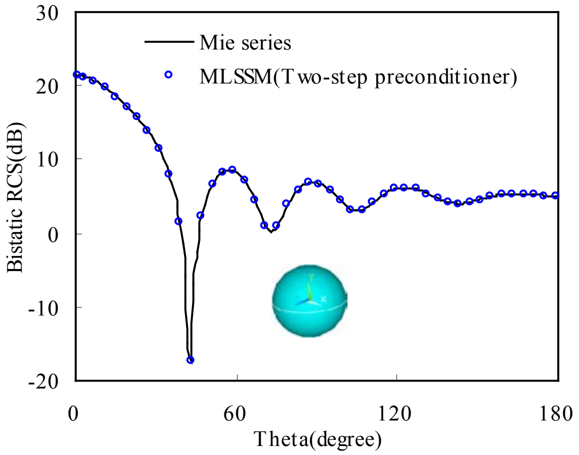

Fig. 3. Calculation results for bistatic RCS of the sphere with radius 1 m at 300 MHz.

Second, we consider a PEC plane as shown in Fig. 4. The length of the plane is 2.04 m in the x-axis direction, and width is 2.02 m in the y-axis direction. The frequency of the incident wave is 1GHz and the incident direction is $\theta_i = 60^\circ$, $\phi_i = 270^\circ$. The surface of the plane is meshed with one-tenth of the wavelength. The unknown of the PEC plane is 18264. The third example considers a VIAS geometry [27] as shown in Fig. 5. The frequency of the incident wave is 100 MHz and the incident direction is $\theta_i = 0^\circ$, $\phi_i = 0^\circ$. The unknown of the VIAS geometry is 15377.

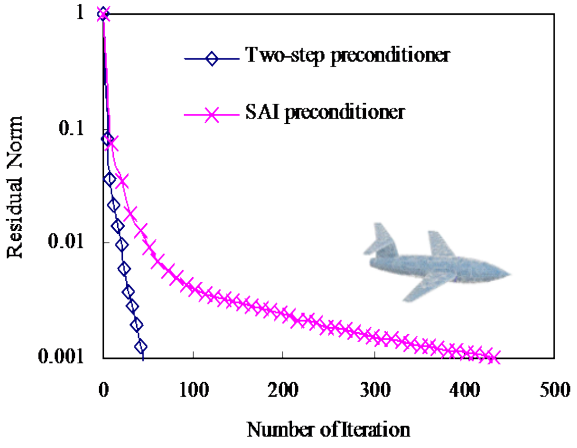

Fig. 4. Convergence history of the GMRES(m) for solving system on the plane.

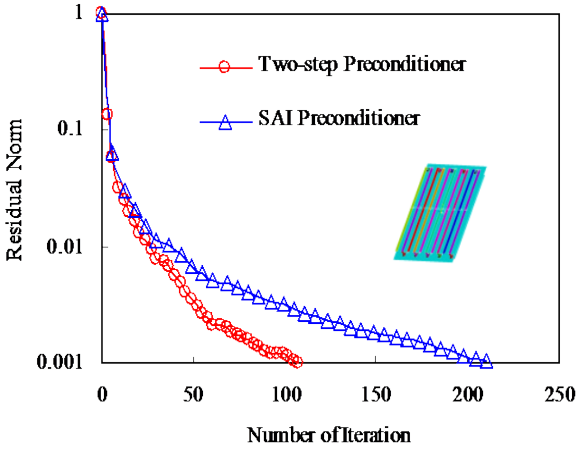

Fig. 5. Convergence history of the GMRES(m) for solving system on the VIAS geometry.

Table 1: Total number of iterations and solution time (in second) for the plane and VIAS geometry

Object	Unknown	Iteration Number		Solution Time	
		SAI	Two-step	SAI	Two-step
Plane	18264	442	44	195 s	22 s
VIAS	15377	215	107	63 s	31 s

The convergence histories of the GMRES algorithms with a two-step preconditioner and SAI preconditioner are displayed in Figs. 4-5 for the above examples. It can be observed that when compared with the SAI preconditioned GMRES (m), the two-step preconditioner can decrease the number of iterations by a factor of 10.0 on the plane case, 2.0 on the VIAS case. The solution times are given in Table 1 for the above examples. It can be seen from Table 1 that a two-step preconditioner can reduce the solution time and iteration number greatly.

In order to illustrate the performance of the two-step preconditioner further, the monostatic RCS of the above PEC sphere is calculated firstly. The interest angles vary from 0° to 180° in ϕ direction when θ_i is fixed at 0°. The error of monostatic RCS of the two-step preconditioner and Mie series is displayed in Fig. 6 for the metallic sphere. It can be seen that the maximum error of the monostatic RCS is less than 0.06 db and this demonstrates the validation of our MLSSM and the two-step preconditioner.

Then, the above plane and VIAS examples are calculated. The interest angles vary from 0° to 180° in ϕ direction when θ is fixed at 0°. The monostatic RCS of the two-step preconditioner and the SAI preconditioner are displayed in Figs. 7-8 for the above examples. The number of iterations is reported for the monostatic RCS calculation in Figs. 9-10.

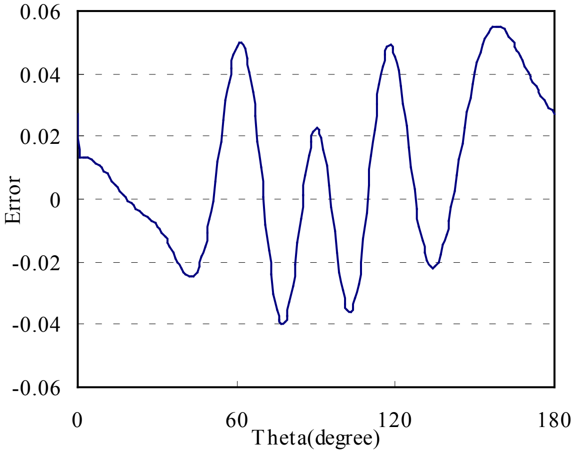

Fig. 6. The error of monostatic RCS of two-step preconditioner and Mie series for the PEC sphere.

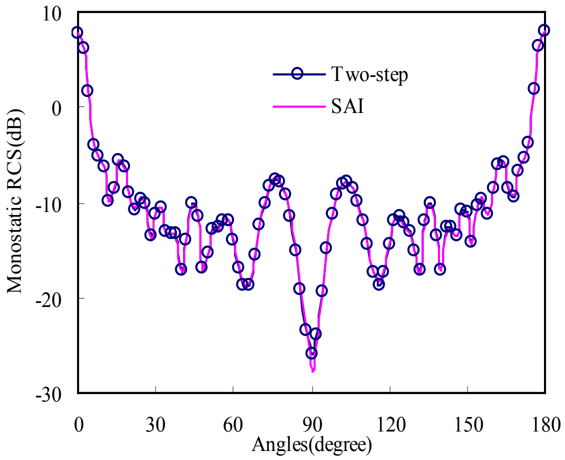

Fig. 7. The monostatic RCS of the PEC plane for $\theta = 0^\circ, 0^\circ \le \phi \le 180^\circ$.

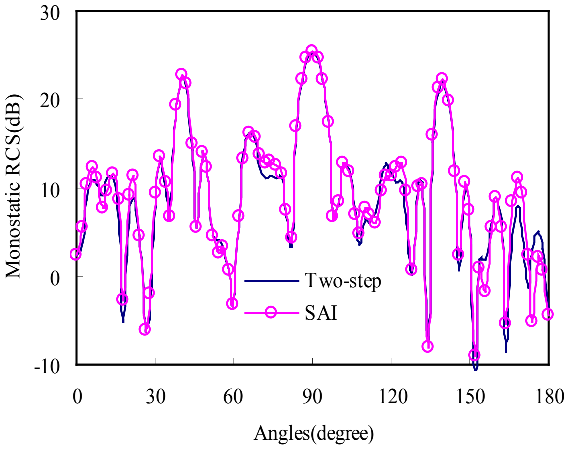

Fig. 8. The monostatic RCS of the PEC VIAS geometry for $\theta = 0^\circ, 0^\circ \le \phi \le 180^\circ$.

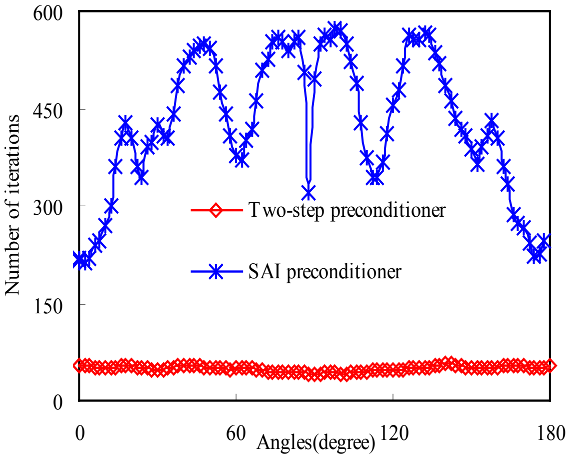

Fig. 9. Number of GMRES iterations for solving monostatic RCS on the plane.

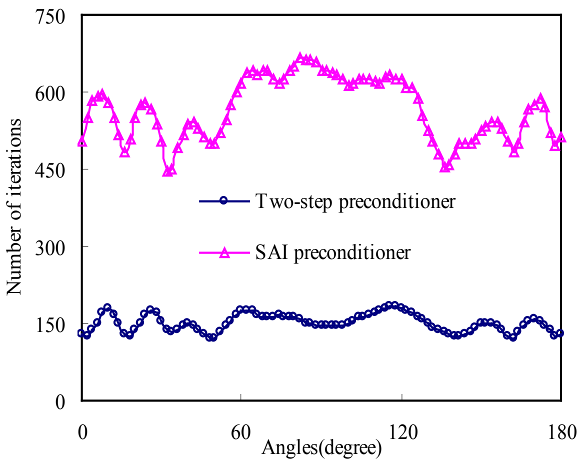

Fig. 10. Number of GMRES iterations for solving monostatic RCS on the VIAS geometry.

From Figs. 9-10, it can be seen that the number of iterations of the SAI preconditioner varies largely with respect to incident angles (i.e. RHS-vectors), while that of the two-step preconditioner is more similar and almost constant for each example. This is the advantage of the two-step preconditioner. Therefore, the two-step preconditioner is suitable for the multiple right hand vectors problem, such as the calculation of the monostatic RCS.

V. CONCLUSION

Because of the nature of the EFIE formulation, the linear system resulting from the electromagnetic scattering MLSSM is often an ill-conditioned matrix and results in the low convergence of the Krylov subspace solvers. In this paper, the two-step preconditioner is used to accelerate the convergence of the Krylov subspace solvers in MLSSM. The numerical examples demonstrate that the two-step preconditioner is more effective than SAI preconditioner in terms of the CPU time in iterative procedure. Especially, the two-step preconditioner is suitable for the multiple right hand vectors problem.

ACKNOWLEDGMENT

We would like to thank the support of Major State Basic Research Development Program of China (973 Program: 2009CB320201), Natural Science Foundation of 60871013, Jiangsu Natural Science Foundation of BK2009387 and NUST 2010ZYTS027.

REFERENCES

[1] S. Rao, D. Wilton, and A. Glisson, “Electromagnetic Scattering by Surfaces of Arbitrary Shape,” *IEEE Trans. Antennas and Propag.*, vol. 30, no. 3, pp. 409-418, May 1982.

[2] K. A. Michalski and D. L. Zheng, “Electromagnetic Scattering and Radiation by Surfaces of Arbitrary Shape in Layered Media, Part I: Theory,” *IEEE Trans. Antennas and Propag.*, vol. 38, no. 3, pp. 335-344, March 1990.

[3] K. A. Michalski and D. L. Zheng, “Electromagnetic Scattering and Radiation by Surfaces of Arbitrary Shape in Layered Media, Part II: Implementation and Results for Contiguous Half-Spaces,” *IEEE Trans. Antennas and Propag.*, vol. 38, no. 3, pp. 345-352, 1990.

[4] D. Ding, J. Ge, and R. Chen, “Well-Conditioned CFIE for Scattering from Dielectric Coated Conducting Bodies above a Half-Space,” *Applied Computational Electromagnetic Society (ACES) Journal*, vol. 25, no. 11, pp. 936 - 946, November 2010.

[5] W. C. Chew, J. M. Jin, E. Michielssen, and J. Song, *Fast Efficient Algorithms in Computa-tional Electromagnetics*, Boston, MA, Artech House, 2001.

[6] J. M. Song, C. C. Lu, and W. C. Chew, “Multilevel Fast Multipole Algorithm for Electromagnetic Scattering by Large Complex Objects,” *IEEE Trans. Antennas Propagat.*, vol. 45, no. 10, pp. 1488-1493, 1997.

[7] L. Rossi, P. J. Cullen, and C. Brennan, “Implementation of a Multilevel Fast Far-Field Algorithm for Solving Electric-Field Integral Equations,” *IEE Proc., Microw. Antennas Propag.*, vol. 147, iss. 1, pp. 19-24, 2000.

[8] M. Bebendorf, “Approximation of Boundary Element Matrices,” *Numer. Math.*, vol. 86, no. 4, pp. 565–589, 2000.

[9] K. L. Lai, L. Tsang, and C. -J. Ong, “Application of the Multilevel UV Method to Analyze Large Microstrip Patch Structures,” *IEEE Antennas Wireless Propag. Lett.*, vol. 4, no. 1, pp. 471-474, 2005.

[10] F. X. Canning and K. Rogovin, “A Universal Matrix Solver for Integral-Equation Based Problems,” *IEEE Antennas and Propagation Magazine*, vol. 45, iss. 1, pp. 16-19, Feb. 2003.

[11] A. Zhu, R. J. Adams, and F. X. Canning: “Modified Simply Sparse Method for Electromagnetic Scattering by PEC,” *IEEE Antennas and Propagation Society Internatio-nal Symposium*, Washington, DC, pp. 427-430, 2005.

[12] R. J. Adams, A. Zhu, and F. X. Canning, “Sparse Factorization of the TMz Impedance Matrix in an Overlapped Localizing Basis, *Progress in*

Electromagnet Research, vol. 61, pp. 291-322, 2006.

[13] Y. Xu, X. Xin, R. J. Adams, S. D. Gedney, and F.X. Canning, "Sparse Direct Solution of the Electric Field Integral Equation using Nonoverlapped Localizing LOGOS Modes," *Micro. Opt. Tech. Lett*., vol. 2, pp. 303-307, Feb. 2008.

[14] Y. Xu, X. Xin, and R. J. Adams, "A Sparse Factorization for Fast Computation of Localizing Modes," *IEEE Trans. Antennas Propagat.*, vol. 58, no. 9, pp. 3044-3049, 20120.

[15] X. Q. Hu, Y. Xu, and R. S. Chen, "Fast Iterative Solution of Integral Equation with Matrix Decomposition Algorithm and Multilevel Simple Sparse Method," *IET Microwaves, Antennas, and Propagation,* vol. 5, no. 13, pp. 1583-1588, Oct. 2011.

[16] J. M. Song, C. C. Lu, and W. C. Chew, "Multilevel Fast Multipole Algorithm for Electromagnetic Scattering by Large Complex Objects," *IEEE Trans. Antennas Propagat.*, vol. 45, no. 10, pp. 1488-1493, 1997.

[17] K. Sertel and J. L. Volakis, "Incomplete LU Preconditioner for FMM Implementation," *Microwave and Optical Technology Letters*, 26(7):265–267, 2000.

[18] T. Wan, R. S. Chen, and X. Q. Hu, "Data-Sparse LU-Decomposition Preconditioning Combined with MLFMM for Electromagnetic Scattering Problems," *IET Microwaves, Antennas & Propagation,* vol. 5, no. 11, pp. 1288-1296, Aug. 2011.

[19] B. Carpentieri, I. S. Duff, L. Griud, and G. Alleon, "Combing Fast Multipole Techniques and an Approximate Inverse Preconditioner for Large Electromagnetism Calculations," *SIAM J. Sci. Comput.*, 27(3):774–792, 2005.

[20] Y. Xie, J. He, A. Sulllvan, and L. Carin, "A Simple Preconditioner for Electric-Field Integral Equations," *Micro. Opt. Tech. Lett.*, vol. 30(1), pp. 51-54, 2001.

[21] J. Lee, J. Zhang, and C. –C. Lu, "Sparse Inverse Preconditioning of Multilevel Fast Multipole Algorithm for Hybrid Integral Equations in Electromagnetics," *IEEE Transactions on Antennas and Propagat.*, vol. 52(9), pp. 2277-2287, 2004.

[22] P. L. Rui, R. S. Chen, D. X. Wang, and E. K. N. Yung, "Spectral Two-step Preconditioning of Multilevel Fast Multipole Algorithm for the Fast Monostatic RCS Calculation," vol. 55, no. 8, *IEEE Transactions on Antennas and Propagation*, August 2007.

[23] P. L. Rui and R. S. Chen, "A Spectral Multigrid Method Combined with MLFMA for Solving Electromagnetic Wave Scattering Problems," *IEEE Transactions on Antennas and Propagation*, September 2007.

[24] D. Z. Ding, R. S. Chen, Z. H. Fan, and P. L. Rui, "AA Novel Hierarchical Two-Level Spectral Preconditioning Technique for Electromag-netic Wave Scattering," *IEEE Transactions on Antennas and Propagation*, vol. 56, no. 4, April 2008.

[25] X. Q. Hu, M. Chen, D. Z. Ding, and R. S. Chen, "A Modified Complex Shifted Preconditiner Combined with Sparse Approximate Inversion Preconditiner for Electromagnetic Scattering," *Micro. Opt. Tech. Lett.*, vol. 53, no. 1, pp. 55-58, January 2011.

[26] Y. Saad and M. Schultz, "GMRES: A Generalized Minimal Residual Algorithm for Solving Nonsymmetric Linear Systems," *SIAM J. Sci. Stat. Comput.*, vol. 7, no. 3, pp. 856-869, 1986.

[27] J. Cheng, S. A. Maloney, R. J. Adams, and F. X. Canning, "Efficient Fill of a Nested Representation of the EFIE at Low Frequencies," *IEEE AP-S International Symposium* San Diego, CA, 2008.

Xiaoqing Hu was born in Hubei province, China. He received the B.S. and M.S. degree in Applied Mathematics from Jilin University, Changchun, China, in 2004 and 2007, respectively. He is currently working toward the Ph.D. degree at Nanjing University of Science and Technology. His research interests include integral equation and its fast methods.

Rushan Chen was born in Jiang-su, China. He received his B.S. and M.S. degrees from the Dept. of Radio Engineering, Southeast University, in 1987 and in 1990, respectively, and his Ph.D. from the Dept. of Electronic Engin-eering, City University of Hong Kong in 2001. Since September 1996, he has been a Visiting Scholar with Department of Electronic Engineering, City University of Hong Kong, first as Research Associate, then as a Senior Research Associate in July 1997, a Research Fellow in April 1998, and a Senior Research Fellow in 1999. From June to September 1999, he was also a Visiting Scholar at Montreal University, Canada. In September 1999, he was promoted to Full Professor and Associate Director of the Microwave & Communication Research Center in NJUST and in 2007, he was appointed Head of the Dept of Communication Engineering, Nanjing

University of Science & Technology. His research interests mainly include microwave/millimeter-wave systems, measurements, antenna, RF-integrated circuits, and computational electro-magnetics. He is a Senior Member of the Chinese Institute of Electronics (CIE). He received the 1992 third-class science and technology advance prize given by the National Military Industry Department of China, the 1993 third class science and technology advance prize given by the National Education Committee of China, the 1996 second-class science and technology advance prize given by the National Education Committee of China, and the 1999 first-class science and technology advance prize given by JiangSu Province as well as the 2001 second-class science and technology advance prize. At NUST, he was awarded the Excellent Honor Prize for academic achievement in 1994, 1996, 1997, 1999, 2000, 2001, 2002, and 2003. He has authored or co-authored more than 200 papers, including over 140 papers in international journals. He is the recipient of the Foundation for China Distinguished Young Investigators presented by the National Science Foundation (NSF) of China in 2003. In 2008, he became a Chang-Jiang Professor under the Cheung Kong Scholar Program awarded by the Ministry of Education, China.

Dazhi Ding was born in Jiangsu, China. He received the B.S. and Ph.D. degrees in electro-magnetic field and microwave technique from Nanjing Univer-sity of Science and Technology (NJUST), Nanjing, China, in 2002 and 2007, respectively. During 2005, he was with the Center of wireless Communication in the City University of Hong Kong, Kowloon, as a Research Assistant. He is currently a Lecturer with the Electronic Engi-neering of NJUST. He is the author or coauthor of over 20 technical papers. His current research interests include computational electromagnetics, electromagnetic scattering and radiation.

Zhenhong Fan was born in Jiangsu, China, in 1978. He received the M.Sc and Ph.D degrees in electromagnetic field and microwave technique from Nanjing University of Science and Technology (NJUST), Nan-jing, China, in 2003 and 2007, respectively. During 2006, he was with the Center of wireless Communication in the City University of Hong Kong, Kowloon, as a Research Assistant. He is currently a Lecturer with the Electronic Engineering of NJUST. He is the author or coauthor of over 20 technical papers. His current research interests include computational electromagnetics, electromagnetic scattering and radiation.

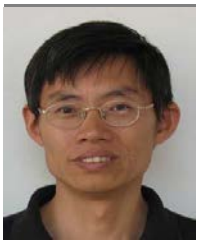

Yuan Xu received the B.S. and M.S. degrees in mathematics from Suzhou University, Suzhou, China, in 1988 and 1991, respectively, and the Ph.D. degree in electrical engineering from Nanjing University of Science and Technology, China, in 2001. He is currently working as a Postdoctoral Scholar at the University of Kentucky, Lexington. His research interest includes computational electromagnetics, integral equation methods, and the analysis of large-scale electromagnetic problems.

A Methodology to Identify Crosstalk Contributor from 6-Line Suspension Assembly Interconnect of Ultra-High Capacity Hard Disk Drives

K. Prachumrasee[1], A. Siritaratiwat[1], V. Ungvichian[2], R. Sivaratana[3], and A. Kaewrawang[1]

[1] KKU-Seagate Cooperation Research Laboratory,
Department of Electrical Engineering, Khon Kaen University, Khon Kaen, 40002, Thailand
krisada.pachumrasee@live.kku.ac.th, apirat@kku.ac.th, arkom@elec.kku.ac.th

[2] EMI Research Laboratory, College of Engineering and Computer Science,
Florida Atlantic University, Boca Raton, FL 33431, USA
ungvich@fau.edu

[3] Seagate Technology (Thailand) Co., Ltd.,
90 Friendship Road, Nakhonratchasima 30170, Thailand
roong.sivaratana@seagate.com

***Abstract* —** The crosstalk phenomenon on the suspension assembly interconnecting trace (SAIT) in hard disk drives (HDD) causes the signal to deform and/or degrade the recording head. For the purpose of analyzing the crosstalk contributions from SAIT using the 3D electromagnetic simulation tool, SAIT is divided into 4 sections which are bend section (BS), far-end section (FS), straight section (SS), and near-end section (NS). The length of each section is selected based on the physical shape of the trace and characteristic impedance. From the results, it was observed that the lowest crosstalk occurs at the BS and the highest crosstalk occurs at the NS. NS is necessary during a HDD quality evaluation and is removed before the SAIT installed in the HDD. With such high crosstalk, the test results can indicate poor head performance even when the head is working properly. Moreover, the crosstalk can be suppressed up to 14 dB and 33 dB for the near-end side and the far-end side, respectively when the NS with a 100% filled stainless steel backing layer is applied to the SAIT. Hence, to improve the accuracy of the recording head test performance, the designer should put more effort to design the SAIT near-end section to minimize crosstalk.

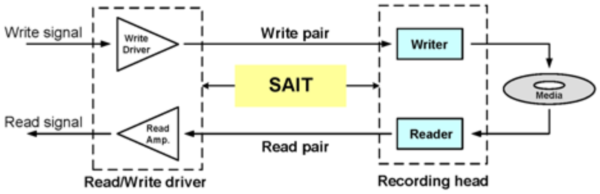

Fig. 1. A diagram of the interconnect links between the recording head and the read/write driver.

***Index Terms* —** Crosstalk, hard disk drive, head gimbal assembly, scattering parameters, suspension assembly interconnecting trace.

I. INTRODUCTION

In the recording head based on tunneling magneto-resistive (TMR) technology, SAIT is used to transfer the data signal between the read/write (R/W) and the recording head, as shown in Fig. 1. To improve the R/W performance in the ultra-high capacity hard disk drive [1], a heating circuit is integrated in the present design. As the result, the space between the traces is made even closer to each other to accommodate the heating lines. Unfortunately, the crosstalk which is an unintended signal from one circuit coupled to the adjacent circuit will increase [2]. The crosstalk

Submitted On: Aug 16, 2011
Accepted On: Jan 26, 2012

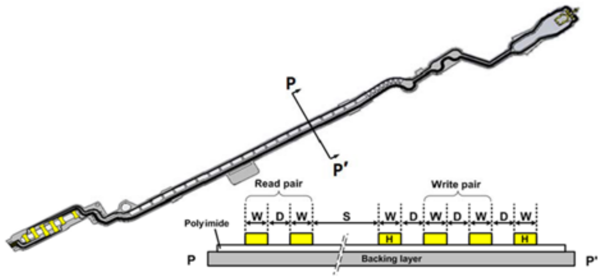

Fig. 2. A 6-trace SAIT 3D model and a cross sectional view along P-P′ plane.

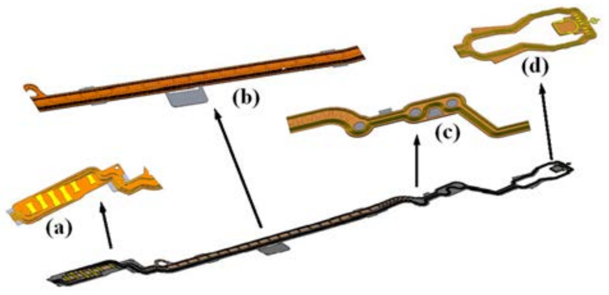

Fig. 3. The 4 sections: (a) NS, (b) SS, (c) BS, and (d) FS.

on the SAIT is reported in [3-10] and the mechanisms are explained in [3 and 11]. Due to the narrow spacing and the TMR recorder's extreme sensitivity, the crosstalk posts more challenges to the SAIT designer.

Before a better SAIT design can be sought, a crosstalk contribution along the trace must be understood. In this paper, a methodology to identify a dominated generating crosstalk portion along the SAIT is proposed. Since the traces along the SAIT structure are non-uniform, one approach is to divide the SAIT according to the physical shape and the characteristic impedance. By using a 3D electromagnetic simulation tool, the scattering parameters (S-parameters) are calculated and the parameters are used to be the crosstalk indicator.

II. THE SUSPENSION ASSEMBLY INTERCONNECTING TRACE STRUCTURE

The 3D model of SAIT, commercially used in the HDD industrial, and the cross section are shown in Fig. 2. It is composed of 3 layers, i.e. the insulator layer, conductor line layer, and backing layer which included polyimide, copper, and stainless steel. The 6 conductive traces consist of a write pair, a read pair, and a heating circuit line (H). The trace width (W), the distance of edge-to-edge between traces (D), and the distance of edge-to-edge between the read trace and the heater trace (S), are 30.5, 30.5, and 535 µm, respectively. The thicknesses of the stainless steel, polyimide, and copper are 20, 10, and 18 µm, respectively. The relative permittivity of polyimide is 3.2, while the conductivity of stainless steel and copper are 1.1×10^{6} S/m and 5.8×10^{7} S/m, respectively [12].

Although the length of SAIT in the 3.5″ HDDs is only 5 cm, the structure and shape of interconnect is complex and non-uniform, as shown in Fig. 2. Therefore, in order to analyze the write-to-read coupling sensitivity of this structure, the SAIT is divided into 4 sections according to the physical structure, that is the near-end section (NS), straight section (SS), bend section (BS), and far-end section (FS), as shown in Fig. 3.

NS includes two read pads, two write pads, and the heating pads. The pads are used during the electrical test of the head gimbal assembly process. It is edged in the hard drive assembly process. For SS, the conductor lines on this section are straight and the write and read pair spacing is kept constant. Around BS, the conductor lines on this section are bent and the write-read pair spacing are varied. FS consists of the read pads, the write pads, and the heating pads connected with the pads on the recording head whereas the spacing between the write-read pair is not constant.

In the cases of a differential line pair, it is characterized by the differential impedance (Z_{diff}). In the SAIT segmentation length, Z_{diff} is selected as the criteria to locate the section-to-section demarcation. The Z_{diff} is the calculating impedance viewing from the left side of each section with a 50-Ω load at the other end. The segment length is determined such that the change of Z_{diff} is less than only 3% hence, the terminal location between two sections has no effect on the crosstalk levels of each section as reported by Hentges [10].

III. THE CROSSTALK PHENOMENON ON THE INTERCONNECT

The electromagnetic coupling mechanisms on the SAIT are reported in [3]. It is the transport of

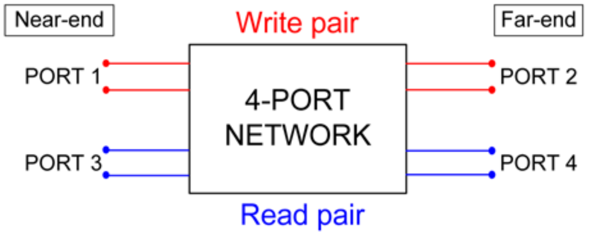

Fig. 4. The 4-port network diagram representing the write and read pairs.

energy from one line to another line via capacitive and inductive couplings which can be expressed by equations (1)-(2).

$$i = C_m \frac{dv}{dt}, \tag{1}$$

$$v = L_m \frac{di}{dt}, \tag{2}$$

where C_m and L_m are mutual capacitance and mutual inductance, v and i are induced voltage and current on the adjacent read line.

In the event of the coupling between the differential line pairs, such as the write-to-read coupling, mutual- capacitance, and inductance of two differential line pairs are represented by the mutual capacitance C_{md} and mutual inductance L_{md}, respectively [13].

The S-parameters are calculated and are utilized as the indicator of energy coupled from the write pair to the read pair due to the crosstalk phenomenon. It has been reported that S-parameters given in (3) give more accurate results at high frequency than other parameters [14].

$$S_{ij}(dB) = 20\log\left(\frac{V_i^-}{V_j^+}\right)\Bigg|_{V_k^+=0 \ \ for \ k \neq j}, \tag{3}$$

where S_{ij} is the transmission coefficient from port j to port i and all remaining ports are terminated in the matched load ($V_k = 0$ for $k \neq j$). The V_i^- is a reflected voltage and V_j^+ is an incident voltage.

Generally, the coupling on the victim line (the read line) is represented by two parameters, i.e. the near-end crosstalk (NEXT) and the far-end crosstalk (FEXT), which is the write-to-read signal coupling observed at the near-end side and the far-end head side of the read lines, respectively. Figure 4 shows the 4-port network diagram. Therefore, NEXT in terms of S_{31} is the ratio between an incident voltage applied at port 1 to a reflected voltage from port 3. Similarly, FEXT in terms of the S parameters is the ratio between an incident voltage applied at port 1 to a reflected voltage from port 4, S_{41}.

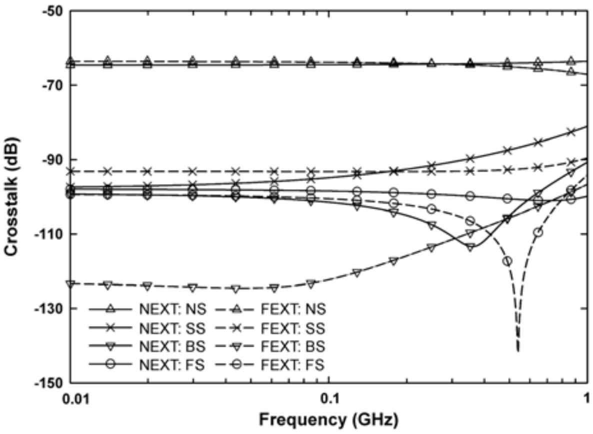

Fig. 5. The NEXT and FEXT of 4-SAIT sections.

IV. THE SIMULATION SETTING

The signal source in the simulation is a Gaussian pulse and it is fed into port 1 of each section. The crosstalk amplitudes based on the S-parameters are both NEXT and FEXT on the read pair and are obtained from CST Microwave Studio [15], which is based on the finite integral technique. The number of cuboids is about 10^6 cells. The operating frequency in this study is 0.01-1.0 GHz, which is compatible with the test procedure in industrial. The boundary condition is set as the magnetic wall for all directions which is recommended for the signal integrity problem [15].

V. RESULTS AND DISCUSSIONS

A. The crosstalk on each SAIT section

The crosstalk levels of 4 portions of SAIT are shown in Fig. 5. It is found that the crosstalk at NE of BS is calculated to be -96 dB, in a frequency range of 10-560 MHz. Also, a very low FEXT of -124 dB is observed in a range of 10-400 MHz. For FS, the crosstalk trace indicates a sharp null of -146 dB at the FE side and occurs around 550 MHz, It might be contributed from the FS acts like the LC resonator of the defected ground structure due to the aperture in the backing layer [16]. While at the NE side, it is almost constant at a level of -99 dB. For BS at NE and FS at FE, it is shown that the crosstalk is in an acceptable range.

Table 1: The self- and mutual- crosstalk parameters of 4 sections at 0.12 GHz

Parameter	Section			
	NS	SS	BS	FS
C_{md} (μF)	0.47700	0.06110	0.00120	0.00923
L_{md} (μH)	0.0256	0.0461	0.1580	0.1030
C_{sd} (pF)	1.360	4.420	1.410	0.871
L_{sd} (μH)	1.290	0.398	1.240	2.580
C_{md}/C_{sd}	351,917.40	13,826.99	7,892.50	10,604.38
L_{md}/L_{sd}	1.99×10^{-5}	1.16×10^{-4}	1.27×10^{-4}	4.01×10^{-5}

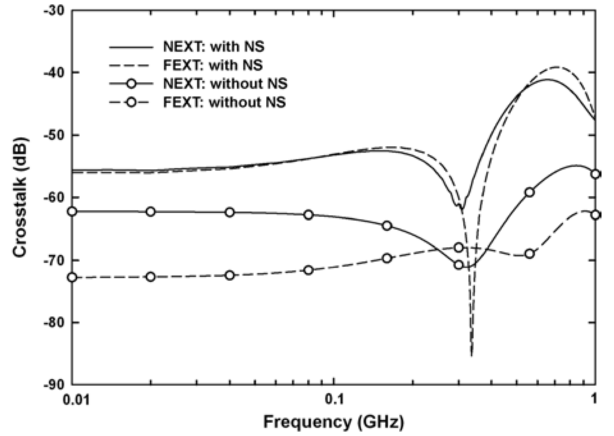

Fig. 6. The crosstalk levels on SAIT in case with and remove NS.

The crosstalk at the NE side of SS is increased with the increasing of frequency and is calculated to be -81.1 dB at 1 GHz, while the crosstalk at FE side is observed as constant at -89.6 dB. For NS, it processes the highest crosstalk of -64.3 dB at NE and -63.9 dB at FE. This can be explained in terms of the spacing between the write and read pair that the narrowing space between the write and read pair possess a stronger coupling and this is in agreement with the result in [13].

This spacing can be represented by C_{md} and the corresponding parameters obtained from the CST are shown in Table 1. NS has the largest C_{md}, and hence, the crosstalk levels are the highest. In addition, it is observed that the crosstalk levels of the portions are correlating to C_{md}/C_{sd} ratio of the induced voltage [17]. The L_{md}/L_{sd} ratio is very small in every section analyzed when compared against the C_{md}/C_{sd} ratio and hence L_{md}/L_{sd} can be neglected. The C_{md}/C_{sd} ratio correlates with the crosstalk level depicted in Fig. 5. In summary, the highest to the smallest crosstalk levels are NS, SS, FS, and BS, respectively.

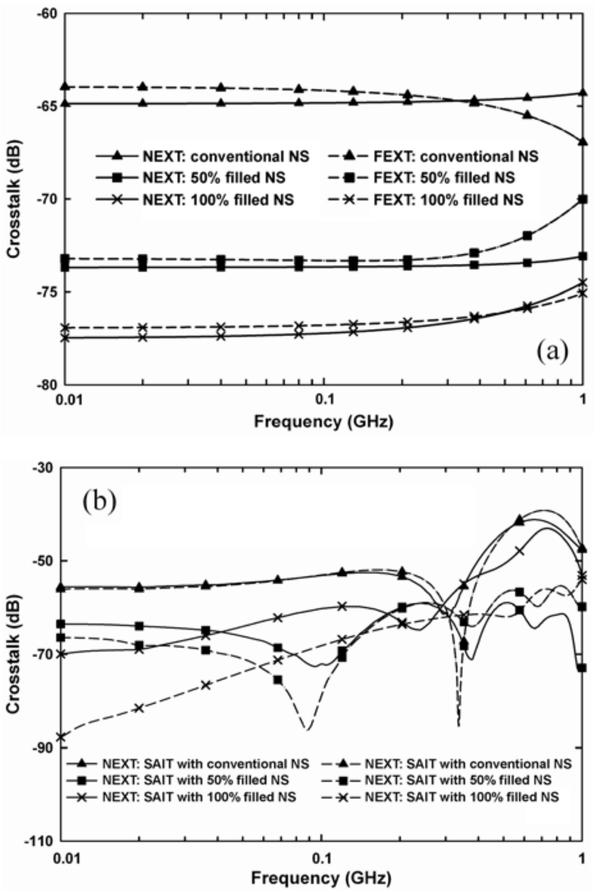

Fig. 7. The crosstalk levels of (a) NS with filled and conventional backing layer and (b) SAIT with filled and conventional NS backing layer.

B. SAIT with and without the near-end section

In industrial practice, NS is removed from SAIT before it is installed in the HDD. However, NS is necessary during the recording head testing processes. There are many test steps where the write-to-read coupling level from the crosstalk can be ascertained. The crosstalk levels with and without NS are compared and are shown in Fig. 6.

From Fig. 6, NEXT and FEXT voltages with NS are higher than SAIT with NS being removed by about 5 dB and 16 dB at 1 GHz, respectively. This is due to the fact that NS is the first section connected to the source in the testing process. The crosstalk levels are higher than SAIT without NS. Hence, a strong crosstalk effect occurred on the SAIT used in the testing process may cause inaccurate test results or totally misinterpreting a recording head performance before being installed in a HDD.

C. The effect of stainless steel filled backing layer of the near-end section

Instead of analyzing using a conventional windowed backing layer at NS, the percentage of stainless steel of backing layer is also used. The crosstalk of the filled percentage and conventional backing layer is compared and is shown in Fig. 7a. The crosstalk levels of the conventional NS are in the range of -64 - -65 dB, while 50% filled and 100% filled are about -74 dB and -77 dB, respectively. This is in agreement with the results described in [10].

The crosstalk levels of the entire SAIT with the filled and conventional backing layer of NS with the conventional, 50% filled with stainless steel, and 100% filled with stainless steel backing layer are shown in Fig. 7b. It can be noticed that at 10 MHz, the NEXT and FEXT of the entire SAIT with 100% filled with stainless steel are suppressed 14 dB and 33 dB, respectively, when compared with the conventional SAIT. In addition, the crosstalk levels of SAIT decreased when the crosstalk levels of NS are also low. Therefore, to avoid the recording head degradation and to improve the performance, the designer must suppress the NS crosstalk.

VI. CONCLUSIONS

The methodology to identify the crosstalk effect on the 6-trace SAIT is proposed. Since the SAIT structure is complex and non-uniform, it is divided into 4 sections according to the physical shape and Z_{diff}. The crosstalk levels represented by *S*-parameters obtained from the commercial software of all sections are enumerated. It is determined that the BS has the lowest crosstalk levels whereas the NS has the highest crosstalk levels. This strong coupling exists at the NS which elevates the crosstalk level of the entire SAIT. Consequently, the presence of the NS may lead to the wrong test results and/or the interpretation of recording head performance. Finally, in order to minimize the crosstalk, the designer should put effort to mitigate crosstalk at the NS.

ACKNOWLEDGMENT

This project is supported by the Thailand Research Fund under the TRF Advanced Scholar Program, No. BRG5280019 and K. Prachumrasee is a PhD candidate granted by the Graduate School, Khon Kaen University under the research fund for high potential student to continue postgraduate study, No 522T201.

REFERENCES

[1] R. Wood, “Future Hard Disk Drive Systems,” *J. Magn. Magn. Mater.*, vol. 321, no. 6, pp. 555-561, Mar. 2009.

[2] C. R. Paul, *Introduction to Electromagnetic Compatibility*, 2nd ed., Wiley & Sons, Inc., USA, pp. 559-712, 2006.

[3] K. B. Klaassen, J. C. L. van Peppen, and X. Xing, “Write-to-Read Coupling,” *IEEE Trans. Magn.*, vol. 38, no. 1, pp. 61-67, Jan. 2002.

[4] Q. He *et al.*, “Write-to-Read Coupling Breakdown in HGA,” *IEEE Trans. Magn.*, vol. 38, no. 5, pp. 2234-2236, Sep. 2002.

[5] E. Jang and X. Zhang, “Write-to-Read Coupling Study of Various Interconnect Type,” *J. Appl. Phys.*, vol. 93, no. 10, pp. 6453–6455, May 2003.

[6] K. W. Carlson, “Crosstalk in the Rigid Disk Drive Channel Front-End,” *IEEE Trans. Magn.*, vol. 40, no. 1, pp. 281-285, Jan. 2004.

[7] X. K. Gao, Q. H. Liu, and Z. J. Liu, “Robust Design of Head Interconnect for Hard Disk Drive,” *J. Appl. Phys.*, vol. 97, no. 10, pp. 10P102, May 2005.

[8] J. D. Pro and M. E. Roen, “Characteristic Impedance and Signal Loss Measurements of Head-to-Preamplifier Interconnects,” *IEEE Trans. Magn.*, vol. 42, no. 2, pp. 261-265, Feb. 2006.

[9] J. T. Contreras, “Modeling of a Disk Drive's Front-End Channel Path,” *IEEE Trans. Magn.*, vol. 42, no. 10, pp. 2600-2602, Oct. 2006.

[10] R. T. Hentges, J. D. Pro, M. E. Roen, G. J. VanHecke, and G. H. Kimball, “Exploring Low Loss Suspension Interconnects for High Data Rates in Hard Disk Drives,” *IEEE Trans. Magn.*, vol. 44, no. 1, pp. 169-174, Jan. 2008.

[11] O. Ramahi, “Analysis of Conventional and Novel Delay Lines: A Numerical Study,” *J. Appl. Comput. Electromagn. Soc.*, vol. 18, no. 3, pp. 181-190, Nov. 2003.

[12] E. Jang, “Three-Dimension Electromagnetic Analysis of Hard Disk Drive Suspension Interconnect with Periodic Aperture in Reference Plane,” *J. Appl. Phys.*, vol. 105, no. 7, pp. 07C128, Apr. 2009.

[13] F. D. Mbairi, W. P. Siebert, and H. Hesselbom, “High-Frequency Transmission Lines Crosstalk Reduction using Spacing Rules,” *IEEE Trans. Compon. Packag. Technol.*, vol.31, no. 3, pp. 601-610, Sep. 2008.

[14] D. M. Pozar, *Microwave Engineering,* 3rd ed., Wiley & Sons, Inc., USA, 2005, pp. 174-183.

[15] CST GmbH, Germany, CST Microwave Sudio, 2010.

[16] D. Ahn *et al.*, “A Design of the Low-Pass Filter using the Novel Microstrip Defected Ground Structure,” *IEEE Trans. Micro. Theo. And Tech.*, vol. 49, no.1, pp. 86-93, Jan. 2001.

[17] T. R. Haller, B. S. Whitmore, P. J. Zabinski, and B. K. Gilber, “High Frequency Performance of GE High-Density Interconnect Modules,” *IEEE Trans. Compon., Hybrids, Manuf. Technol.*, vol. 16, no. 2, pp. 21-27, Feb. 1993.

Krisada Prachumrasee is a Ph.D. candidate after he obtained B. Eng. (EE) and M. Eng. (EE) from Khon Kaen Uiversity. He was granted the M. Eng. Scholarship from the Industrial/University Cooperative Research Center in HDD Component (I/U CRC in HDD Component) supported by the Ministry of Science and Technology. With good performance thesis of his Master degree study, he has received a PhD scholarship from Graduate School, Khon Kaen University under the research fund for high potential student to continue postgraduate study.

Apirat Siritaratiwat received his B.Eng. (EE) from Khon Kaen University in 1992. After working in the industry for few years, he joined the Department of Electrical Engineering, Khon Kaen University in 1994 and continued his postgraduate study at the University of Manchester, UK, between 1995-1999. He has served in many managerial positions such as Head of Department, Assistant to President for Research Affairs etc. He has done researches in HDD and been one of pioneer researchers of ESD/EOS and EMI in recording heads. Since his researches are mainly jointed with HDD industry, it leaded to the establishment of the KKU-Seagate Cooperation Research Laboratory and the I/U CRC in HDD Component where he was Director. He has published more than 80 articles and held 4 pending patents.

Vichate Ungvichian was born in Bangkok, Thailand. He received his Ph.D. degree in Electrical Engineering specialized in Electromagnetic from the Ohio University, Athens, Ohio, in 1981.

Since 1982, he has been with the Department of Electrical & Computer Engineering and Computer Science, Florida Atlantic University, Boca Raton, Florida, USA. He is a Full Professor and in the past 28 years as the Director of the EMI Lab.He is a senior member of IEEE, Advisor of IEEE FAU Student Chapter and Advisor of τβπ Engineering Honor Society.

Roong Sivaratana earned his B.Eng. from KMUT, North Bangkok, and M. Eng. From Warick University, UK. He has been Senior Director at Seagate for years and emphasized on Test Engineering and Development. He has published papers with academia and advised postgraduate students in his expertise area of HDD development.

Arkom Kaewrawang obtained his B. Eng. (EE), Horn, from Khon Kaen University, M. Eng. (EE) from Chulalongkorn University, and Ph.D. from Shinshu University, Japan. He has done researches with HDD industry in the area of magnetic materials and high frequency effects to recording heads. He has published more than 20 international articles with many outstanding awards from various sources.

Capacitance Value Control for Metamaterial Reflectarray using Multi-layer Mushroom Structure with Parasitic Patches

Tamami Maruyama, Tatsuo Furuno, Yasuhiro Oda, Jiyun Shen, and Tomoyuki Ohya

NTT DOCOMO, Inc., 3-5 Hikari-no-oka, Yokosuka, Kanagawa 239-8536 Japan
maruyamatam@nttdocomo.co.jp, furuno@nttdocomo.com, oday@nttdocomo.co.jp,
shink@nttdocomo.co.jp, ooyat@nttdocomo.co.jp

Abstract **─** A mushroom-structure reflectarray can be designed by setting the values of inductance *L* and capacitance *C* based on *LC* resonant circuit theory. Since the capacitance value is determined by the gap size of mushroom patches and the range of the gap size is limited by the manufacturing process, it is difficult to adjust the capacitance value to achieve the desired reflection phase for the reflectarray design. To address this issue, this paper proposes introducing multi-layer parasitic patches on the mushroom structure and controlling the capacitance values using the number of parasitic layers based on the parallel resonant circuit theory. This paper also proposes a novel design method for mushroom reflectarrays when the incident electric field and beam control direction of the scattered waves are set parallel by focusing on the capacitance value. We measure reflected and scattered waves in an anechoic chamber. The measurement results of the direction of the reflected wave are shown compared to the results of the theoretical and simulation analyses.

Index Terms **─** Artificial magnetic conductors (AMC), high impedance surface (HIS), *LC* resonant circuit model, metamaterial, multi-layer mushroom, mushroom-like structure, reflectarray.

I. INTRODUCTION

Recently, the study and standardization of very high-speed (beyond 2 Gbps) wireless communication systems [1] have progressed. By using high frequency radio waves, we can allocate a sufficient bandwidth to achieve high data transmission rates in these systems. The coverage area however, becomes smaller when using a high frequency because the propagation loss increases due to diffraction, and this leads to difficulty in using high frequencies in mobile communications. In order to address this issue, we proposed using reflectarrays placed on the top of buildings to eliminate blind zones in the valleys between buildings by controlling the direction of the scattered waves using the reflectarrays [2-6]. One of these reflectarrays is constructed using an approximate half wavelength cross dipole element array and an approximate one wavelength loop array for the ground plane that can simultaneously achieve dual polarization and frequency selective characteristics [2,4,6]. On the other hand, there are some reports of metamaterial reflectarrays that employ a mushroom structure, the elements for which are very short compared to the wavelength [3,7-10]. The metamaterial structure reflectarray is regarded as an artificial material that can control reflected waves in directions other than a mirror image, and the reflection phase can be calculated using a parallel resonant circuit model with inductance *L* and capacitance *C* [7]. The reflection phase is equal to zero at the *LC* resonant frequency and the reflection phase varies from $+\pi$ to $-\pi$ as the frequency changes. The resonant frequency can be controlled by changing the values of *L* and *C*, and there are typically three control methods [3,7-10]. The first method employs varactor diodes and changes in the voltage [7], the second method changes the via position of the mushroom structure [10], and the third involves changing the patch length of the mushroom structure to achieve a difference in capacitance [3,8,9]. There are mainly two problems with these conventional methods [3,7-10] when we focus on controlling the capacitance value in the design of mushroom reflectarrays based on the *LC* resonant frequency.

Submitted On: Nov 15, 2010
Accepted On: May 29, 2011

The first problem is the limitation caused by the manufacturing process. Although, it is necessary to achieve a reflection phase range from $+\pi$ to $-\pi$ at the desired frequency in the design of a reflectarray, it is difficult to achieve this. For example in the case of the third method [8, 9], it is necessary to close the distance between the mushroom patches to achieve a high capacitance; however, the degree to which the interval between the patches can be reduced is limited by the manufacturing process.

The other problem is the design method. In the conventional reflectarray design method [12, 8, 9], the element length is considered to determine the resonant frequency. However, in the mushroom reflectarray design, the resonant frequency is considered to be the LC resonant frequency, which is determined by L and C. Since the capacitance value depends on the size of the gap between elements, the size of the gap is more important than the element length. Therefore, in designing when the incident electric field and beam control direction of the scattered waves are set parallel, it is difficult to adjust the capacitance value using the conventional design method.

To address these issues, this paper proposes a novel multi-layer mushroom reflectarray in which the structure is decided not by the size of the element but by the size of the gap between the elements. In order to adjust the capacitance value, we apply the circuit theory such that the n-parallel arranged capacitances generate n-times capacitance and set parasitic patch layers on the mushroom structure to form a parallel capacitance arrangement.

A multi-layered mushroom structure is used to increase the capacitance in order to achieve low frequency resonance [11]. However, the patch arrangement in [11] is different from that proposed in this paper. The performance of the proposed multi-layer mushroom reflectarray is shown by using the finite element method analysis, theoretical calculation based on parallel circuit theory, and measurement. For this purpose, we constructed systems to measure the reflection and transmission scattering waves in a chamber. The actual measurement results of the scattering pattern are shown compared with theoretical results using a radar equation and radar cross section (RCS) calculated using the high frequency structure simulator (HFSS). The pattern configurations of both measurement and theoretical results are very similar and the difference of desired main beam direction at -70 deg. is less than 3 dB.

A "homogenization model" was proposed recently for the analysis of a mushroom structure [15, 16, 17]. In this paper, we use both homogenization and LC resonant models for 1 layer mushroom. We show the homogenization model has advantage for accuracy. For the multi-layer mushroom calculation, we focus more on the qualitative behavior concerning parasitic patches for a mushroom structure than the quantitative accuracy, and choose Sievenpiper's model [13].

II. EFFECT AND ANALYSIS OF PARALLEL SET CAPACITANCES

The LC resonant frequency of the mushroom structure can be changed as shown in (1) using variations in capacitance "C" and inductance "L" as reported in [13]. In formula (1), "ω" is the angular frequency.

$$\omega = 2\pi f = 1/\sqrt{LC}. \tag{1}$$

Table 1: Design parameters

Parameter	Symbol
Element space of mushroom structure for x axis direction	Δx
Element space of mushroom structure for y axis direction	Δy
Mushroom patch size for x axis direction	W_{mx}
Mushroom patch size for y axis direction	W_{my}
Parasitic patch size for x axis direction	W_{px}
Parasitic patch size for y axis direction	W_{py}
Gap size between mushroom patches: $\Delta y - W_{my}$	g_y
Gap size between parasitic patches: $\Delta y - W_{py}$	g_{yp}
Mushroom height	t
Interval between parasitic patches	$t_1,..,t_{n-1}$
Metallic ground layer	L_0
Mushroom patch layer	L_1
Parasitic patch layers	$L_2,\ldots,L_n$
Dielectric substrate layers	$D_0,\ldots,D_n$

This paper proposes a multi-layer mushroom structure for a reflectarray, which is shown in Fig. 1, that uses parasitic patches to obtain a wider variation in the capacitance value. Figure 1(a) shows a *n* layer mushroom structure consisting of a mushroom structure and *n-1* parasitic patch layers set on the mushroom structure. We use these parasitic patches to achieve *n* set parallel capacitance. A resonant circuit model and analysis model for the reflection phase calculation of the multi-layer mushroom structure are shown in Fig. 1(b) and 1(c), respectively. Table 1 gives the symbols and names of the parameters for the proposed structure. In terms of a non-parasitic layer mushroom structure, (2) - (5) are introduced based on a parallel resonant model as described in [13] using the parameters shown in Fig. 1 and Table 1. Inductance *L* in Fig. 1 is approximated by the product of permeability and the mushroom thickness, *t*, shown in (2). The gap between patches is expressed as (3). Capacitance *C* is determined by the gap between the adjacent mushroom elements expressed in (4) [13]. The direction of the electric field of the incident plane wave is assumed to be parallel to the Y-axis.

$$L = \mu t. \tag{2}$$

$$g_y = (\Delta \mathrm{y} - \mathrm{W_y}). \tag{3}$$

$$C = \frac{\varepsilon_0 (1+\varepsilon_r) W_\mathrm{x}}{\pi} \operatorname{arccosh}\left(\frac{\Delta y}{g_y}\right). \tag{4}$$

$$Z_s = j\omega L/(1-\omega^2 LC). \tag{5}$$

$$\Gamma = (Z_s - \eta)/(Z_s + \eta) = |\Gamma| \exp(j\phi). \tag{6}$$

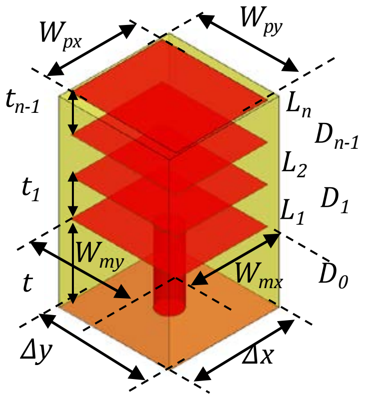

L_0: Metallic ground layer

L_1: Mushroom patch layer

L_2~L_n: Parasitic patch layer

D_0~D_{n-1}: Dielectric substrate layer

(a) Unit cell structure and parameters

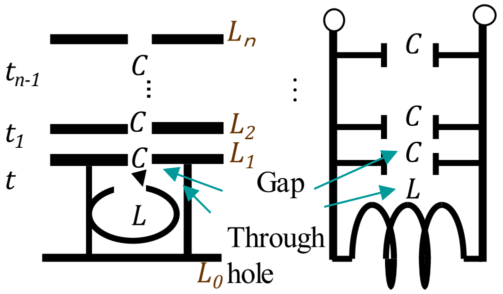

(b) Resonant circuit model

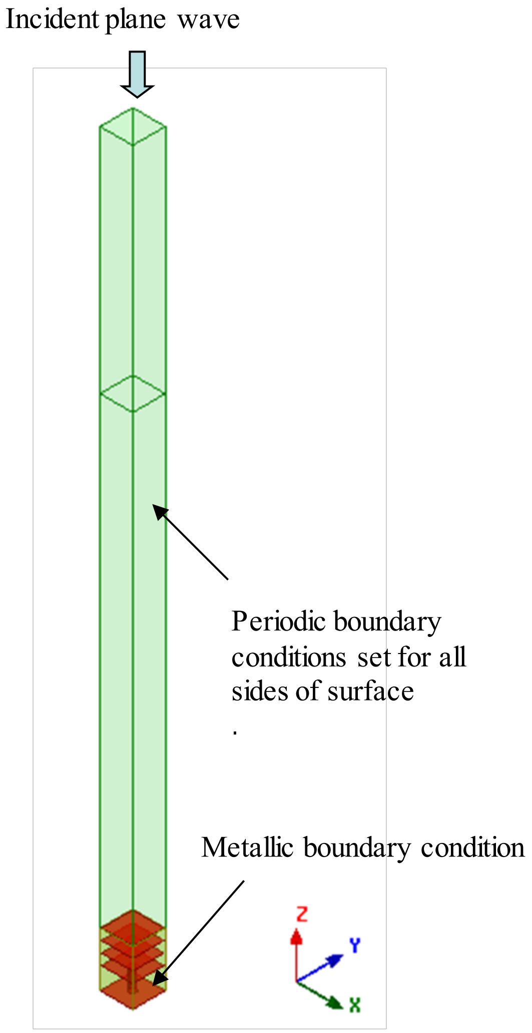

(c) Analysis model for reflection phase calculation.

Fig. 1. Multi-layer mushroom structure with parasitic element layers.

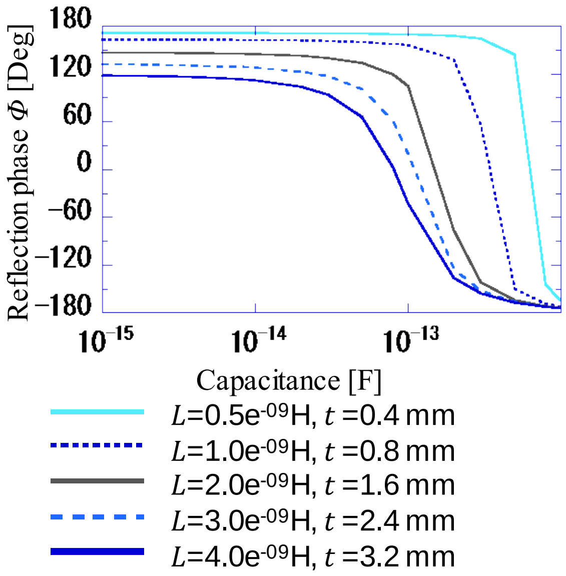

Fig. 2. Relationship between reflection phase ϕ and capacitance C when inductance L is a parameter.

The surface impedance of this array, Z_s, is expressed as (5). The reflection coefficient Γ and reflection phase Φ are shown in (6). In (6), η is equal to the impedance in free space. Figure 2 shows the theoretical calculation results using the above formulas of the relationship between reflection phase ϕ and C when L is a parameter. The frequency is set to 8.8 GHz, and the mushroom spacings, Δx and Δy, are set to 2.4 mm. When L is small and t is thin, the reflection phase range is wide at a high capacitance value and varies rapidly with the variation in the capacitance value.

Next, we describe the multi-layer mushroom structure. When the size of the parasitic patch, W_{px} (or W_{py}), is set to the same size as that of the mushroom patch, W_{mx} (or W_{my}), and both the gap between mushroom patches, g_y , and that between parasitic patches, g_{yp}, are the same, the multilayer mushroom structure shown in Fig. 1(a) is regarded to have the capacitance of n , set parallel in an equivalent circuit model. Therefore, the total capacitance is approximated as n by C . The surface impedance of this array is introduced in (7) by changing capacitance "C" of (5) to n times the capacitance, "nC."

$$Z_s = j\omega L/(1-\omega^2 LnC). \tag{7}$$

In the paper, we call the calculation using (1)-(7) as "LC resonant model".

According to [16, 17], surface impedance is introduced using the other analysis model. We call the model "Theory II" and briefly introduced as follows. In the Theory II, TM- and TE-impedance are shown as (8) and (9), respectively, where θ is the angle of incidence and θ_2 is expressed as formula (10).

$$Z^{TM} = \frac{j\omega\mu\frac{\tan(\beta t)}{\beta}\cos^2(\theta_2)}{1-2k_{eff}a\frac{\tan(\beta t)}{\beta}\cos^2(\theta_2)}. \tag{8}$$

$$Z^{TE} = \frac{j\omega\mu\frac{\tan(\beta t)}{\beta}}{1-2k_{eff}a\frac{\tan(\beta t)}{\beta}\left(1-\frac{2}{\varepsilon_r+1}\right)\sin^2(\theta)}. \tag{9}$$

$$\theta_2 = \arcsin\left(\frac{\sin(\theta)}{\sqrt{\varepsilon_r}}\right). \tag{10}$$

This paper set θ equal to 0 when we calculate reflection phase and then equation (8) and equation (9) are the same. In formula (9), k_{eff} is the wave number of the incident wave vector in the effective host medium [17]. ε_{eff} is the effective relative permittivity shown as (12) [16]. In formula (8),(9) a is expressed as equation (13)[17].

$$k_{eff} = k_0\sqrt{\varepsilon_{eff}}. \tag{11}$$

$$\varepsilon_{eff} = \frac{\varepsilon_r+1}{2}. \tag{12}$$

$$a = \frac{k_{eff}\Delta y}{\pi}\ln\left(\frac{1}{\sin\frac{\pi g_y}{2\Delta y}}\right). \tag{13}$$

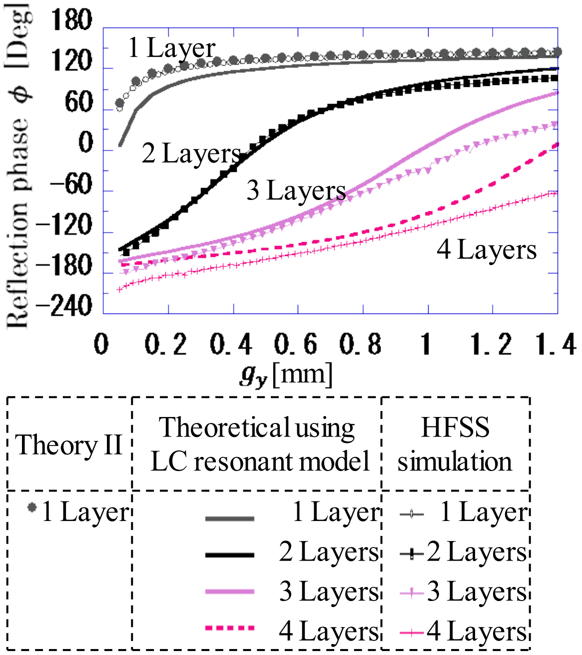

Fig. 3. Reflection phase vs. gap g_y when number of layers is a parameter.

Figure 3 shows the reflection phase versus the gap size g_y at 8.8 GHz for a mushroom structure comprising 1 to 4 layers. In this paper, we use HFSS for the simulation because it is popular for the mushroom structure analysis. HFSS is commercial software based on the finite element method (FEM) and uses the weighted residual method. In the HFSS simulation, we use the first order tangential element basis function. An incident plane wave is assumed coming from the Z-axis positive direction to the reflectarray as shown in Fig. 1(c). The electric field vector of the incident plane wave is set parallel to the Y-axis. We use periodic boundary conditions for the side surface of the element cell and the perfect electric conductor (PEC) boundary condition for the ground plane. The periodic spacing of the mushroom structure, Δx and Δy, are given as 2.4 mm. The thickness of the mushroom structure, t, is set equal to 1.6 mm and the parasitic patch intervals t_1, .. , t_3 are set equal to 0.8 mm. The relative permittivity of the dielectric substrate, ε_r, is 4.4. In Figs. 3, 4, and 5, the solid lines represent the theoretical results using LC resonant model from (1)-(7) and the symbols represent the simulation results using the finite element method. In Fig. 3, the theoretical results using Theory II from (8)-(13) are represented by gray solid circles for 1 Layer. The Theory II results pretty well match the FEM simulated result at 1 Layer. Although theoretical results using the LC resonant model and simulated results do not completely match and the difference increases when gap size g_y is larger than 1 mm and as the number of layers increases, the graph curves of the theoretical and simulated results have a similar tendency for each of the 1 to 4 layers. Therefore, we can confirm that the proposed approximation shown in (7) is useful in considering qualitatively the role of parasitic layers in a multi-layer mushroom structure and in investigating the physical phenomenon based on theory. We can control the capacitance value by changing the number of parasitic layers. Figure 3 also shows that when we increase the number of parasitic patch layers, we can reduce the reflection phase gradient versus the gap size. This is useful for a highly accurate design. The variation range of the reflection phase when we use parasitic layers is also wider than the case for a non-parasitic layer.

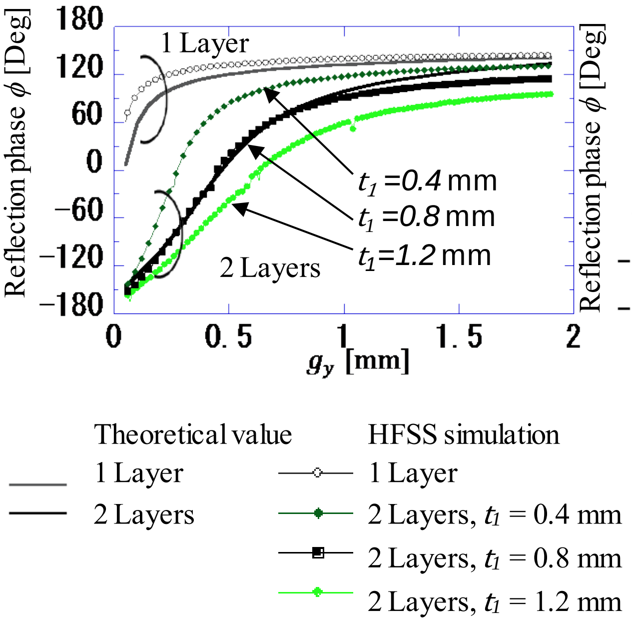

Fig. 4. Reflection phase ϕ vs. gap g_y of one parasitic layer mushroom (2 Layers) and without parasitic layer (1 Layer) when distance t_1 between parasitic patch and mushroom patch is a parameter.

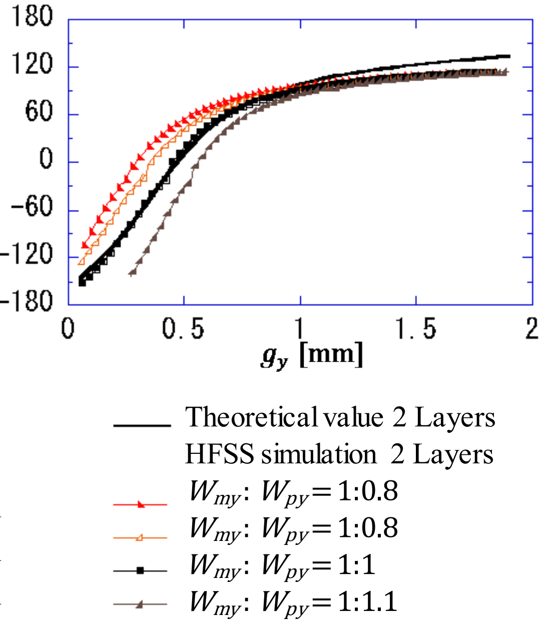

Fig. 5. Reflection phase ϕ vs. gap g_y for one parasitic layer (2 Layers) when parasitic patch size W_{py} is a parameter.

Next, we investigate the characteristics of the parasitic patch given by the parasitic size “W_{py}” and distance t_1 between the parasitic patches and mushroom patches. Figure 4 shows the reflection phase ϕ versus g_y of one parasitic layer mushroom (2 layers) and without a parasitic layer (1 layer) when distance t_1 between the parasitic patch and mushroom patch is a parameter. We consider that the proposed multi-layer mushroom structure using parasitic layers has two kinds of capacitance. One capacitance “C” exists in gaps between patches, and the other capacitance “C_L” exists between layers. In Fig. 4, when interval “e t_1” between layers is small, e.g., 0.4 mm, “C_L” is considered to be large and it prevents the effect of the parallel arrangement of capacitance C to increase the value of the capacitance. We adopt 0.8 mm for the value of t_1 in the paper because the difference between the theoretical results using the above formula and the simulated results using the HFSS is minimum. When we use different size patches the capacitance value also changes. Figure 5 shows reflection phase ϕ versus g_y for one parasitic layer mushroom patch (2 layer mushroom patches) when parasitic patch size W_{py} is a parameter. The conventional reflectarray using a microstrip patch generally uses a smaller size parasitic patch than the microstrip patch to achieve a broadband reflectarray [14]. In the case of the proposed multi-layer mushroom patches using parasitic patches, when we set mushroom patch size W_{my} and parasitic patch size W_{py} to the same value, i.e., $W_{my}:W_{py} = 1:1$, the reflection phase range is wider than when we set $W_{my}:W_{py} = 1:0.8$ or $1:0.9$ as shown in Fig. 5. This is because the effect of the parallel arrangement in this structure to achieve a higher capacitance is weakened by using small patches that enlarge the gap between the patches and reduce the capacitance of each gap. On the other hand, when we set $W_{my}:W_{py} = 1:1.1$, the C yield in the gap between parasitic patches can be large. However, when we adopt a larger parasitic patch than the mushroom patch, the adjacent parasitic patches touch each other. Consequently, when we choose the same size for each mushroom patch and parasitic patch, we can gain an advantage by setting the capacitances parallel to obtain a high capacitance and to increase the reflection phase range. The reflection phase versus the frequency for one parasitic layer (2 layers) and without a parasitic layer (1 layer) is shown in Fig. 6. In 2 layers, both the theoretical results and HFSS calculation results of the reflection phase versus frequency exhibit similar curves and we confirm that the proposed approximation is effective for frequency dependency. A comparison of the 1-layer and 2-layer mushroom structures shows that the resonant frequency that satisfies the reflection phase equal to zero shifts to a lower frequency by using a parasitic patch. From (1) and (2) above, it is considered that the resonant frequency shifts lower due to the increase in the capacitance value. This is because inductance L is the same for both cases with and without the mushroom structure. The largest difference in the reflection phase between the minimum $(W_y = 1.187\ \mathrm{mm})$ and maximum $(W_y = 2.3\ \mathrm{mm})$patches is 183 deg. at 11 GHz for the 1 layer mushroom structure and 240 deg. at 9 GHz for the 2 layer mushroom structure. Therefore, the maximum difference in the reflection phase can be expanded using parasitic elements. When the difference in the reflection phase between adjacent patches, $\Delta\phi_{k,k+1}$, shown in (14) satisfies (15) for each k, a wave is reflected toward control angle α. The model in Fig. 7 shows when the incident electric field direction and beam control direction are orthogonal.

$$\Delta\phi_{k,k+1} = \phi_k - \phi_{k+1}. \tag{14}$$

$$\alpha = \arcsin(\lambda\Delta\phi/2\pi\,\Delta y). \tag{15}$$

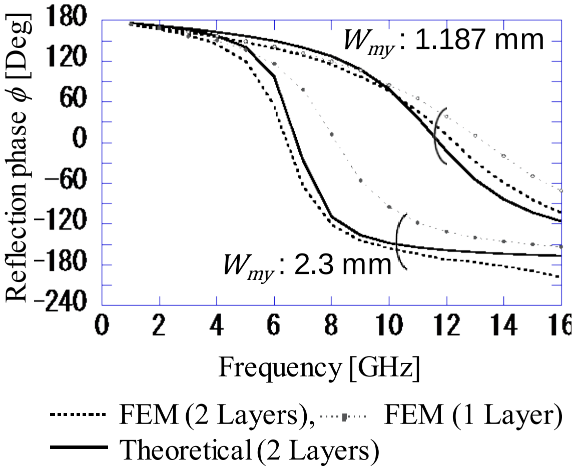

Fig. 6. Reflection phase vs. frequency for one parasitic layer (2 Layers) and without parasitic layer (1 Layer) compared to theoretical calculation.

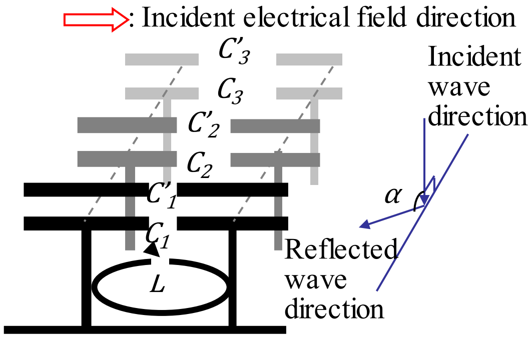

Fig. 7. Design model for multi-layer mushroom structure with parasitic element reflectarray.

III. DESIGN OF MULTI-LAYER MUSHROOM REFLECTARRAY BASED ON *LC* RESONANT CIRCUIT THEORY

In this section, we propose a novel design method for a multi-layer mushroom reflectarray with parasitic elements that focuses on the function of L and C when the incident electric field direction and beam control direction are parallel. We adopt two-layer patches for a multi-layer mushroom reflectarray, which achieves a wide reflection phase range as in Fig. 3. In the conventional reflectarray design method such as the microstrip reflectarray [12] in which the element sizes are usually almost half the wavelength, the resonant frequency and reflection phase are usually decided by the element size. Therefore, to achieve the desired reflection-phase difference, we usually set different size patch elements $(W_{my1}, W_{my2}, \ldots)$ at equal distances. Figure 8 shows the conventional reflectarray design model using the patch element length and we call this model the 'element model.' Figure 8(a) shows the model when the incident electric field and beam control direction of the scattered waves are set parallel. Figure 8(b) shows the model when the incident electric field and beam control direction of the scattered wave are set orthogonal.

In the conventional method [3,8,12], different size patches are arranged in the reflect beam direction as shown in Fig. 8. In Fig. 8(a), the beam control direction and incident electrical field direction are set parallel to the Y-axis. Different size patches selected to satisfy the desired reflection phase are arranged along the Y-axis.

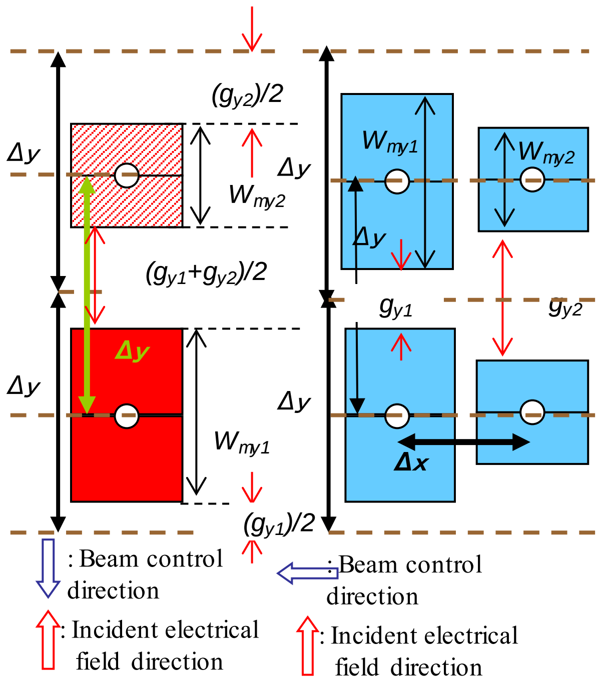

(a) Parallel setting (b) Orthogonal setting

Fig. 8. Conventional element model reflectarray.

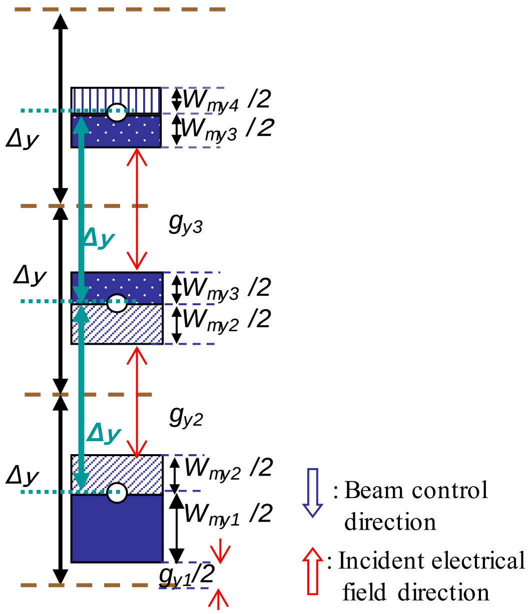

Fig. 9. Proposed gap model reflectarray.

In Fig. 8(b), the beam control direction and incident electrical field direction are set orthogonal. Different size patches selected to satisfy the desired reflection phase are arranged along the X-axis. However, in the case of Fig. 8(a), the beam control direction and incident electrical field direction are set parallel, when we set different size patch element 'W_{yi}' at equal distances, the gap value is changed from 'g_{y_i}' to '$g_{y_i}+g_{y_{i+1}}/2$'. Nevertheless, in the case of orthogonal beam control as shown in Fig. 8(b), when we set a different size patch element 'W_{yi}' at equal distances, gaps 'g_{y_i}' are also set in the same way. In the case of the mushroom structure, the element sizes are very small and we consider that the resonance is decided by LC resonance as described in Section II. Therefore, the capacitance value, which is determined by the gap size, is more important than that determined by the element size. To achieve a gap based design, this paper proposes a new design model in which the incident electric field and beam control direction of the scattered wave are set parallel. The model is called the "gap model" and is shown in Fig. 9. In the proposed model, in the first step, we set the via holes to be equally spaced, Δy. In the next step, different size gaps, g_{y_i}, are chosen that are decided based on the reflection phase shown in Fig. 3. Next, the gaps are allocated so that the center of each gap is also equally-spaced between vias as shown in Fig. 9. Then, half length patches, $W_{y_i}/2$, are set on both sides of the gaps. Consequently, the size of each patch is $\left(W_{y_i}+W_{y_{i+1}}\right)/2$ as shown in Fig. 9. Please note, in this model, the via hole is not set in the center of the patch. Finally, we can allocate different capacitances at equal spacing using the proposed method because the capacitance value is decided by the gap size as described in Section II.

IV. ANALYSIS AND MEASUREMENT RESULTS FOR MULTI-LAYER MUSHROOM REFLECTARRAY

Using the gap-model reflectarray design method that is described in Section III, a 70 deg. beam control mushroom reflectarray with parasitic elements for normal incidence (PV70Gs) can be achieved when the incident electric field and beam control direction of the scattered waves are set parallel. A 2-layer model that has the widest reflection phase range in Fig. 3 is adopted. We use the same frequency and periodic spacing for the mushroom structure, Δx and Δy, as that for the reflection phase calculation shown in Fig. 3, i.e., 8.8 GHz and 2.4 mm, respectively. In order to achieve a scattering reflect wave beam control angle, α, which is equal to 70 deg., each mushroom should satisfy the condition where the reflection phase difference, $\Delta\varphi_{k,k+1}$, between adjacent mushroom patches is 24 deg. based on (9). The design conditions and parameters of the gap model and element model are given in Table 2. Using the 24 deg. phase difference, 15 gaps are required to cover a 360 deg. reflection phase region. From Fig. 3, we can choose an adequate gap size for each required gap in the gap model. However, from Fig. 3, we can see that a gap smaller than 0.1 mm is necessary to achieve less than -140 deg.; however, it is difficult to achieve this in the fabrication process with high accuracy. We can also see from Fig. 3 that no patches exist in relation to a reflection phase greater than 125 deg. We can prepare 11 gap (12 patches correspond to the gaps) sizes from #1 to #11 that can yield the same phase difference between adjacent arrays and the gap sizes from #12 to #15 are not available as indicated in Table 2.

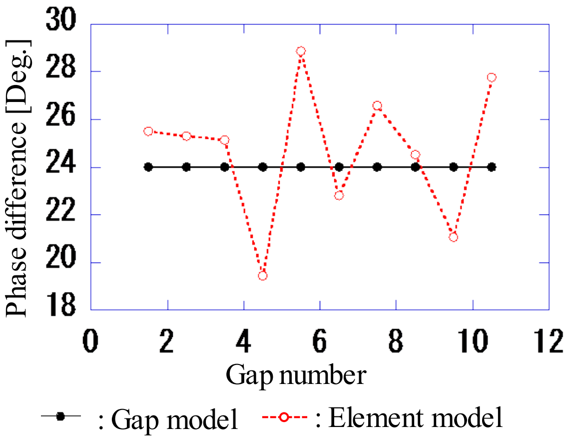

Fig. 10. Reflection phase difference vs. gap number for gap and element models.

In the case of the element model, we primarily decide the element patch size to obtain the required reflection phase that is described in Section III. Then, the reflection phases of the element model shown in Table 2 are decided by the gap size using Fig. 3. The reflection phase difference versus the gap number is shown in Fig. 10. The phase difference in the gap model is maintained at a constant 24 deg.; however, in the element model, the value differs in the range of 10 deg. The gap model and element model

Table 2: Design parameters of PV70Gs

	Gap model				**Element model**			
Gap number	**Symbol**	**Gap [mm]**	**Reflection phase [Deg.]**	**Phase difference [Deg.]**	**Symbol**	**Gap [mm]**	**Reflection phase [Deg.]**	**Phase difference [Deg.]**
#1	g_{y_1}	0.1	-139	24	$\frac{g_{y_1}+g_{y_2}}{2}$	0.139	-127	21
#2	g_{y_2}	0.177	-115	24	$\frac{g_{y_2}+g_{y_3}}{2}$	0.208	-106	24
#3	g_{y_3}	0.238	-91	24	$\frac{g_{y_3}+g_{y_4}}{2}$	0.266	-82	27
#4	g_{y_4}	0.294	-67	24	$\frac{g_{y_4}+g_{y_5}}{2}$	0.321	-55	23
#5	g_{y_5}	0.348	-43	24	$\frac{g_{y_5}+g_{y_6}}{2}$	0.385	-32	28
#6	g_{y_6}	0.422	-19	24	$\frac{g_{y_6}+g_{y_7}}{2}$	0.441	-4	20
#7	g_{y_7}	0.46	5	24	$\frac{g_{y_7}+g_{y_8}}{2}$	0.496	16	25
#8	g_{y_8}	0.532	29	24	$\frac{g_{y_8}+g_{y_9}}{2}$	0.584	41	25
#9	g_{y_9}	0.636	53	24	$\frac{g_{y_9}+g_{y_{10}}}{2}$	0.722	66	25
#10	$g_{y_{10}}$	0.809	77	24	$\frac{g_{y_{10}}+g_{y_{11}}}{2}$	-	91	-
#11	$g_{y_{11}}$	1.213	101	24	-	-	-	-
#12	$g_{y_{12}}$	-	125	-	-	-	-	-
#13	$g_{y_{13}}$	-	149	-	-	-	-	-
#14	$g_{y_{14}}$	-	173	-	-	-	-	-
#15	$g_{y_{15}}$	-	197	-	-	-	-	-

Name	**Symbol**	**Value**
Substrate name	*FR4*	-
Relative permittivity	ε_r	4.4
Dielectric loss-tangent	$\tan\delta$	0.018
Via hole diameter	vd	0.50 mm ϕ
Mushroom height	t	1.6 mm
Interval between parasitic patches	t_1	0.8 mm
Element space of mushroom structure	$\Delta x, \Delta y$	2.4 mm
Gap size between mushroom patches at x-axis direction	g_x	0.1 mm

reflectarrays are designed using parameters from Table 2.

The HFSS analysis model of the reflectarray (PV70Gs) is shown in Fig. 11. The reflectarray is constructed using a mushroom layer and patch layer. In Fig. 11, the perfect matched layer (PML) boundary condition is used at the top and bottom boundary surfaces and periodic boundary conditions are used at the side boundary surfaces. A plane wave incident along the Z-axis is assumed.

No patch is set if the optimum size patch that satisfies the desired reflection phase does not exist. The metallic ground plane, which represents the unavailability of a desired patch, is also removed to avoid undesired radiation from the ground plane. A mushroom structure usually uses a much smaller mesh for HFSS calculation than the wavelength. Therefore, it is difficult to analyze a large-scale mushroom array. This paper uses array factor approximation using the basic analysis model shown in Fig. 11 and the periodic boundary conditions.

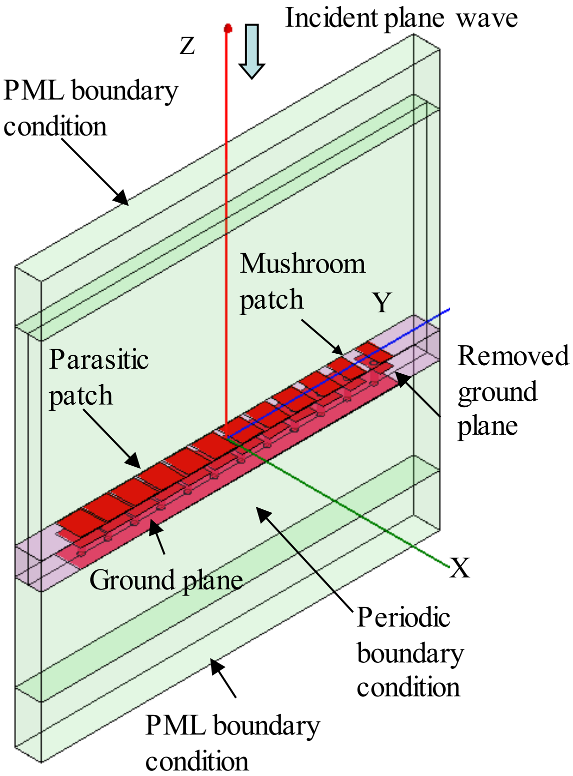

Fig. 11. The analysis model of 70 degree vertical beam control reflectarray (gap model); PV70Gs.

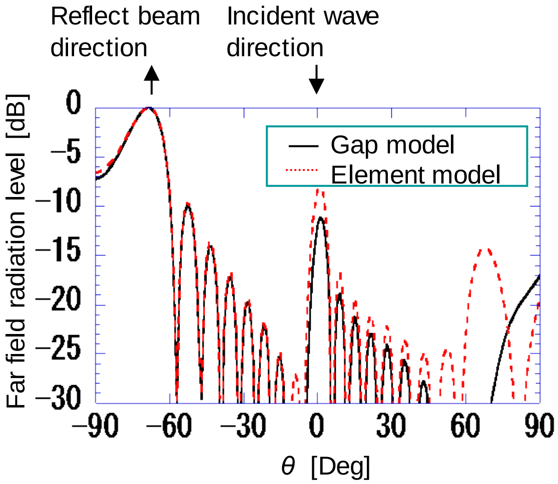

Fig. 12. Far field patterns for element and gap models (calculation results).

The far field scattering patterns of the gap model and element model reflectarrays are shown in Fig. 12. In Fig. 12, we arrange 129 arrays in the X-axis direction and 9 arrays in the Y-axis direction using an array factor and construct a 310 mm by 325 mm reflectarray. The levels are normalized to the peak level in the −70 deg. direction. Both results using the gap model and element model have a peak level at the desired −70 deg. and a radiation level in undesired directions, i.e., imaging direction ($\theta = 0°$) and 70 deg. direction of the conventional element model are higher than those for the proposed gap model. From Figs. 11 and 12, we can confirm that the proposed gap model is superior to the conventional element model.

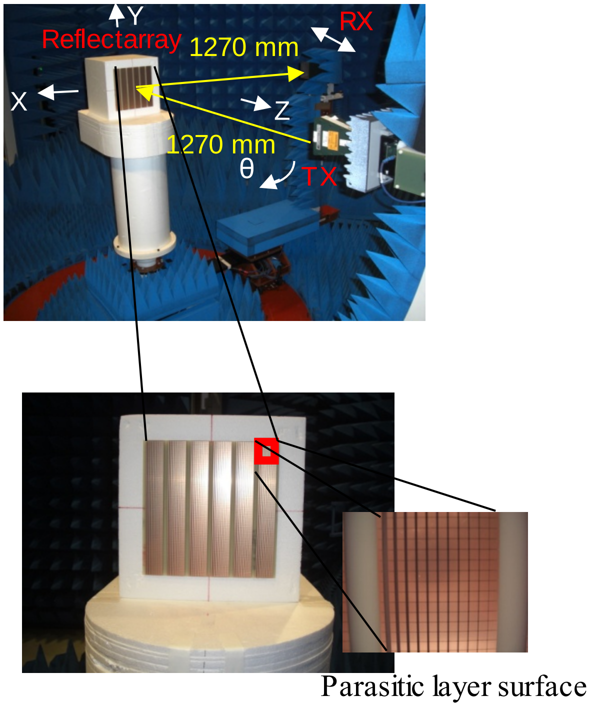

Fig. 13. Measurement system and multi-layer mushroom reflectarray with parasitic element designed using gap model (217 mm × 217 mm).

Next, we fabricate a 217 mm by 217 mm gap model reflectarray and measure the scattering of reflected and transmission waves in the chamber. Photographs of the measurement system and reflectarray are shown in Fig. 13. In the system, the reflectarray is set at the center and the distances between the reflectarray and transmitter antenna (TX) and that between the reflectarray and receiver antenna (RX) are set to 1270 mm. The TX is set in front of the reflectarray and an incident wave is assumed from $\theta = 0°$ direction (The coordinate system is shown in Fig. 13). The RX horn is moved on a rail along the circumference of a circle to scan the scattering level.

Generally, the measurement distance must satisfy (16) for a radar cross-section measurement [18]. In (16), "*D*" represents the maximum diameter of the target, which we set to 217 mm. Therefore, the measurement distance must be longer than 2500 mm. However, it is difficult to maintain a dynamic range when we use a long measurement distance or a small reflectarray. Moreover, the chamber size is limited.

$$\rho > \frac{2D^2}{\lambda}. \tag{16}$$

The far field scattering pattern of the measurement and calculated results are shown in Fig. 14. To avoid collision between the TX and RX, the measurement range is set to $20° < \theta < 340°$. In the $-20° < \theta < 20°$ region, only simulated results are shown in the graph. In Fig. 14(a), the levels are normalized to 0 dB at the peak level at -70 deg. Figure 14(b) shows the actual measured value in the chamber using the settings indicated in Fig. 13 by the aqua colored line. In the measurement, we set the level equal to 0 dB when the transmission cable and received cable are directly connected. We use standard horn antennas (Flan Microwave LTD.) and the directivity gain at the 8.8 GHz is 18.6 dBi. The black line in Fig. 14(b) shows the theoretically calculated received level using the radar equation (17) and radar cross section σ_r of the reflectarray calculated using HFSS.

$$W_a(\theta,\varphi) = \frac{\lambda^2 {G_a}^2}{(4\pi)^3 R^4} W_t \sigma_r(\theta,\varphi). \tag{17}$$

The symbol name and value used in (17) are shown in Table 3.

Table 3: Symbol name and value used in radar equation

Name	Symbol	Value
Received power	W_a	
Transmission power	W_t	1 mW
Antenna gain; standard horn from Flan micro	G_a	18.6 dBi
Distance between transmission antenna and reflectarray	R	1270 mm
Radar cross section of reflectarray	σ_r	Calculated using HFSS
Wavelength (8.8 GHz)	λ	0.034

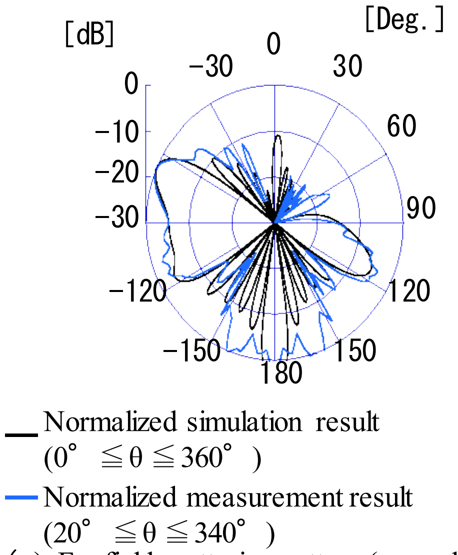

(a) Far field scattering pattern (normalized).

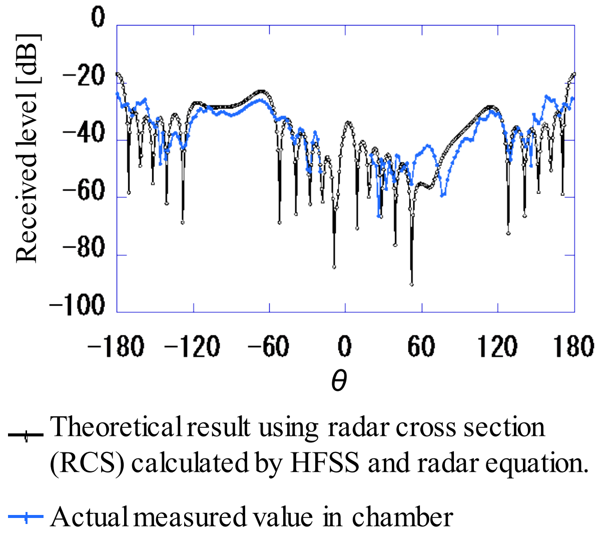

(b) Actual measurement value and theoretical result from radar equation and simulated RCS.

Fig. 14. Comparison between theoretical, simulated, and measurement results of far field scattering pattern.

In Fig. 14(b), the values in the desired −70 direction are −26.3 $\mathrm{dB_m}$ (measurement) and −23.4 $\mathrm{dB_m}$ (theoretical). The difference is 2.9 dB. There exists a side lobe level at θ equal to 70 deg. that is in the opposite axial direction of the desired −70 deg. Because we use the element spacing of 2.4 mm and 15 divisions for one period in the −70 deg. reflection beam direction, in the design of the 70 deg. beam control we also use the same element spacing of 2.4 mm and 15 divisions. The design differences in the reflected beam control between 70 deg. and -70 deg. are represented by the phase difference between adjacent elements of -24 deg. or 24 deg. Therefore, when the difference in the reflection phase between adjacent elements is shifted due to manufacturing error, the side lobe level is increased. In Fig. 14, there also exists a side lobe level at "θ" equal to the direction caused by specular reflection in the simulation. Please note that the direction cannot be measured. Under the conditions given above for array factor approximation analysis and measurement in a small chamber, we confirm that the graphs of the calculation and measurement scattering radiation pattern results are overlapped except for the back lobe radiation. In the reflectarray design of the paper, we assume the incident wave is coming from the upper side ("θ" equal to 0 deg. direction). However, when we use the reflectarray to improve the propagation environment, the waves come from several oblique directions [3, 20]. Otherwise, the mushroom like structure exhibits dual resonant behavior for an oblique incident as reported in [16 and 19]. We need further study for these oblique incidents for the reflectarray.

V. CONCLUSION

This paper proposed a novel reflectarray design using a multi-layer mushroom structure with parasitic elements based on capacitance value control in the LC resonant circuit model. Based on the study of the LC resonant circuit model, this paper showed that the parallel set capacitance value can be theoretically controlled using the number of parasitic layers. This paper also proposed a novel reflectarray design method for a 70 deg. beam control mushroom reflectarray when the incident electric field and beam control direction of the scattered waves are set parallel by focusing on the capacitance value. Finally, this paper showed that the proposed design exhibits good performance by comparing the simulated and experimental results.

ACKNOWLEDGMENT

This work was carried out by "the research and development project for expansion of radio spectrum resources" from The Ministry of Internal Affairs and Communications, Japan. The authors especially thank Prof. Shinji Uebayashi of Chukyo University, Prof. Kunio Sawaya of Tohoku University, and Dr. Long Li and Dr. Atsushi Murase of NTT DOCOMO who provided continuous support for this study.

REFERENCES

[1] R. Fisher, "60 GHz WPAN Standardization within IEEE 802.15.3c," *Signals, Systems and Electronics*, 2007. ISSSE '07, pp. 103 - 105, 2007.

[2] L. Li, Q. Chen, Q. Yuan, K. Sawaya, T. Maruyama, T. Furuno, and S Uebayashi, "Microstrip Reflectarray using Crossed-Dipole with Frequency Selective Surface of Loops," *ISAP2008*, TP-C05, 1645278, 2008.

[3] T. Maruyama, T. Furuno, and S. Uebayashi, "Experiment and Analysis of Reflect Beam Direction Control Using a Reflector Having Periodic Tapered Mushroom-Like Structure," *ISAP2008*, MO-IS1, 1644929, p. 9, 2008.

[4] L. Li, Q. Chen, Q. Yuan, K. Sawaya, T. Maruyama, T. Furuno, and S Uebayashi, "Frequency Selective Reflectarray using Crossed-Dipole Elements with Square Loops for Wireless Communication Applications," *IEEE Trans. Antennas Propagat.*, vol. AP-59, no. 1, pp. 89-99, 2011.

[5] L. Li, Q. Chen, Q. Yuan, K. Sawaya, T. Maruyama, T. Furuno, and S Uebayashi, "Novel Broadband Planar Reflectarray with Parasitic Dipoles for Wireless Communication Applications," *IEEE APWL*, vol. 8, pp. 881-885, 2009.

[6] T. Maruyama, T. Furuno, T. Ohya, Y. Oda, Q. Chen, and K. Sawaya, "Dual Frequency Selective Reflectarray for Propagation Improvement," *IEEE iWAT*, 2010, pp. 1-4, 5464764, March 2010.

[7] D. Sievenpiper, J. H. Schaffner, H. J. Song, R. Y. Loo, and G. Tangonan, "Two-Dimensional Beam Steering using an Electrically Tunable Impedance Surface," *IEEE Trans. Antennas Propagat.*, vol. AP-51, no. 10, pp. 2713-2722, Oct. 2003.

[8] K. Chang, J. Ahn, and Y. J. Yoon, "Artificial Surface Having Frequency Dependent Reflection Angle," *ISAP 2008*.

[9] K. Chang, J. Ahn, and Y. J. Yoon, "High-Impedance Surface with Nonidentical Lattices," *IEEE iWAT 2008*, P315, pp. 474-477, 2008.

[10] F. Yang and Y. Rahmat-Samii, "Polarization Dependent Electromagnetic Band Gap (PDEBG) Structure: Design and Applications," *Microwave Opt. Technol. Lett.*, vol. 41, no. 6 pp. 439-444, July 2004.

[11] D. Sievenpiper, L. Zhang. R. F. J. Broas, N. G. Alexopolous, and E. Yablonovitch, "High-Impedance Electromagnetic Surfaces with a

Forbidden Frequency Band," *IEEE Trans. Microwave Theory and Techniques* vol. MTT-47, no. 11, pp. 2059-2074, Nov. 1999.

[12] D. M. Pozar, T. S. Targonsky, and H. D. Syrigos, "Design of Millimeter Wave Microstrip Reflectarrays," *IEEE Trans. Antennas Propagat.*, vol. AP-45, no. 2, pp. 287-295, 1997.

[13] D. F. Sievenpiper, "High-Impedance Electromagnetic Surfaces," Ph.D. Dissertation, UCLA, 1999.

[14] J. Huang, Reflectarray Antennas, *IEEE Press*, Wiley-Interscience, pp. 97-99, 2007.

[15] A. B. Yakovlev, M. G. Silveirinha, O. Luukkonen, C. R. Simovski, I. S. Nefedov, and S. A. Tretyakov, "Characterization of Surface-Wave and Leaky-Wave Propagation on Wire-Medium Slabs and Mushroom Structures Based on Local and Non-Local Homogenization Models," *IEEE Trans. Microwave Theory and Techniques*, vol. MTT-51, no. 11, pp. 2700-2714, November 2009.

[16] O. Luukkonen, M. G. Silveirinha, A. B. Yakovlev, C. R. Simovski, I. S. Nefedov, and S. A. Tretyakov, "Effects of Spatial Dispersion on Reflection from Mushroom-type Artificial Impedance Surfaces," *IEEE Trans. Microwave Theory and Techniques*, vol. MTT-51, no. 11, pp. 2692-2699, November 2009.

[17] O. Luukkonen, C. Simovski, G. Granet, G. Goussetis, D. Lioubtchenko, A. V. Raisanen, and S. A. Tretyakov, "Simple and Accurate Analytical Model of Planar Grids and High-Impedance Surfaces Comprising Metal Strips or Patches," *IEEE Trans. Antennas Propagat.*, vol. 56, no. 6, pp. 1624-1632, 2008.

[18] W. L. Stutzman and G. A. Thiele: "Antenna Theory and Design," second edition, Wiley, 1998.

[19] L. Li, Q. Chen, Q. Yuan, L. Changhong, and K. Sawaya, "Surface-Wave Suppression Band Gap and Plane-Wave Reflection Phase Band of Mushroom Like Photonic Band Gap Structures," *Journal of Applied Physics*, vol.103, pp. 023513-023513-10, 2008.

[20] K. Shin, Y. Oda, T. Furuno, T. Maruyama, and T. Ohya, "A Novel Approach for Capacity Improvement of 2x2 MIMO in LOS Channel Using Reflectarray," *IEEE VTC* 2011 Spring, 2011.

Tamami Maruyama is a senior research engineer at the NTT DOCOMO Research Laboratories. She received her B.S. and M.S. degrees in 1985 and 1988, respectively, from the department of mathematics, Tsuda College, Tokyo, Japan. In 2001, she received her Ph.D. degree from Tohoku University, Sendai, Japan. In 1988, she joined the Nippon Telegraph and Telephone Corporation (NTT). In 2003, she joined NTT DOCOMO INC. In 1995, she received the Young Engineer Award from IEEE AP-S Tokyo Chapter. In 1998, she received the Excellent Paper Award from the IEICE. In 2008, she received the Best Paper Award from ISAP 2008. Dr. Maruyama is a member of the IEEE and IEICE. Her main research interests include the optimum antenna design method, genetic algorithm, application of metamaterials and reflectarray to wireless communications, design of multi-frequency antennas for digital mobile communication base stations, small sector antennas for indoor high-speed wireless LANs and small multi-band antennas that employ the genetic algorithm for handsets.

Tatsuo Furuno received the B.S. degree from Niigata University, Japan, in 1986. He joined NTT and engaged in the research and development of cordless telephone system, radio propagation characteristics for PHS (personal handy-phone system) and Wireless LAN. He joined NTT DOCOMO in 1999 and engaged in the research and development of public wireless LAN service, indoor radio propagation and cognitive radio. He is currently a senior research engineer at NTT DOCOMO Research Laboratories.

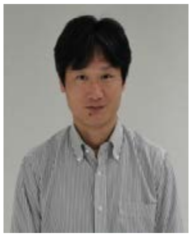

Yasuhiro Oda received the B.S. degree in Physics from Nagoya University, Nagoya, Japan, in 1990. He joined the Nippon Telegraph and Telephone Corporation (NTT) Laboratories, Kanagawa, Japan, in 1990. He has been engaged in research on radio propagation for land mobile communication systems, radio link design, and positioning technologies. Since 1992, he has been with the Research and Development Department, NTT Mobile Communication Network Inc. He is currently an Executive Research Engineer of Research Laboratories, NTT DOCOMO, Inc.

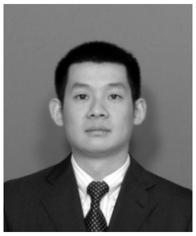

Jiyun Shen was born in Shanghai, China. He received his B.S. and M.S. degrees in 2001 and 2003, respectively, from the undergraduate department of Electrical and Electronic Engineering and the graduate department of Communications and Computer Engineering, Kyoto University, Japan. From 2003, he became a research engineer of the NTT

DOCOMO Research Laboratories. In 2008, he received the Young Researcher's Award from the IEICE. His current main research interests include location algorithm, global positioning system (GPS), orthogonal frequency-division multiplexing (OFDM), multiple-input multiple-output (MIMO), channel coding, radio wave propagation analysis, radio wave signal processing. He is a member of IEICE communications society.

Tomoyuki Ohya received his B.E. and M.E. degrees in Electronic Engineering from Kyoto University in 1986 and 1988 respectively, and his M.S. degree in Management of Technology from Massachusetts Institute of Technology in 2000. He joined Nippon Telegraph and Telephone Corporation (NTT) in 1989, and since 1992, he has been working at NTT DOCOMO. He was engaged in the research and development of digital signal processing technologies and wireless transmission technologies. He received Young Researcher’s Award from IEICE in 1995. He is a member of IEEE, IEICE and The Acoustical Society of Japan.

Currently, he is a general manager of technology & solution department in mmbi, Inc., and in charge of standardization and development of ISDB-Tmm mobile multimedia broadcasting technologies.

8×8 Near-Field Focused Circularly Polarized Cylindrical DRA Array for RFID Applications

Saber H. Zainud-Deen, Hend A. Malhat, and Kamal H. Awadalla

Department of Electronics and Electrical Communications Engineering
Faculty of Electronic Engineering, Menoufiya University, Egypt
anssaber@yahoo.com, er_honida@yahoo.com

***Abstract* —** The design of an 8×8 near-field focused circularly polarized dielectric resonator antenna (DRA) array for fixed RFID reader applications at 5.8 GHz is presented. The proposed antenna array consists of 64-element of cylindrical dielectric resonator antennas (CDRA) with two orthogonal feeding probes located inside the CDRA element. A single element CDRA with supporting arms is used as a building block of the array provided good impedance matching and circular polarization at 5.8 GHz. The perforation technique is used for the supporting arms to reduce the manufacturing complexities in the CDRA mounting over the ground plane. The sequential feeding technique is applied to improve the gain and circular polarization bandwidth of the single element and the array. The characteristics of the near-field focused array are introduced compared to that of the uniformly phased array. The finite integral technique and the finite element method are used to compute the array performance.

***Index Terms* —** CDRA, fixed reader antenna, RFID, sequential feeding.

I. INTRODUCTION

RFID systems have been applied in many applications for their advantages over other automatic identification systems [1]. Practically, the RFID reader has a read zone that can sometimes be difficult to control due to multipath effects or reflections of the RF signal. Problems that may arise with conventional RFID readers include:1) the reader may detect tags that are not in the reader coverage area, and 2) the tags may be located adjacent to the reader antenna thus blocking its field. Spatial isolation of an RFID tag may be difficult if the interrogation range of the RFID readers is not easily controlled or adjusted to a lower power setting. This can lead to errors in customer purchases or errors in verification that an item is in a specific physical location (e.g., baggage on a specific cart) [2, 3]. The RFID reader antenna is an important component in RFID systems and it has been designed with circularly polarized (CP) operation. CP for the reader antenna in transmission is preferred because the tag antenna (which is linearly polarized) will receive enough power from the transmitter irrespective of its orientation. A CP antenna with a low profile, small size, lightweight, high gain, and high front-to-back ratio is required in a portable RFID reader [4-6]. The other type of RFID reader is the fixed reader. Generally, fixed-reader antennas are complex microstrip patch arrays with high gain, and a relatively narrow beam and low side lobe level [7-9].

Using antenna arrays for a fixed RFID reader will result in long read range. The far-field region is determined according to the dimensions of the array (L×L) and the operating frequency by ($2L^2/\lambda$). In some applications, tags may be located in the near-field region of the fixed reader antenna array not in their far-field region as is usually the case in a standard communication system. Therefore, a reader antenna array exhibiting a near-field (NF) focused radiation, which is able to maximize the field amplitude in a size-limited spot within the antenna near-field region, while not affecting the field strength far from the antenna (far-field region), is needed. Recently, NF-focusing has attracted major interest due to its potential applications in near-field sensing and imaging microscopy [10-11]. NF- focusing is used in RFID to increase the field incident on the tags at allowed effective isotropic radiated power (EIRP)

Submitted On: Aug 6, 2011
Accepted On: Oct 23, 2011

[12-14]. In [15], a circular half-wavelength dipole array is used to study the effect of changing the focusing distance on the power in the Fresnel region. In this paper, an 8×8 NF-focused cylindrical DRA phased array with supporting arms for fixed RFID reader at 5.8 GHz is proposed. The NF-focused CDRA array is designed to maximize the radiated power density in a limited size spot in the near field of the RFID reader. The performance parameters of the NF-focused array are compared with that of uniform phased array. The array consists of 64 sequentially fed CDRA elements with two supporting arms mounted on a square ground plane. Each CDRA element is fed via two orthogonal probes located at two orthogonal points from the CDRA center. The finite integration technique (FIT) [16] is used to optimize and analyze the antenna array performance parameters such as reflection coefficient, radiation pattern and antenna gain. The finite element method (FEM) [17] is used to validate the results. The novelty of this work is the using of the CDRA elements in the phased array for wide bandwidth, no metallic loss (high radiation efficiency), and high gain (wide coverage area for RFID reader). The paper is organized as follows. In Section II, numerical results for a circularly polarized CDRA with supporting arms as a building block for the RFID reader antenna array are investigated. Near field focused CDRA array for fixed RFID reader consists of 64 CDRA elements is designed at 5.8 GHz. Section III concludes the results.

III. NUMERICAL RESULTS

Figure 1 shows the geometry of a single cylindrical dielectric resonator antenna with two feed probes excitation. The CDRA with dielectric constant ε_r of 10.2 is used [18]. It has a radius '*a*' of 5.9 mm and a height 'H_d' of 8.3mm. The CDRA is designed to operate around 5.8 GHz. Two coaxial probes are located off the center by distance d_f of 5.1 mm. Each probe has radius of 0.25 mm and height h_f of 3.9 mm. The two probes are parallel and located at similar positions on two orthogonal diameters and the feeding is arranged such that the two probes have a phase difference of 90^o. Because of the fabrication complexity of CDRA over ground plane, four supporting arms having rectangular shape are connected with the CDRA. In [19], perforated structure was proposed to overcome the mounting problems of the CDRA over the ground plane and save more manual effort in the alignment of the CDRA with the feeding structure especially for arrays. The technique of perforating a dielectric sheet eliminates the need to position and bond individual CDRA elements in the array. Perforations create different effective dielectric permittivity and make the fabrication of CDRA arrays feasible. The perforations result in lowering the effective dielectric constant for the region between the CDRA elements. The CDRA element is made from one piece of dielectric material; with a perforated bonding dielectric rods and completely eliminating all the rest of the dielectric material. The dielectric rods have low dielectric constant and thin enough to avoid guiding waves around the design frequency of the element itself. The effective dielectric constant, ε_{reff}, of the perforated material can be calculated from [19]

$$\varepsilon_{r\,eff} = \varepsilon_r(1-\alpha)+\alpha\,,$$

$$and\ \ \alpha = \frac{\pi R_p^2}{2\left(\sqrt{3}/4\right)\ S_p^2} \qquad (1)$$

where R_p is the radius of the air holes, and S_p is the center to center separation distance of the holes. The holes forming the perforation are only one line centered along the axis of the ribbon forming the supporting arm. Thus, the supporting arms are used to reduce the fabrication complexity while keeping the same radiation characteristic as arm free element [19, 20].

The dimensions of the supporting arms are width W_p= 4 mm and thickness H_p=1 mm. The supporting arms are perforated by incorporating air holes in the arms. The air holes have equal radii, R_p=1.2 mm and center to center separation S_p=3R_p. The CDRA elements with supporting arms are mounted on square ground plane with edge length 'G' of 35.15 mm. Figure 2 shows the simulated reflection, S_{11}, at the two ports of the feeding pins of the single CDRA element with perforated supporting arms against the frequency. The two ports produced the same performance due to their position similarity. Good impedance matching is obtained with impedance bandwidth extending from 5.62 GHz to 6.12 GHz for S_{11} < -10 dB.

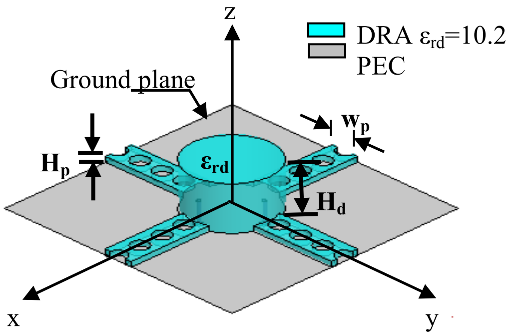

a. 3-D view

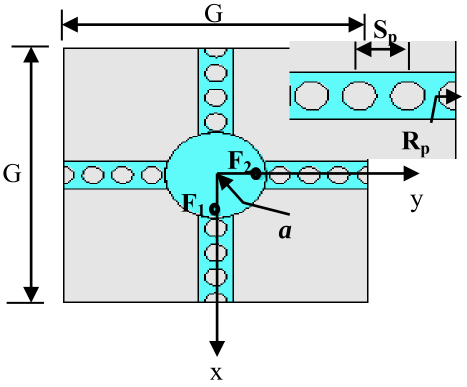

b. Top view

Fig. 1. The geometry of circularly polarized CDRA with supporting arms.

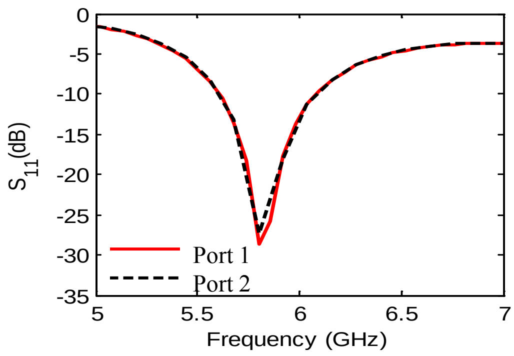

a. Reflection coefficient

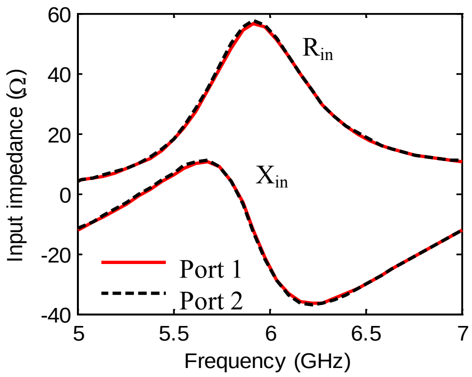

b. The input impedance

Fig. 2. The power reflection coefficient and input impedance versus frequency of the CDRA with supporting arms.

The simulated radiation pattern components, left hand polarization, E_L, and right hand polarization, E_R, of the single CDRA element at 5.8 GHz in x-z plane and y-z plane are shown in Fig. 3. Asymmetrical radiation pattern is obtained with high cross-polarization level due to the coupling effect between the excitation orthogonal probes, as well as the asymmetrical positioning of the feeds with respect to the two planes. Good agreement is obtained between the results calculated by FEM and FIT techniques.

The main polarization (E_L) is within -10 dB level in a beam of about 100° width centered at the 0° direction. The cross polarization (E_R) level is more than -10 dB relative to the main polarization (E_L) within the circular polarization beam (100°). These results indicate good performance of this dielectric resonator antenna for RFID reader application.

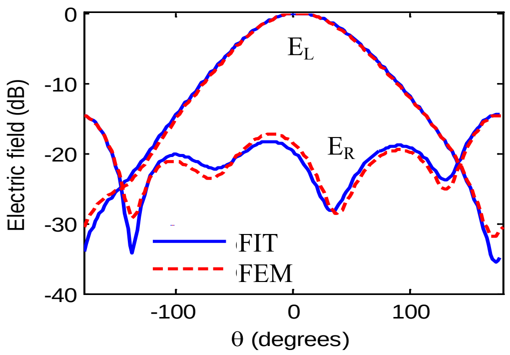

a. x-z plane

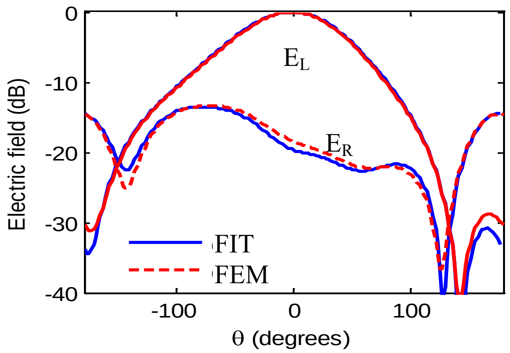

b. y-z plane

Fig. 3. The simulated radiation pattern components of the single element at 5.8 GHz.

The axial ratio at the normal axis, $\varphi = \theta = 0^o$, versus frequency is shown in Fig. 4a. The antenna provides circular polarization with minimum value of 1.9 dB at 5.8 GHz with a relatively wide axial ratio bandwidth (AR< 3dB) of the order of 40.74%. The antenna gain at the normal axis over the operating band is shown in Fig. 4b. The gain at the normal axis is 7.15 dB at 5.8 GHz and nearly constant within 0.5 dB over the RFID frequency band (5.65- 5.95 GHz).

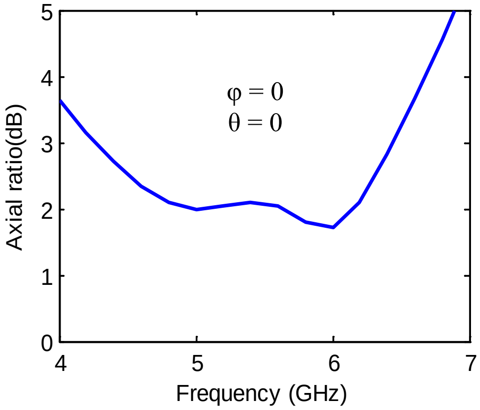

a. Axial ratio

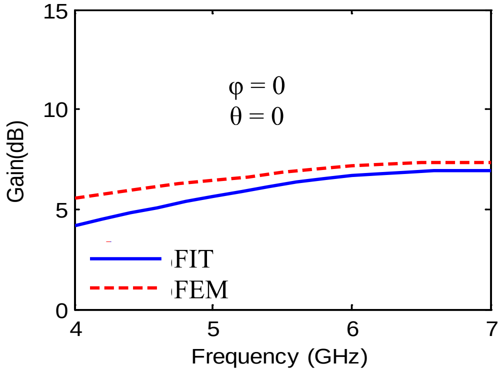

b. Gain

Fig. 4. The simulated axial ratio and antenna gain versus frequency of the single element CDRA with supporting arms.

An 8×8 RFID reader antenna array with supporting arms is shown in Fig. 5. The area of the array is L×L= 28.13 × 28.13 cm^2 (5.44 λ×5.44 λ where λ is the free-space wavelength at 5.8 GHz). The distance G between the elements is 35.16 mm (0.68λ) to reduce the mutual coupling between the elements. The sequential feeding technique is applied to the CDRA elements in order to improve the circular polarization bandwidth (axial ratio bandwidth) and gain of the antenna array [21]. For each sub-array forming (2×2) elements, the elements in one diagonal are 90° out of phase and rotated -90° in orientation relative to the elements in the other diagonal (see Fig. 5b). This sequential feeding mechanism produces two fields with equal magnitude and out of phase by 90° which results in improving the circular polarization bandwidth of the array.

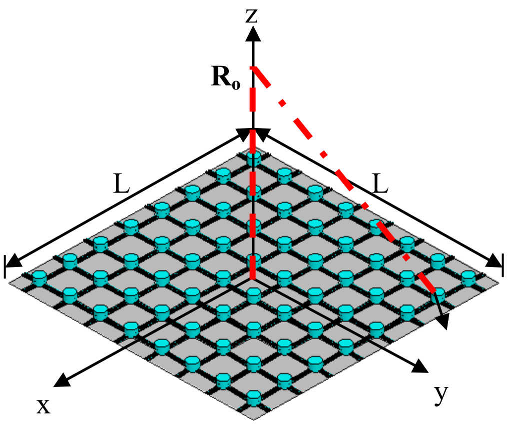

a. 3-D view.

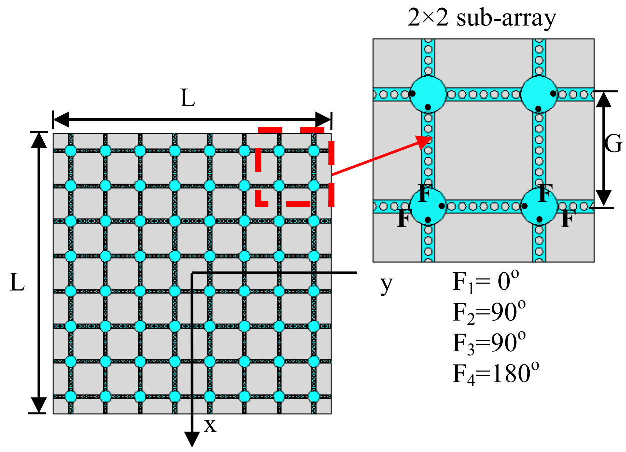

b. Top view

Fig. 5. The geometry of the proposed 8 ×8 RFID reader antenna array consists of 4 sub-array of CDRA with supporting arms.

The antenna array aperture is placed in the (x, y) plane and (x_i, y_i) are the position coordinates of the ith element. The phase of the feeding currents has been adjusted to maximize the radiated field at a distance z = R_o= 40 cm (The assumed boundary for the far field is $2L^2/\lambda$ = 306.11 cm) from the antenna aperture. For the NF- focused phased array, the phase shift for the ith element can be calculated from,

$$\phi_i = \frac{2\pi}{\lambda}\left(\sqrt{x_i^2 + y_i^2 + R_o^2} - R_o\right). \tag{2}$$

The beamwidth between 3-dB points in the focal plane is defined as the array spot size. The spot size area radius, W, of a NF-focused planar array depends on the interelement distance, array size and geometry [22]

$$W = 0.8868\, R_o \cdot \frac{\lambda}{L}. \tag{3}$$

In this case, W= 6.52 cm (1.26 λ_o). The Poynting vector is equal to the cross product of electric field, $\bar{E}$, by the complex conjugate of the magnetic field, $\hat{H}$. The magnitude of its real part is the active power density while the magnitude of its imaginary part is the reactive power density [23].

Adding the phase shift to the array elements results in focusing both the active and reactive power density at the focal plane (the plane includes the focus point). The ratio between the active power density and the reactive power density is very large (about 256). Thus, only the active radiated power density will be taken into account and is given by

$$S = \left\| \operatorname{Re}\left(\vec{S}\right) \right\| = \left\| \operatorname{Re}\left(\vec{E} \times \vec{H}^*\right) \right\|. \tag{4}$$

The equivalent plane wave power density p is defined from the E-field or the H-field as follows [21]

$$p = S_e = \frac{\left\|\vec{E}_x\right\|^2 + \left\|\vec{E}_y\right\|^2 + \left\|\vec{E}_z\right\|^2}{\eta_o}, \tag{5}$$

$$or \;\; p = S_h = \eta_o \cdot \left(\left\|\vec{H}_x\right\|^2 + \left\|\vec{H}_y\right\|^2 + \left\|\vec{H}_z\right\|^2 \right)$$

where $\eta_o = 377\Omega$. The normalized power density distribution in the x-y plane for the uniformly phased array compared to that of the NF-focused array is used to introduce the effect of focusing as shown in Fig. 6. The power density of the NF-focused antenna array decreases rapidly from the focal point than that of the uniformly phased array. The -3dB contour curve of the NF-focused array exhibits a diameter of about 8 cm. Contour plots of the normalized power density in the x-z plane is plotted in Fig. 7.

Figure 8 shows the variations of the power density along the z-axis from the antenna aperture of the NF-focused array. The 3-dB focused depth of the array is 31.2 cm along the array axis.

Using a rectangular to spherical coordinate transformation, the three components of the electric field E_x, E_y, and E_z are transformed to their spherical counterpart E_r, E_θ, and E_φ. For NF-focused array, the radial component of the electric field E_r is very small and can be ignored in the near field region [24]. Thus, only the components E_θ and E_φ are used to calculate the axial ratio. The AR in the area of 20 × 20 cm^2 of the transverse plane at focal point 40 cm away from the NF array aperture is shown in Fig. 9. The NF-focused array exhibits focused circular polarization in area around the focal point less than that for the uniformly phased array. The variations of the normalized power density along x-axis and y-axis for the uniformly phased array and NF- focused array are shown Fig. 10. The side lobe level, SLL, in the 32 × 32 cm^2 area around the focal point is less than -13.5 dB while -5.82 dB for the uniformly phased array. Approximately the same field distributions in the far- field region for the uniformly phased array are obtained in the near field region for the NF-focused array due to the phase correction of each element in the array.

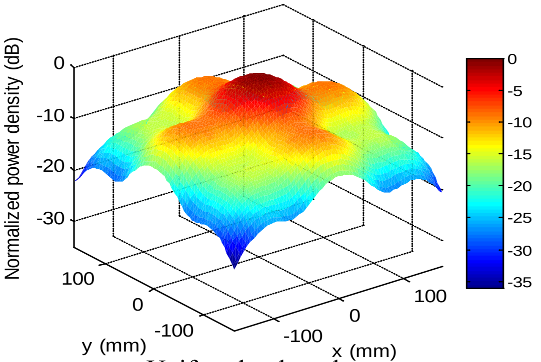

a. Uniformly phased array

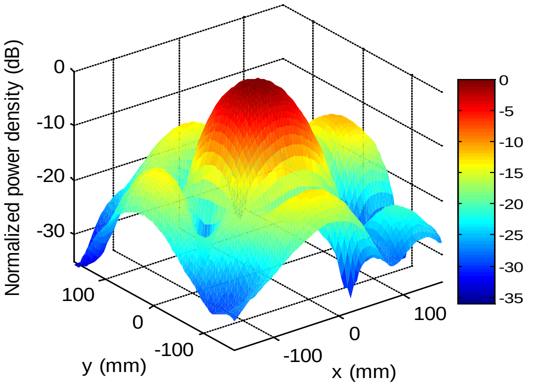

b. NF- focused array

Fig. 6. A 3-D plot of the simulated normalized power density of the 8×8 CDRA at z=R_o=40 cm.

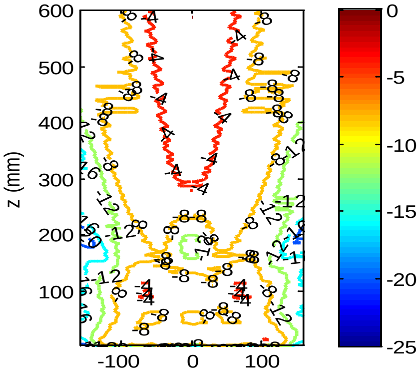

a. Uniformly phased array

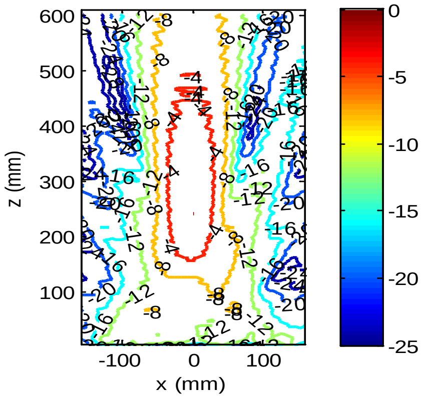

b. NF- focused array

Fig. 7. A contour plot of the simulated normalized power density of the 8×8 CDRA in the x-z plane at y=0.

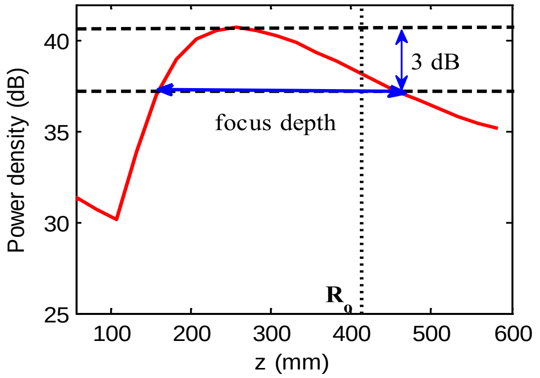

Fig. 8. Simulated radiated power density along the axial direction for the NF-focused CDRA array with supporting arms at x=y=0.

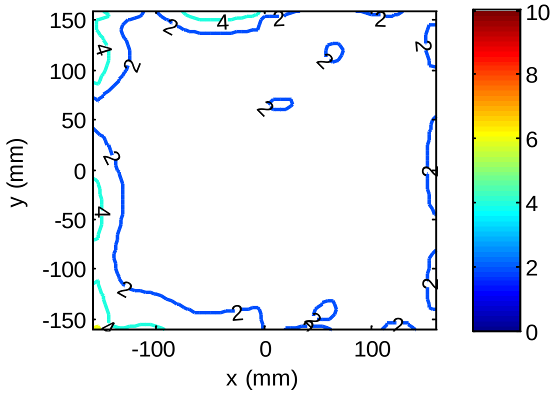

a. Uniformly phased array

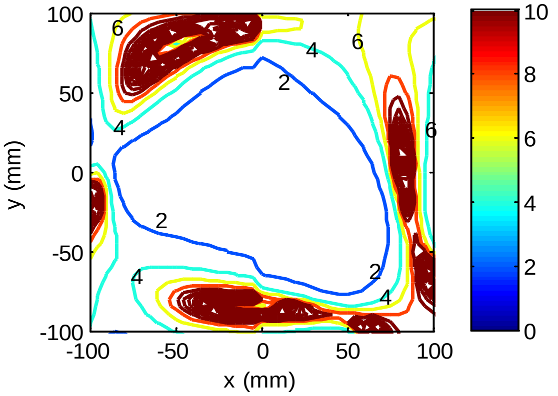

b. NF focused array

Fig. 9. Contour plot of the simulated axial ratio in 20 ×20 cm^2 area at $z=R_o= 40$ cm from the antenna aperture.

IV. CONCLUSION

The performance of the proposed NF- focused CDRA array compared with the uniformly phased CDRA array has been presented. The NF-focused CDRA array is maximizing the radiated power at a limited size spot of radius 6.5 cm in the focal plane at 40 cm from the array aperture with a 3-dB focus depth of 31.2 cm along the axis normal to the array aperture. The NF- focused array produces a far-field like pattern in the near–field at the focal plane. Thus, the near field focused array will improve the performance of the reader antenna for the RFID application, and consequently improve the detectability of the tagged objects in the near field.

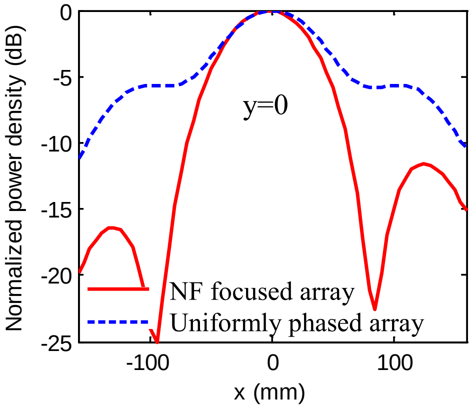

a. x- axis

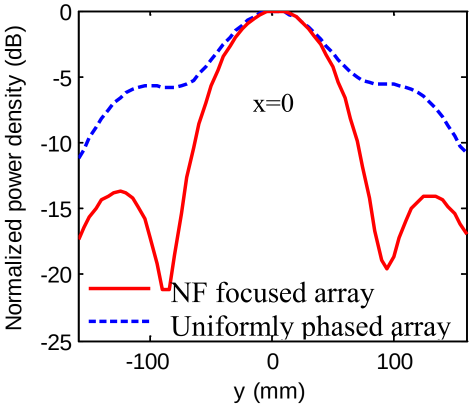

b. y-axis

Fig. 10. Simulated normalized power density along the transverse direction at $z=R_o= 40$ cm from the antenna aperture.

REFERENCES

[1] K. Finkenzeller, RFID Handbook: Radio-Frequency Identification Fundamentals and Applications, 2nd Ed., *Wiley & Sons, Inc.*, New Jersey, USA, 2004.

[2] R. Bhochhibhoya, Mobile Tag Reading in a Multi-Reader RFID Environment, *M. Sc. Thesis, Pokhara University,* Nepal, India, 2005.

[3] W. Arts, E.D. Mulder, B. Preneel, G.A. Vandenbosch, and I. Verbauwhede, “Dependence of RFID Reader Antenna Design on Read Out Distance,” *IEEE Trans. on Antennas and Propag.*, vol. 56, no. 12, pp. 3829-3837, December 2008.

[4] S. H. Zainud-Deen, Hend A. Malhat, and K. H. Awadalla, “Circular Polarized Dielectric Resonator Antenna for Portable RFID Reader using a Single Feed,” *International Journal of Radio Frequency Identification & Wireless Sensor Networks*, vol. 1, no.1, 2011.

[5] S. H. Zainud-Deen, H. A. Malhat, and K. H. Awadalla, “Octafilar Helical Antenna for Handheld UHF-RFID Reader,” *International Journal of Radio Frequency Identification & Wireless Sensor Networks,* vol. 1, no. 1, 2011.

[6] C. F. Tseng, C. L. Huang, and C. H. Hsu, “A Wideband Planar Inverted-F Dielectric Resonator Antenna for RFID System Applications,” *Microwave and Opt. Tech. Letters*, vol. 48, no. 7, pp. 1302-1305, July 2006.

[7] Z. Sun, S. S. Zhong, X. R. Tang, and K. D. Chen, “Low-Side Lobe Circular-Polarized Microstrip Array for 2.45 GHz RFID Readers,” *Microwave and Opt. Tech. Letters.,* vol. 50, no. 9, pp. 2235-2237, September 2008.

[8] M. Abbak, and I. Tekin, “RFID Coverage Extension using Microstrip-Patch Antenna Array,” *IEEE Antennas and Propag. Magazine,* vol. 51, no. 1, pp. 185-191, February 2009.

[9] M. Bogosanovie and A. G. Williamson, "Microstrip Antenna Array with a Beam Focused in the Near Field Zone for Application in Noncontact Microwave Industrial Inspection," *IEEE Trans. on Instruments and Measurements,* vol. 56, no. 6, pp. 2186-2495, December 2007.

[10] J. T. Loane and S. Lee, "Gain Optimization of Near Field Focusing Array for Hyperthermia Applications," *IEEE Trans. on Microwave Theory and Techniques*, vol. 37, no. 10, pp. 1629-1635, October 1989.

[11] F. R. L. Silva, M. T. de Melo, and M. D. Lourenço O. Junior, “Coplanar Antenna Array Design with Stubs over Dipoles for RFID Applications,” *Microwave and Opt. Tech. Letters*, vol. 50, no. 4, pp. 877-879, April 2008.

[12] H. T. Chou, T. M. Hung, N. N. Wang, H. H. Chou, C. Tung, and P. Nepa, "Design of a Near Field Focused Reflectarray Antenna for 2.4 GHz RFID Reader Applications," *IEEE Trans. Antennas Propag.*, vol. 59, no. 3, pp. 1013-1018, March 2011.

[13] H. T. Chou, C. Tung, T. M. Hung, H. H. Chou, and P. Nepa, “Design of a Near Field Focused Reflectarray Antenna for RFID Reader Applications,” *in Proc. IEEE Antennas and Propag. Soc. Int. Symp.*, vol. 48, Toronto, Canada, June 2010.

[14] S. H. Zainud-Deen, H. A. Malhat, and K. H. Awadalla, “Near-Field Focused DRA Array for Fixed RFID Reader,” *International Journal of Radio Frequency Identification & Wireless Sensor Networks,* vol. 1, no. 1, 2011.

[15] R. Siragusa, P. Lemaître-Auger, and S. Tedjini, “Tuneable Near-Field Focused Circular Phase-Array Antenna for 5.8-GHz RFID Applications,”

IEEE Antennas and Wireless Propag. Letters, vol. 10, pp. 33-36, January 2011

[16] R. Schuhmann, T. Weiland, W. H. Schilders, E. J. Maten, and S. H. Houben, "Recent Advances in Finite Integration Technique for High Frequency Applications," *Scientific Computing in Electrical Engineering,* vol. 4, pp. 46-57, 2004.

[17] J. L. Volakis, A. Chatterjee, and L. C. Kempel, "Finite Element Method for Electromagnetic: Antennas, Microwave Circuits, and Scattering Applications," *IEEE Press*, Piscataway, NJ, 1998.

[18] M.T. Sebastian, Dielectric materials for Wireless Communication, *Elsevier Ltd.*, 2008.

[19] R. Chair, A. A. Kishk, and K. F. Lee, "Experimental Investigation for Wideband Perforated Dielectric Resonator Antenna," *Electronic Letters*, vol. 42, no. 3, pp. 137-139, Feb. 2006

[20] Y. Zhang and A. A. Kishk, "Analysis of Dielectric Resonator Antenna Arrays with Supporting Perforated Rods," *2nd European Conf. on Antennas and Propag., (EuCAP 2007)*, pp. 1-5, 2007.

[21] M. Hansishi and H. Takazawa, "Broad Band Circularly Polarized Planar Array Composed of a Pair of Dielectric Resonator Antennas," *Electronics Letters,* vol. 21, no. 10, pp. 437-438, May 1985.

[22] R. C. Hansen, "Focal Region Characteristics of Focused Array Antennas," *IEEE Trans. Antennas Propag.,* vol. 33, no. 12, pp. 1328-1337, December 1985.

[23] Y. Adanel, M. Wongl, C. Dale', and J. Wiartl, "Near Field Power Density Characterization of Radio Base Station Antennas using Spherical Harmonics Optimization Techniques," *European Conference on Wireless Technology, Amsterdam*, Holland, pp. 121-124, 2004.

[24] A. J. Fenn, "On the Radial Component of the Electric Field for a Monopole Phased Array Antenna Focused in the Near Zone," *IEEE Trans. Antennas Propag.,* vol. 40, no. 6, pp. 723-727, June 1992.

S. H. Zauind-Deen: (S'81-M'88) was born in Menouf, Egypt, on November 15, 1955. He received the B.Sc. and M.Sc. degrees from Menoufia University in 1973 and 1982, respectively, and the Ph.D. degree in Antenna Engineering from Menoufia University, Egypt in 1988.

He is currently a professor in the Department of Electrical and Electronic Engineering in the Faculty of Electronic Engineering, Menoufia University, Egypt. His research interest at present includes microstrip and leaky wave antennas, DRA, RFID, optimization techniques, FDFD and FDTD, scattering problems, and breast cancer detection.

Hend A. Mahat: was born in Menouf, Egypt, on December 12, 1982. She received the B.Sc. and M.Sc. degrees from Menoufia University in 2004 and 2007, respectively, and the Ph.D. degree in Antenna Engineering from Menoufia University, Egypt in 2011.

She is currently a lecturer in the Department of Electrical and Electronic Engineering in the Faculty of Electronic Engineering, Menoufia University, Egypt. Her research interest at present includes Transmitarray, reflectarray, DRA, RFID, and wavelets technique.

K. H. Awadalla: was born in El-Santa – Gharbiya - Egypt, on February 1, 1943. He received the B.Sc. and M.Sc. from Faculty of Engineering, Cairo University, Egypt, in 1694 and 1972, respectively, and the Ph.D. degree from University of Birmingham, UK. in 1978.

He is currently a Professor emeritus in the Dept. of Electrical and Electronic Engineering in the Faculty of Electronic Engineering, Menoufia University, Egypt. His research interest at present includes microtrip and leaky wave antennas, DRA, RFID, and optimization techniques.

Design of N-Channel Rotary Joint using Curved Double-Ridged Waveguide and Concentric Coaxial Lines

Alireza Mallahzadeh and Hadi Ahmadabadi

Faculty of Engineering, Shahed University, Tehran, Iran
mallahzadeh@shahed.ac.ir , ahmadabadi@shahed.ac.ir

Abstract ─ In this paper, a general design method for a special kind of N-channel rotary joint is presented. The N-channel configuration is achieved by using transition between concentric coaxial lines and double-ridged waveguides. Design of double-ridged waveguides for the purposed transition is also presented. Based on this method, an ultra wide band six-channel rotary joint is designed for a frequency band of 8 to 18 GHz. A full-wave numerical simulation tool is used to optimize the geometry of the proposed six-channel rotary joint to achieve a compact size, wide bandwidth operation, and low insertion loss. Simulated results show the insertion loss of less than 0.5 dB and VSWR ≤ 2 for all channels over the entire frequency bandwidth. Finally, the sensitivity analysis is done to obtain the effect of the manufacturing tolerances on performances of the rotary joint.

Index Terms ─ Concentric coaxial lines, double-ridged waveguide, rotary joint.

I. INTRODUCTION

The rotary joint is an integral part of rotational microwave communication systems, such as spacecrafts [1] and tracking radar systems [2]. It is an electromechanical device that provides a critical interface between the stationary and rotating section of system, allowing signals to be transmitted back and forth between the antenna and pedestal with little distortion and low insertion loss. Although different types of rotary joints are used extensively in commercial and military applications but they have not been reported in the open literature.

In radars or seeker antennas, it is often necessary to have a multi-channel rotary joint to transmit two or more RF signals through a rotational axis. The operation frequencies of channels are dependent on their applications so channels can operate at the same or different frequencies. The connection of multi-channel rotary joint to the antenna, i.e., movable part of system, and the stationary part of system is through transmission lines which support circularly symmetric propagating modes. These types of modes are needed to avoid distortion of signal when it is transmitted along the axis of rotation, due to rotation of device around the axis. The transmission lines which support the propagation of circularly symmetric modes are circularly waveguides excited in the TM_{01}, TE_{01}, or circularly polarized modes and coaxial lines which propagate TEM mode. These propagating modes have radial electromagnetic fields distribution and fields are only the function of radius, so their propagation is not affected by rotation of rotary joint and the phase shift is small due to rotation. Rotary joints which use circular waveguide with the TM_{01} or TE_{01} modes have low insertion loss and high power handling capability. The operational bandwidths of these types of rotary joints are limited by the bandwidth of the transducers which are used for excitation of these modes [3] and are also limited by the generation of higher order modes. The rotary joints that use the circular waveguide with circularly polarized mode have wider bandwidth compared to TE_{01} or TM_{01} modes [4]. The disadvantage of mentioned rotary joints is the difficulty in design of multi-channel configurations. The TEM coaxial line has wider single mode operation compared to cylindrical

Submitted On: Aug 21, 2011
Accepted On: Jan 26, 2012

waveguide and multi-channel rotary joint can be designed by using concentric coaxial lines configuration [1, 5]. But the rotary joints which use the coaxial transmission line contain transition of coaxial line to rectangular waveguide that often prevent the rotary joint from being a wideband structure [5]. Forward-mounted antennas in the missile function in the role of seeker of target. If the seeker antenna beams steers mechanically, a rotary joint is needed to transmit the received signals by the antenna to stationary part of system. These signals are utilized to guide the missile to the target. In this paper wideband characteristics and N-channel configuration of the seeker antenna rotary joint are achieved through utilizing of double-ridged waveguides together with concentric coaxial transmission lines. Double-ridged waveguides have preferential features for using in broadband applications such as low cutoff frequency and wide bandwidth. Ridged waveguides satisfy requirements of applications that need to have a transmission line with a single mode of propagation over extensive bandwidth. For a given frequency bandwidth, ridged waveguides have smaller cross section compared to conventional rectangular waveguides. An additional advantage follows from the fact that the ridged waveguides have low and flat characteristic impedance compatible with the coaxial line. The above mentioned features of ridged waveguides make them suitable candidates for using in rotary joint. In the following, the configuration of N-channel rotary joint is described and then designs of different part of it are presented in detail.

II. DESIGN CONSIDERATIONS

A. N-channel rotary joint configuration

Figure 1 shows configuration of the designed rotary joint. This configuration consists of N double-ridged waveguides. Each of the waveguides is considered as a channel to transfer signals between the two coaxial lines which are at right angles and are connected to the antenna and pedestal. Coaxial lines, which their axes are aligned with x axis, are considered for connecting to the stationary part of the system or pedestal and coaxial lines with axes aligned with y axis are connected to antenna. Due to need of rotation around the unique axis, use of coaxial line with separate axes is impossible therefore concentric coaxial lines are used. Because of the right angle between input and output port of each channel, double-ridged waveguide must have curved form to make the connection between two coaxial lines possible. Curved forms of waveguides provide the advantage of having a compact structure since they can be arranged circularly around a center in a cylindrical volume. In this configuration t,he number of channels is even and they are completely isolated. The operating frequency of each channel depends on dimensions of its waveguide and coaxial line. As depicted in Fig. 1(b), N-channel rotary joint consists of transitions from N/2 coaxial lines with concentric configuration to N/2 double-ridged waveguides placed next to each other, with different dimensions that must be designed.

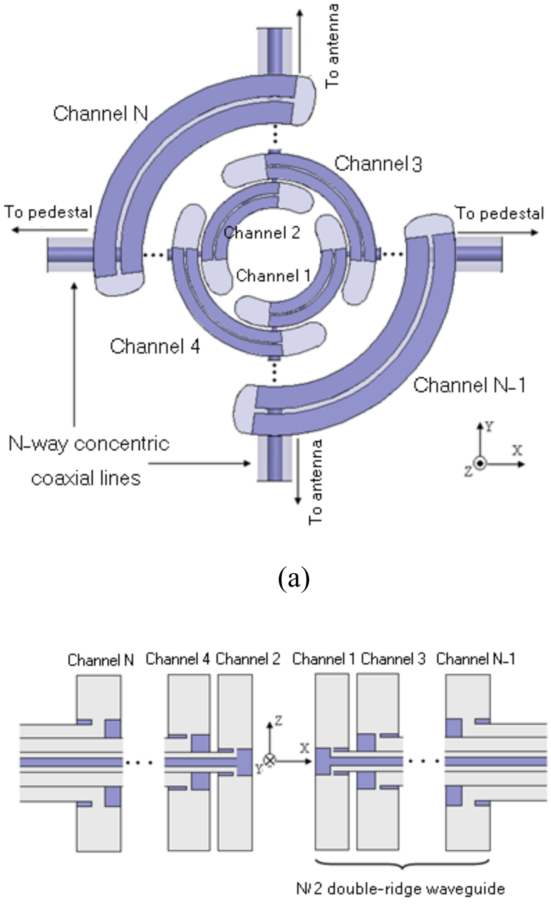

(a)

(b)

Fig. 1. Configuration of N-channel rotary joint. (a) Top view. (b) Cutaway in XZ plane.

B. Design of double-ridged waveguides

In Fig. 2, the transition between N concentric coaxial lines to N double-ridged waveguides placed next to each other is shown. Concentric coaxial lines contain N+1 conductors comprising N coaxial transmission lines. Diameters of outer and inner conductors of the nth coaxial line are denoted by D_{n+1} and D_n , respectively, so the characteristic impedance of the nth line is given by:

$$Z_n = \frac{60}{\sqrt{\varepsilon_r}} \ln \frac{D_{n+1}}{D_n}, \qquad (1)$$

where ε_r is the relative permittivity of insulator filled between lines. The signal of nth coaxial line is coupled to nth double-ridged waveguide. To have a well-matched transition between the coaxial line with predetermined arbitrary line impedance and the double-ridged waveguide, following design considerations must be taken into account:

1- The characteristic impedance of double-ridged waveguide must be as close as possible to the predetermined impedance of coaxial line.
2- The size of outer diameter of the nth coaxial line should be close to the ridge width of nth waveguide.
3- The cutoff frequency of TE_{10} mode of double-ridged waveguide must be excited before than the low end of the desired band, and cutoff frequencies of higher TE_{m0} modes, especially odd modes, must be larger than the high end of band.
4- The higher non-TEM modes of coaxial line must be cutoff in desired bandwidth. The second propagating mode in the coaxial line is the TE_{11} mode. The cutoff frequency of the TE_{11} mode of nth coaxial line is approximately given by[6]:

$$f_c = \frac{c}{\pi\sqrt{\varepsilon_r}\,(D_{n+1} + D_n)}, \qquad (2)$$

where c is the speed of light in the free space.

Taking into account of above considerations also avoids propagation of higher order modes in all channels. Some undesired modes can be excited in the vicinity of junction but they are evanescent.

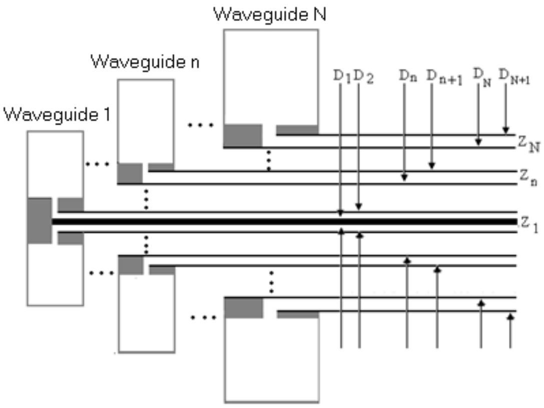

Fig. 2. Transition of N concentric coaxial lines to N double-ridged waveguides.

For the purposed transition, the cutoff frequencies of first propagating mode and higher order modes need to be determined for designing of each double-ridged waveguide. Hopfer [7] presented curves to determine cutoff frequencies for specified aspect ratio but they are not applicable to this design since to meet the characteristic impedance criterion different aspect ratios are needed. Pyle [8] extended the work of Hoefer and presented the design data for ridged waveguides of any aspect ratio but without considering characteristic impedances of waveguides. In 1982, closed form expressions, for calculating the cutoff frequency of TE_{10} mode and the characteristic impedance of double-ridged waveguide were obtained by perturbation theory [9]. The cutoff frequency of the double-ridged waveguide, with cross section as depicted in Fig. 3, is given by the following formula

$$f_c = \frac{1}{2(a-s)\sqrt{\varepsilon_r \mu_r}}[1 + \frac{4}{\pi}\left(1 + 0.2\sqrt{\frac{b}{a-s}}\right)\frac{b}{a-s}.$$

$$\ln\csc\frac{\pi}{2}\frac{d}{b} + (2.45 + 0.2\frac{s}{a})\frac{sb}{d\left(a-s\right)}]^{-\frac{1}{2}}, \qquad (3)$$

where a and b are the waveguide width and height, respectively, s is the ridges width and d is the spacing of two ridges. This formula has 1 percent accuracy in determining the cutoff frequency with parameters in the following ranges:

$$0.01 \le \frac{d}{b} \le 1$$

$$0 < \frac{b}{a} \le 1$$

$$0 \le \frac{s}{a} \le 0.45$$

And the characteristic impedance obtained by voltage-power approach is

$$Z_0 = Z_{0\infty}\left[1-\left(\frac{f_c}{f}\right)^2\right]^{-\frac{1}{2}}, \tag{4}$$

where

$$Z_{0\infty} = \frac{120\pi^2\,(\frac{b}{\lambda_c})}{\frac{b}{d}\sin\pi\frac{s}{b}\frac{b}{\lambda_c}+[\frac{B_0}{Y_0}+\tan\frac{\pi}{2}\frac{b}{\lambda_c}(\frac{a-s}{b})]\cos\pi\frac{s}{b}\frac{b}{\lambda_c}}. \tag{5}$$

$Z_{0\infty}$ is the characteristic impedance when frequency approaches infinity and λ_c is related to cutoff frequency by $\lambda_c = c / f_c$. The use of (3) and (4) is easy so are chosen for designing of the waveguides.

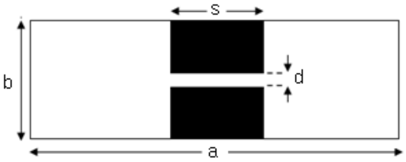

Fig. 3. Cross section of double-ridged waveguide.

Cutoff frequencies of higher order modes can be determined by applying the transverse resonance method. The following transcendental equations are obtained for TE_{m0} cutoff frequencies [7]. For m odd

$$\cot\frac{\pi(a-s)}{\lambda_c} - \frac{b}{d}\tan\frac{\pi s}{\lambda_c} - \frac{B}{y_0} = 0. \tag{6}$$

And for m even

$$\cot\frac{\pi(a-s)}{\lambda_c} + \frac{b}{d}\cot\frac{\pi s}{\lambda_c} - \frac{B}{y_0} = 0. \tag{7}$$

The (6) and (7) must be solved for λ_c to determine the cutoff wavelengths or frequencies of TE_{30} and TE_{20}, respectively. In the above equations, the term B/y_0 is the normalized discontinuity susceptance of ridges obtained by Marcuvitz [10]. The cutoff frequency of TE_{20} is slightly varied by changing the dimensions of the ridges. Its value depends mainly on the value of the waveguide width, so the choice of the cutoff frequency of TE_{20} mode upper than the high end of the bandwidth, approximately determines the size of waveguide width [11]. The dimension of ridge width can be adjusted by considering the cutoff frequency of the TE_{30} mode and the attenuation of waveguide. After selecting the waveguide and ridge width, the (3) and (4) must be solved for various values of b and d to obtain dimensions which satisfy the required cutoff frequency and characteristic impedance of the first propagating mode. Finally, for the determined values of waveguide dimensions, the (6) and (7) must be solved for f_c to ensure that the cutoff frequencies of higher order modes are larger than the high end of the frequency band.

C. Design of rotary joint channels

The structure of one channel of the rotary joint is depicted in Fig. 4. It consists of two coax to double-ridged waveguide transformers and a uniformly curved form of double-ridged waveguide. In the design of the purposed rotary joint, it is important to keep the overall configuration compact; therefore, the radius of the curvature of the waveguide should be chosen as little as possible. The radius of the curvature of the waveguide must also be chosen such that the VSWR contribution due to the curved form of the waveguide becomes negligible in the whole bandwidth. In the transition of the coax to the curved double-ridged waveguide, three parameters are important to achieve good VSWR. They are the shape and the length of the cavity and the lengths of the two ridges which means where these two ridges stop in the cavity [12, 13].In this design the cavity of transformer has the same curvature of waveguide to reduce the reflection between the waveguide and transformer. To improve the VSWR, the junctions of the outer and inner conductors of the coaxial line must be as close as possible to the end of ridges inside the transformer; it means that the ridges must stop close to the junction inside the cavity. Finally, the end of the cavity has to be shorted by properly shape plate which results in the best VSWR.

III. DESIGN OF SIX-CHANNEL ROTARY JOINT

In this section based on suggested design method, a six-channel rotary joint has been designed and simulated for the frequency bandwidth of 8 to 18

GHz. This frequency bandwidth covers both X and Ku band. These bands are commonly used in the Seeker missile. Figure 5 shows the configuration of the six-channel rotary joint. It has the same configuration of the N-channel prototype, but is placed inside an aluminum body. Due to the symmetry of the rotary joint, the configurations of channels 1, 2, and 3 are exactly the same as channels 4, 5, and 6, respectively, so in the following just designs and simulations of channels 1 to 3 are presented. As depicted in Fig. 5(b), there is a transition between three concentric coaxial lines and three double-ridged waveguides, so three double-ridged waveguides have to be designed for the frequency bandwidth of 8 to 18 GHz with the assumption that line impedances of all concentric coaxial lines are 50 Ω. This transition is shown separately in Fig. 6. It follows from the (1) that the relationship between the diameters of three 50 Ω air filled coaxial lines with concentric configuration, as depicted in Fig. 6, is

$$D_3 = 2.3 \times D_2 = 2.3 \times 2.3 \times D_1. \quad (8)$$

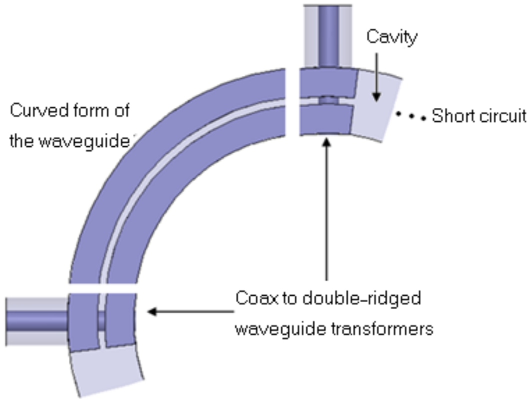

Fig. 4. Structure of one channel of rotary joint.

As mentioned above, choosing the ridge width of waveguide close to the outer diameter of the coaxial line provides better transition so the ridges widths of three waveguides must be close to D_1, D_2, and D_3, so ratios between the ridges widths of adjacent waveguides must be about 2.3. This causes difficulties in the design of double-ridged waveguides, since three waveguides with different ridges widths and the same operating bandwidth are needed. In double-ridged waveguides, operating bandwidth is the frequency range in which there is just one propagating mode, but this bandwidth is not the useful bandwidth, so the cutoff frequency of the dominant mode is commonly chosen 15 to 25 percent lower than the low end of the desired bandwidth [7]. Assuming the operating bandwidth between 8 to 18 GHz, three waveguides with different dimensions must be designed by considering the following constraints:

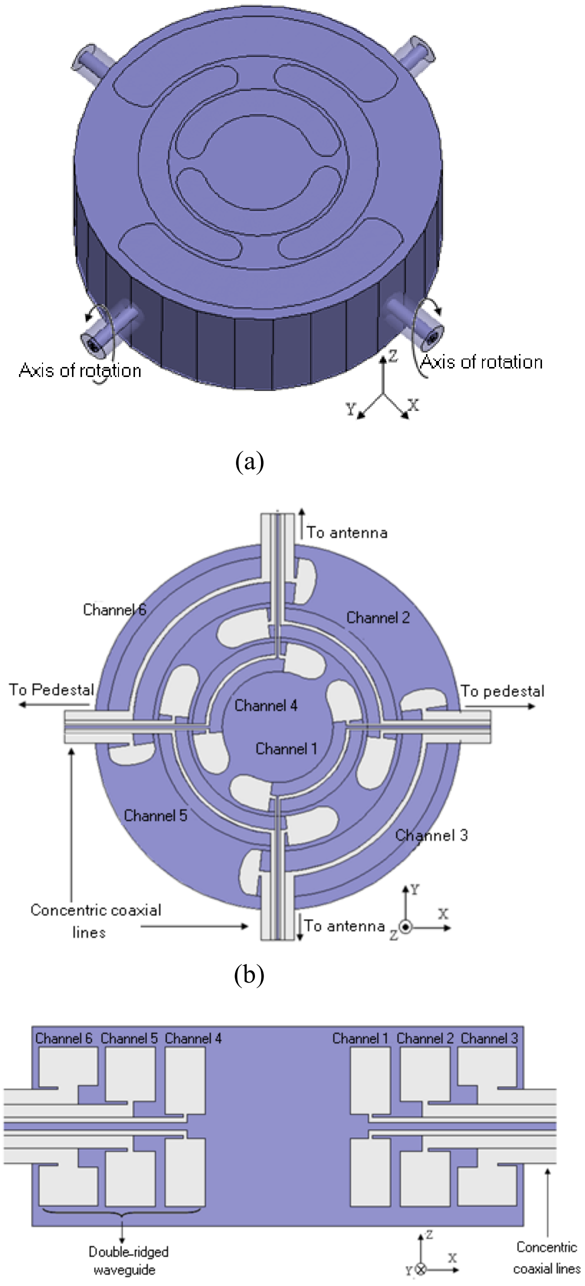

(a)

(b)

(c)

Fig. 5. Configuration of six-channel rotary joint. (a) 3D view. (b) Cutaway view in XY plane. (c) Cutaway in XZ plane.

1- Cutoff frequencies of their dominant modes should be lower than 6 GHz (25% of the 8 GHz).
2- Higher propagating modes especially TE_{30} must be excited above the 18 GHz.
3- Characteristic impedances of waveguides must be around 50 Ω.
4- Ratios of ridges widths of adjacent waveguides must be approximately 2.3.

The design is based on the method mentioned previously. The cutoff frequency of the TE_{20} mode depends on the size of the waveguide width. Its size is chosen to be 16 mm for three waveguides. Larger width of the ridge leads to larger attenuation in the double-ridged waveguide [14] so width of ridge must be small as possible to keep the attenuation or insertion loss low.

As mentioned previously, the ridge width also is limited by the cutoff frequency of the TE30 mode which can be coupled to coaxial line. For these reasons the ridge width of waveguide 3 is chosen 1/4 of waveguide width, i.e. 4 mm. by considering (8), this size leads to 1.73mm and 0.75 mm for ridges widths of waveguides 2 and 3, respectively.

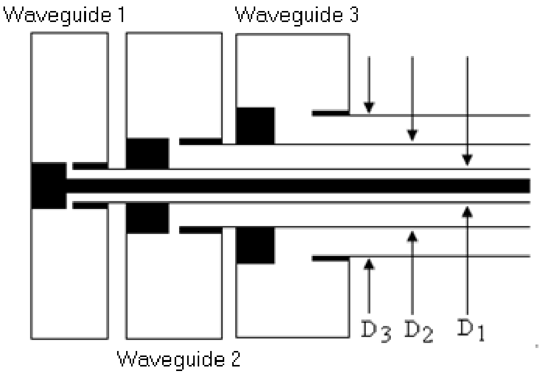

Fig. 6. Transition of three concentric coaxial lines to double ridged waveguide.

Since the power-handling capacity of rotary joint is not of concern, the aspect ratio of waveguides can be arbitrary. The double-ridged waveguide characteristic impedance increases with the spacing between ridges and inversely with the ridge width hence, ridges spacing must be decreased from waveguides 3 to 1. Finally for values of ridges spacing and waveguides heights which satisfy the previously mentioned requirement, nonlinear equations (4) and (5) have been solved by the least squares method [15]. Bandwidth specifications of the designed waveguides are presented in Table 1 and the characteristic impedances of them are depicted in Fig. 7. It can be seen that their values are in the range of 40 to 50 Ω in the entire bandwidth. Designed waveguides must be curved. The radiuses of curvatures of the waveguides of channels 1 to 3 have been optimized by HFSS [16]. The VSWR of the curved form of double-ridged waveguides are plotted in Fig. 8 which are lower than 1.06 across the whole bandwidth. Each curved waveguide is connected to two coax to waveguide transformers which their design method mentioned before. The end of the cavity has been shorted by various shapes of plates and the elliptical shape of the shorting plate resulted in the best results. The complete geometry of each channel can be described by means of angles of waveguide and ridge sectors, as shown in Fig. 9. The geometry of each channel has been modeled by HFSS and optimizations have been carried out for these parameters.

In Table 2, values of θ_i and radiuses of curvatures which result in desired properties of rotary joint are presented. Simulated insertion losses of channels are shown in Fig. 10(a). Their values are better than 0.3 dB for channels 1 and 2 in the frequency range 8 to 18 GHz and the insertion loss of channel 3 is less than 0.5 dB. The VSWR of all channels have acceptable values and are better than 2 over the frequency range of 8 to 18 GHz as depicted in Fig. 10(b).

Table 1: Cutoff frequencies of first three modes of designed waveguide in GHz

Modes	Waveguide A	Waveguide B	Waveguide C
TE_{10}	3.9	4.5	4.6
TE_{20}	23.2	20.7	19.6
TE_{30}	25.2	22.7	20.9

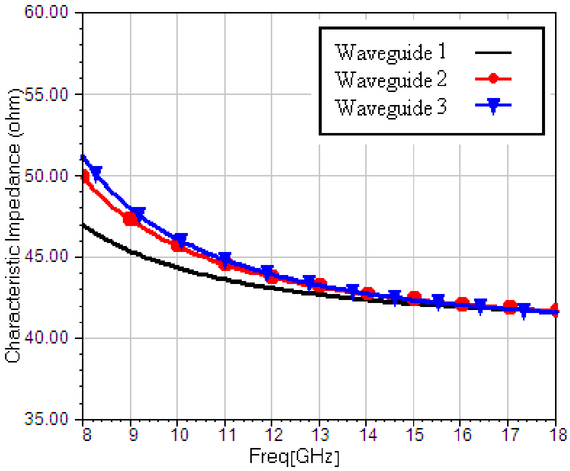

Fig. 7. Characteristic impedances of designed waveguides of channels 1 to 3.

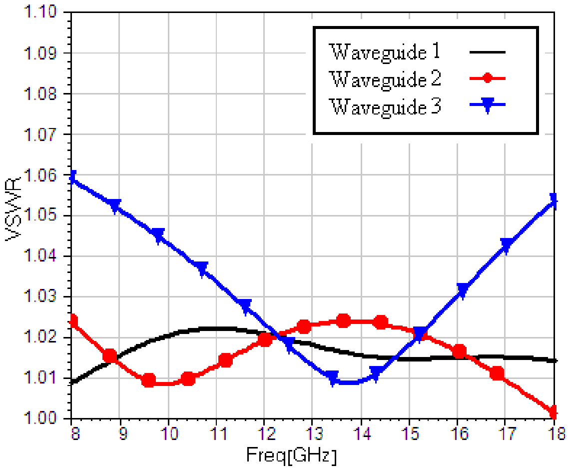

Fig. 8. VSWR of curved form of designed waveguides of channels 1 to 3.

The designed rotary joint must be connected to the stationary part through an appropriate choke types. The use of contacting choke is preferred for the non-contacting type for several reasons. The first reason is that the bandwidth of the contacting choke is greater than its non-contacting type. Although the broadband non-contacting choke can be designed for the coaxial line [17], the concentric configuration of coaxial lines of this rotary joint and its small dimensions makes design and fabrication of the non-contacting choke mechanically and electronically complex. The second reason relates to the rotation speed of the seeker antenna. Since the seeker antenna rotates gently, the contacting choke is suitable.

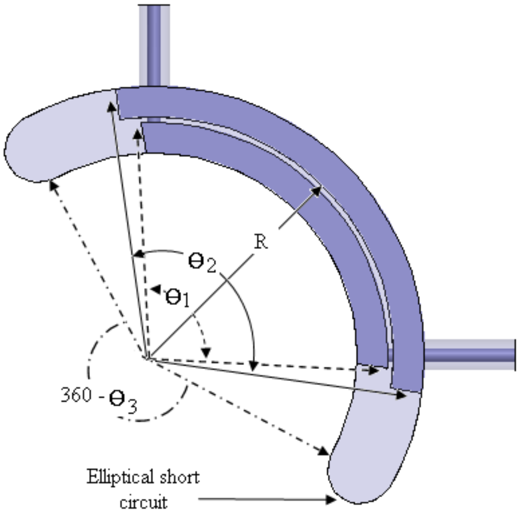

Fig. 9. Description of each channel by angles.

Table 2: Values of θ_i and R for three channels

	Channel1	Channel2	Channel 3
Θ_1(deg)	103	96	94
Θ_2(deg)	105.3	98	95
Θ_3(deg)	111.7	138	125
R(mm)	17.3	12.25	8.8

IV. SENSITIVITY ANALYSIS

In this section, a comprehensive sensitivity analysis is carried out to obtain a clear insight of the effects of manufacturing tolerances on the performance of the proposed rotary joint, especially insertion loss. It reveals that the parts which are most sensitive to tolerances are diameters of coaxial lines. Figure 11 shows the effects of 0.05 mm tolerances of diameters of coaxial lines on the insertion loss for three channels. Tolerances of manufacturing often are less than 0.05mm. The results demonstrate that the most sensitive channel to tolerances is channel 1. It is obvious that the sensitivity increase as dimensions of channel is decreased.

V. CONCLUSIONS

A general design method for an N-channel rotary joint with a novel configuration has been suggested. In this design, double-ridged waveguides and concentric coaxial lines have been

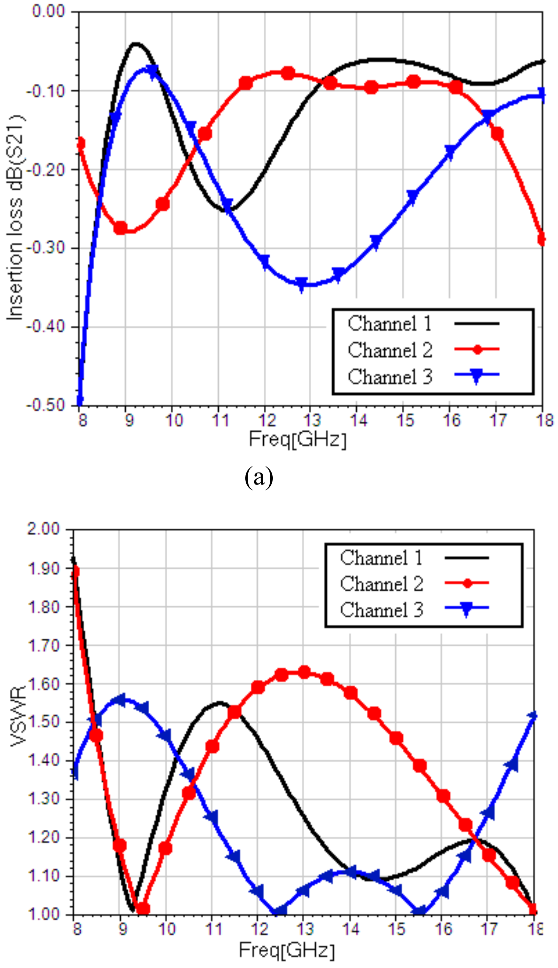

(a)

(b)

Fig. 10. Simulation resluts of six-channel rotary joint. (a) Insertion loss. (b) VSWR.

utilized to achieve simultaneously multi-channel, compact configuration, complete isolation between channels, and wide band characteristics. A six-channel rotary joint has been designed by this method. The structure has been simulated using finite element package, HFSS. The results show the insertion loss of less than 0.5 dB and VSWR of less than 2 for six channels. Finally, the sensitivity analyses have been done to obtain effects of manufacturing tolerances on the characteristics of six-channel rotary joint.

ACKNOWLEDGEMENT

Special thanks to Iran Telecommunication Research Center.

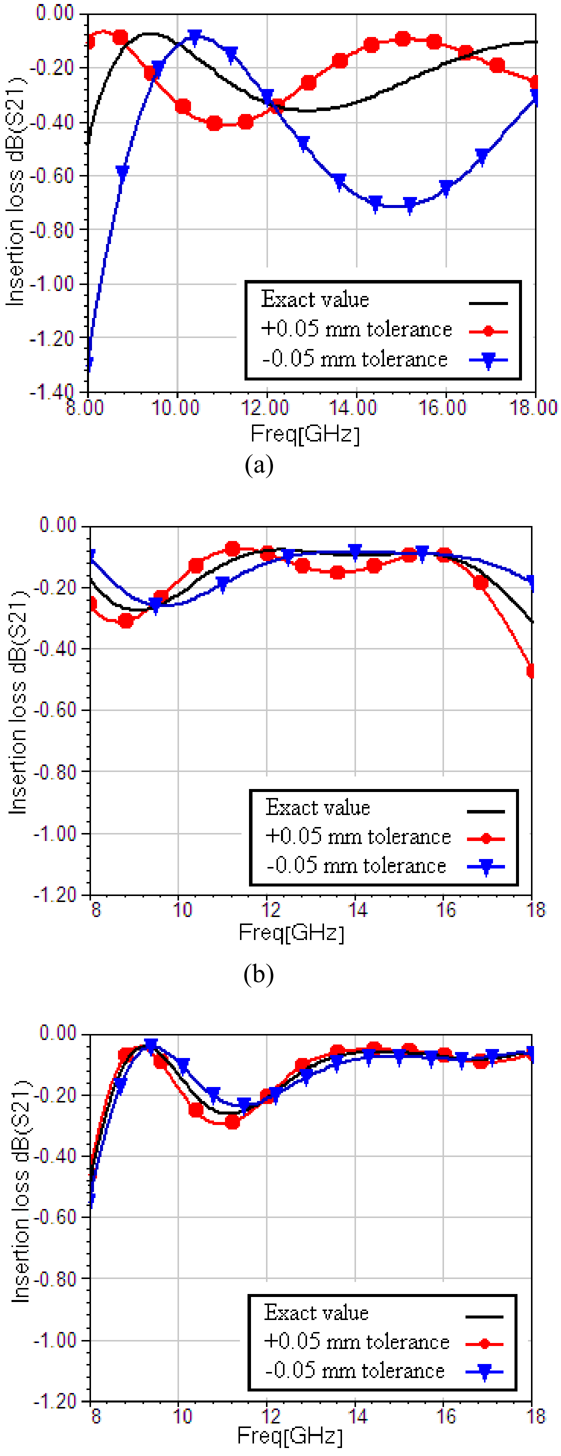

(a)

(b)

(c)

Fig. 11. Variations of insertion loss of channels by considerig tolerances of diameters of coaxial lines. (a) Channel 1. (b) Channel 2. (c) Channel 3.

REFERENCES

[1] W. Matthews and M. A. Ikemoto, "A Multi-Channel Rotary Joint for Spacecraft Applications," *Proc. IEEE*, vol. 72, pp.157-159, May 1972.

[2] K. Rambabu and J. Bornemann "Compact Single-Channel Rotary Joint Using Ridge Waveguide Sections for Phase Adjustment," *IEEE Trans. MTT.*, vol. MTT-51, pp. 1982-1986, August 2003.

[3] S. B. Chakrabarty, V. K. Singh, S. B. Sharma, "TM_{01} Mode Transducer Using Circular and Rectangular Waveguides," *Int. J. RF and Microwave CAE 20*, pp. 259-263, February 2010.

[4] M. Kaiden, K. Kimura, H. Ogawa , T. Kasuga, M. Tsuboi, and Y. Murata, "Septum Polarizer for Ka-Band H-Shaped Rotary Joint," *Int. J. Infrared Millim. Waves 30*, pp. 727-737, April 2009.

[5] S. H. Hajimowlana and M. Kamyab, "Sensitivity Analysis of Curved-Structure Rotary Joint for a Radar System in X-band," *Proc. IEEE*, pp. 330-333, August 1998.

[6] D. M. Pozar, Microwave Engineering, 2nd ed., John Wiley & Sons, Inc., 1998.

[7] S. Hopfer, "The Design of Ridge Waveguides," *IRE Trans. MTT*, vol. MTT-3, pp. 20-29, October 1955.

[8] J. R. Pyle, "The Cutoff Wavelength of the TE_{10} Mode in Ridge Rectangular Waveguide of Any Aspect Ratio," *IEEE Trans. MTT.*, vol. MTT-14, pp. 175-183, April 1966.

[9] J. R. Hoefer, N. Burton, and R. Vahldieck, "Closed-Form Expressions for the Parameters of Finned and Ridge Waveguides," *IEEE Trans. MTT*, vol. MTT-30, pp. 2190-2194, December 1982.

[10] N. Marcuvitz, *Waveguide Handbook. New York*: McGraw-Hill, 1951.

[11] T. N. Anderson, "Double-Ridge Waveguide for Commercial Airlines Weather Radar Installation," *IRE Trans. MTT,* vol. MTT-3, pp. 2-9, July 1955.

[12] T. Rizawa and R. Pendleton, "Broadband Coax-Waveguide Transitions," *Proc. IEEE*, vol. 3, pp. 1824-1826, 1995.

[13] A. R. Mallahzadeh and A. Imani, "Modified Double-Ridged Antenna for 2-18 GHz," *Applied Computational Electromagnetic Society (ACES) Journal*, vol. 25, no. 2, pp. 137-143, February 2010.

[14] W. Sun, C. A. Balanis, "MFIE Analysis and Design of Ridge Waveguides," *IEEE Trans. MTT*, vol. 41, no. 11, pp. 1965-1971, November 1993.

[15] W. Y. Yang, W. Cao, T. S. Chung, and J. Morris, Applied Numerical Methods Using MATLAB, John Wiley & Sons, Inc., 2005.

[16] Ansoft Corporation, USA, http://www.ansoft.com/

[17] H. E. King, "Broad-Band Coaxial Choked Coupling Design," *IRE Trans. MTT*, vol. MTT-8, pp. 132-135, March 1960.

Alireza Mallahzadeh was born in Bushehr, a beautiful city in the south of Iran in 1977. He received the B.S. degree in Electrical Engineering from Isfahan University of Technology, Isfahan, Iran, in 1999 and the M.Sc. degree in Electrical Engineering from Iran University of Science and Technology, Tehran, Iran, in 2001, and the Ph.D. degree in Electrical Engineering from Iran University of Science and Technology, Tehran Iran, in 2006. He is a member of academic staff, Faculty of Engineering, Shahed University. He is interested in numerical modeling, antennas and microwaves.

Hadi Ahmadabadi was born in Tehran, Iran, in 1985.He received the B.S. and M.S. degree in Electrical Engineering from Shahed University, Tehran, Iran, in 2008 and 2011, respectively. He is currently working on shaped reflector Antenna design for GEO satellite. His research interests include the Antenna Design, passive microwave devices, Microwave Measurements and numerical methods in electromagnetic.

An AMC Based Antenna for Telemedicine Applications

Haider R. Khaleel, Hussain M. Al-Rizzo, and Daniel G. Rucker

Department of Systems Engineering
University of Arkansas at Little Rock, Little Rock, AR, 72204, USA
hrkhaleel@ualr.edu, hmalrizzo@ualr.edu, dxrucker@ualr.edu

***Abstract* —** In this paper, we present an antenna design for telemedicine applications operating in the Industrial Scientific Medical (ISM) 2.4 GHz band. The design is based on a printed monopole antenna integrated with an artificial magnetic conductor (AMC) ground plane. The AMC ground plane is utilized to isolate the user's body from undesired electromagnetic radiation in addition to eliminating the antenna's impedance mismatch caused by the proximity to human tissues. Moreover, specific absorption rate (SAR) is analyzed based on a numerical human body model (HUGO) to assess the design feasibility. Results show that the radiation characteristics, impedance matching, and SAR values of the proposed design are significantly improved compared with conventional antennas.

***Index Terms*—** Artificial magnetic conductors (AMCs), printed monopoles, specific absorption rate (SAR), telemedicine.

I. INTRODUCTION

Telemedicine has evolved tremendously during the past decade due to the increasing demand for remote monitoring of human vital signs. Telemedicine applications involve but are not limited to seniors monitoring, post surgery patients recovery tracking, and monitoring the body performance of astronauts and athletes during exercise [1]. The health parameters that may be transmitted wirelessly to remote stations (off body mode) in telemedicine systems range from heart rate, blood pressure, body temperature to blood glucose levels and ECG wave forms [2]. In addition to off body applications, on body mode is also necessary for communication between sensor devices located on or within the patient's body [3]. For optimal performance, wearable antennas are required to be small in size, lightweight, and robust. They also have to be comfortable and conformal to the body shape, yet they must maintain high performance in terms of reliability and efficiency. Electro textile based antennas seem to be a low profile solution for a wearable application; however, they are prone to discontinuities in substrate material, fluids absorption, bending, and compression [4]. Microstrip antennas in general offer favorable characteristics in terms of radiation characteristics (directional radiation pattern which is desired in telemedicine application i.e. radiates outside the patient's body). Furthermore, microstrip antennas offer a low profile construction, low cost, and ease of fabrication; however, they suffer from a very narrow bandwidth, that is, any minor shift in the resonant frequency would cause a channel disconnection. Thus, a low profile antenna with hemi spherical radiation pattern and a relatively wide bandwidth is needed to be employed in this application.

Previous work was primarily focused on achieving an omni-directional radiation pattern [5, 6]. However, a uni-directional radiation pattern of the patch antenna is favorably desired in wearable applications, to avoid unnecessary radiation exposure to the human body, radiation losses and impedance mismatch.

Several techniques [7-10] have been reported to solve the aforementioned issues including the use of cavities, absorbers, and shielding planes. However, these techniques lead either to an unacceptable increase in the antenna's height, or a more complicated manufacturing process. In [8], a

Submitted On: July 28, 2011
Accepted On: Dec 18, 2011

reflector patch element is utilized to decrease the rear directed radiated field. The performance of this technique is highly dependent on the ground plane size, furthermore, it is based on a stack of multiple (five) layers which leads to a complex high profile system. In [9], a study on the effects of including conductive materials within cell phones for reducing SAR has been presented. The study demonstrated that the position of the shielding material is an important factor to the technique's effectiveness. In [10], a single negative (SNG) metamaterial is utilized to suppress the EM wave propagating towards the human body, though efficient, it does not offer a low profile solution.

In this paper, we propose a compact printed monopole antenna integrated with an artificial magnetic conductor (AMC) ground plane which is utilized to reflect the electromagnetic radiation in phase in order to minimize the radiation exposure towards the user's body and eliminating the antenna's impedance mismatch caused by the proximity of human tissues. It is well known that a perfect electric conductor (PEC) has a reflection phase of 180° for a normally incident plane wave, while a perfect magnetic conductor (PMC), which does not exist in nature, has a reflection phase of 0° [13]. Image theory states that a PEC ground plane causes the antenna's current and its image to cancel each other, in other words shorting the antenna. This is responsible for dropping the real part of the antenna impedance towards zero ohms, while the imaginary impedance approaches infinity. Thus, a significant amount of the electromagnetic energy is trapped between the antenna and the ground plane; hence, the antenna can no longer radiate efficiently. This is the opposite scenario if an AMC is placed instead of PEC due to its reflection of electromagnetic wave with zero phase shift.

In Section II, we present the description of our proposed design and principle of operation. In Section III, we discuss the radiation characteristics and performance of the antenna system on a numerical human model. In Section IV, the specific absorption rate (SAR) is evaluated for the design with and without the AMC structure for comparison purposes. Finally, conclusions are given in Section V.

II. ANTENNA SYSTEM DESIGN

The proposed antenna along with the AMC structure was designed and optimized using CST Microwave Studio which is based on the finite integration technique (FIT) [11]. For validation purposes, Ansoft HFSS which is based on the finite element method (FEM) [12] is used for further results verification.

A. Antenna design

The proposed antenna is designed to operate in the Industrial Scientific Medical (ISM) 2.4 GHz band. As shown in Fig. 1, the antenna design which was previously reported by the authors of this paper [13] consists of a U-shaped monopole. This type of winding decreases the structure size without a disturbance to the radiation pattern or significant degradation of the efficiency (with respect to a free space monopole/dipole. The separation distance between the monopole arms is chosen as 6 mm which achieves the minimum return loss. It should be noted that smaller separation distance leads to an increased capacitive coupling between the arms which yields an increased impedance mismatch. The U-shaped monopole is fed by a 1.5 mm wide 50 Ω microstrip line. Both the monopole and the microstrip line are printed on the same side of a 26.5 mm x 25 mm Kapton polyimide substrate which offers a very low profile (50.8 μm) yet very robust with a very high tensile strength and a dielectric constant of 3.4 and a loss tangent of 0.002. On the other side of the substrate, a 12.5 mm x 25 mm copper ground plane is positioned behind the microstrip line. The electrical length of the U-shaped monopole in addition to the ground plane size controls the resonance frequency of the antenna. It is worth mentioning that the considered antenna was fabricated using a conductive ink based on sliver nano particles which is ink-jetted over the kapton polyimide substrate by a Fujifilm Dimatix DMP 2831 material printer followed by a thermal annealing at 100° C for 9 hours. Three layers of ink were deposited on the substrate to achieve a robust and continuous radiating element/feed line. The antenna's geometry and dimensions are depicted in Fig. 1 and Table 1, respectively.

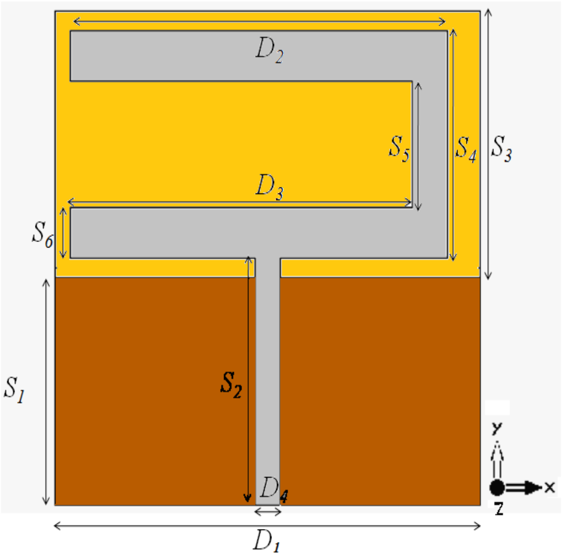

Fig. 1. Geometry and dimensions of the proposed printed monopole (the shaded area represents the ground plane on the opposite side).

Table 1: Single band antenna dimensions in millimeter

S_1	12.5	D_1	25
S_2	13.5	D_2	22
S_3	14	D_3	20
S_4	12	D_4	1.5
S_5	6		
S_6	3		

B. AMC based system

As is well known, utilizing AMC structures as ground planes significantly enhance the gain of dipole/monopole antennas [14, 15].

As stated previously, a PEC has a reflection phase of 180° for a normally incident plane wave, while a PMC, which does not exist in nature, has a reflection phase of 0°.

AMC which was first proposed by [15] can be artificially engineered to emulate a PMC, i.e.: have in-phase reflection coefficient properties in a specified frequency band. AMCs are typically realized based on periodic metallization patterns. The reflection phase of an AMC surface varies continuously from -180° to +180° versus frequency, and crosses zero at the AMC resonance frequency. The useful bandwidth of an AMC is generally defined as -90° to +90° on both sides of the resonant frequency [15].

In this research, a 3 x 3 unit cell of square patch based AMC (without vias) is designed to operate in the same frequency range as the antenna's (2.45 GHz) with a bandwidth of 200 MHz. The AMC is utilized to isolate the user's body from unnecessary radiation and to eliminate the antenna's impedance mismatch. The total size of the AMC is 58 mm x 58 mm printed on a substrate with 1.5 mm thickness and 4.5 mm dielectric constant. Figure 2 depicts the reflection phase profile of the proposed AMC structure.

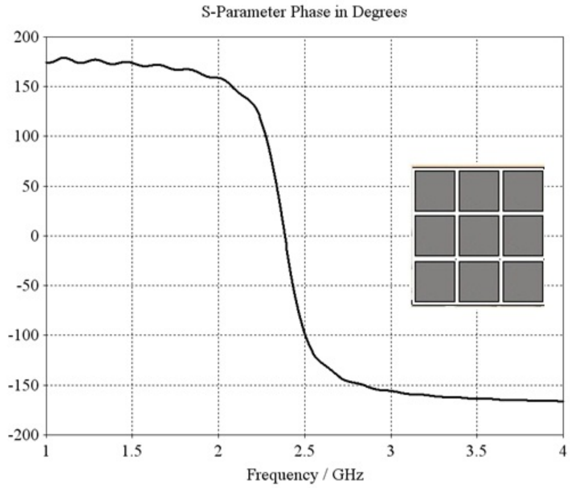

Fig. 2. Reflection phase profile of the AMC unit cell.

III. ANTENNA SYSTEM'S PERFORMANCE

The proposed antenna without AMC was first simulated in free space then over a HUGO numerical human model to study the effect of the human tissues proximity on the antenna's performance. HUGO is an anatomical 3D volume and surface data set of the human body which is based on the visible human data set produced by the National Library of Medicine. The HUGO data set is segmented and categorized into 40 different types of tissues and is available at a 1x1x1 mm voxel size [16]. The antenna is positioned on the arm of the human model as a typical realistic setup. To reduce the simulation time, a portion of the arm with a reasonable size (sectional area of about 25 times the antenna's size) is selected instead of simulating the entire numerical model; it should be noted that this approximation is fair since the specific absorption rate (SAR) distribution does not exceed this number (as will be observed later in Section IV). The number of mesh cells is reduced from 28,366,422 down to 1,423,934 mesh cells. It is worth mentioning that symmetry planes were applied to the AMC's unit cell structure to further reduce the simulation time required for reflection phase extraction since it has a geometrical symmetry. Electric wall (E_t=0) is applied in the YZ plane while a magnetic wall (H_t=0) is applied to the XZ plane in compliance with the assigned boundary conditions needed to simulate periodic AMC structures. Thus, 75% reduction in the mesh cells is achieved (from 128,000 down to 32,000) in addition to an extreme reduction in the simulation time. The overall simulation time is recorded to be 86 minutes on an Intel Xeon^{TM} 3.40 GHz CPU with a 16 Giga Byte RAM workstation. As is well known, if the number of the adopted mesh cells is not enough, enormous error may be induced which leads to accuracy deterioration of the entire simulation. Hence, to simultaneously retain the simulation efficiency and results accuracy, the number of mesh cells was mainly determined through sufficient meshing of the antenna element and AMC structure where the smallest geometric detail (i.e. AMC gap, antenna's microstrip line, etc,..) is covered by at least two mesh cells both horizontally and vertically. The numerical setup for the antenna-Hugo model is shown in Fig. 3.

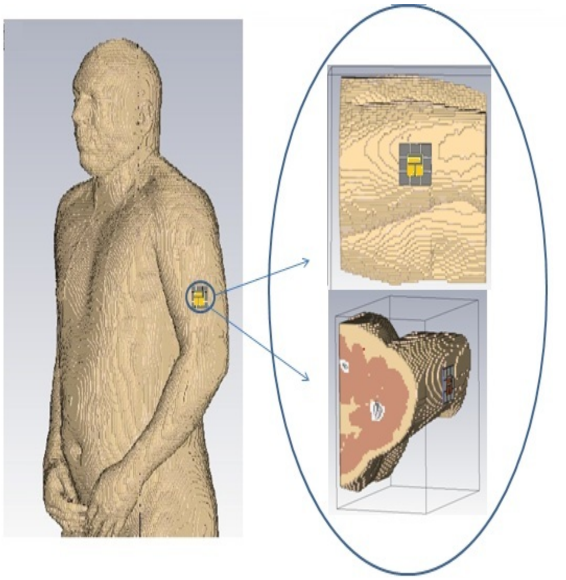

Fig. 3. Numerical human model (HUGO) used for realistic antenna performance testing.

To further validate the simulation results obtained from CST microwave studio, a simplified human arm model is synthesized based on a skin-fat-muscle scheme using the Ansoft HFSS full wave EM solver. The electrical properties of each material are imported from the HUGO model. The antenna is simulated on the human arm model with and without the AMC structure.

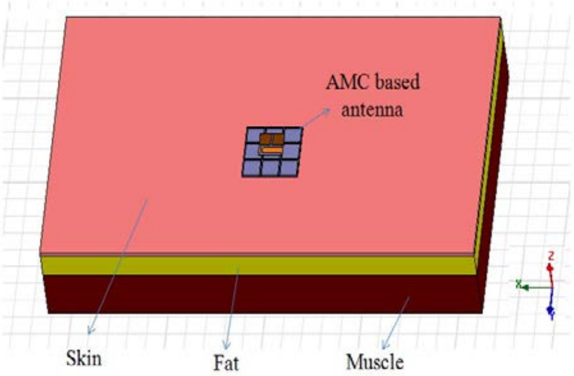

Fig. 4. Numerical human arm model in HFSS including the electrical properties of each layer.

As can be seen in Fig. 5, CST results for the return loss of the antenna with AMC on HUGO is -23 dB at 2.45 GHz, while the achieved -10 dB return loss bandwidth is 130 MHz. removing the AMC leads to a 95 MHz (4%) shift in the resonance frequency to the lower side, and an increase in the return loss (about 7 dB). HFSS results show good agreement with CST's. The antenna also experiences a shift to a lower frequency when the AMC is removed with an increase in return loss but to a less extent compared to CST results.

As stated earlier, integrating the AMC structure with the antenna (as a ground plane) overcomes the abovementioned problems associated with the human tissues proximity. Furthermore, the radiation pattern turns to a hemi-spherical when the AMC is included compared to an omni-directional radiation pattern for the conventional monopole.

It is evident from Fig. 6 that a considerable improvement in terms of gain is achieved (4.1 dB) by including the AMC structure with respect to a free-space monopole. The simulated gain for the proposed antenna system is 6.2 dB compared to 2.1 dB for the original case. It should be noted that using a PEC ground plane instead of AMC would lead to a high profile system since a separation of λ/4 is required to achieve in phase reflection. The separation distance could be reduced if the monopole is placed on top of a high permittivity dielectric slab backed by a PEC; the drawback of using this technique is that high permittivity substrates support surface waves which trap a significant amount of power radiated by the monopole and become the main radiation source, which consequently leads to a distortion in the radiation pattern.

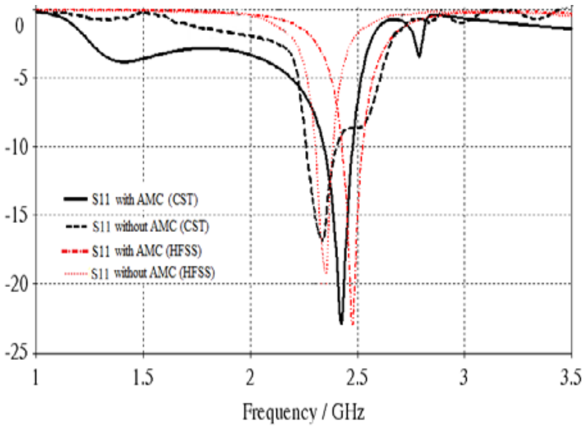

Fig. 5. S_{11} parameters for the antenna on a human numerical model (with and without AMC).

IV. SAR ANALYSIS

The specific absorption rate (SAR) is a standard measure used to evaluate electromagnetic power deposition in the human tissues. SAR values must not exceed the exposure guidelines specified by the Federal Communication Commission (FCC). The maximum allowed SAR in USA and Canada is 1.6 W/kg averaged over 1g of tissue [17]. SAR was simulated using the HUGO human model to reflect realistic situations. For comparison purposes, both the proposed design and the antenna without AMC were simulated. As is well known, the radiated power of mobile phones can range from 21dBm (125 mW) to 33 dBm (2W) depending on the adopted power class; on the other hand, a wireless router can range from a typical 15 dBm (30 mW) to 27 dBm (500 mW). Since FCC has not standardized the power limit in telemedicine systems yet, a 100 mW power input is chosen as benchmark to evaluate the performance of the antenna systems (with and without AMC) in terms of SAR values. For the considered power input, the proposed design achieved a SAR value of 0.68 W/Kg while the same antenna without AMC experiences a 1.68 W/Kg which is above the specified rate allowed by the FCC. Thus, the proposed design achieved a 60% reduction in SAR. SAR values for both cases are depicted in Fig. 7.

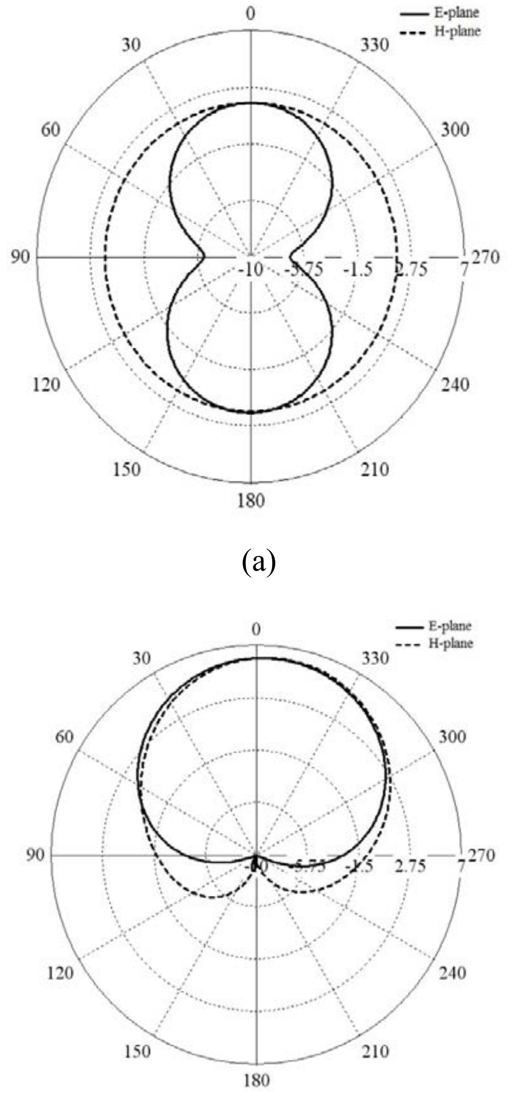

(a)

(b)

Fig. 6. E-plane (YZ cut) and H-plane (XZ cut) radiation patterns for (a) printed monopole antenna and (b) the same antenna based on AMC ground plane.

V. CONCLUSION

In this paper, we reported a printed monopole antenna design based on an AMC ground plane intended for telemedicine applications. The AMC ground plane is utilized to eliminate the impedance mismatching and frequency shift caused by the human tissues proximity. Furthermore, the in-phase reflection characteristic of the AMC structure significantly reduced the undesired electromagnetic radiation towards the patient's body which is essential to the performance of telemedicine antenna systems. The proposed antenna has an operating bandwidth of 5.4% at 2.45 GHz with a unidirectional radiation pattern. The calculated SAR values for the AMC based antenna were very low with a reduction of about 60% compared to the same antenna without the integration of AMC. To conclude, the proposed antenna would be a good candidate for wireless body area network (WBAN) and telemedicine applications in terms of SAR, efficiency, bandwidth, and stability.

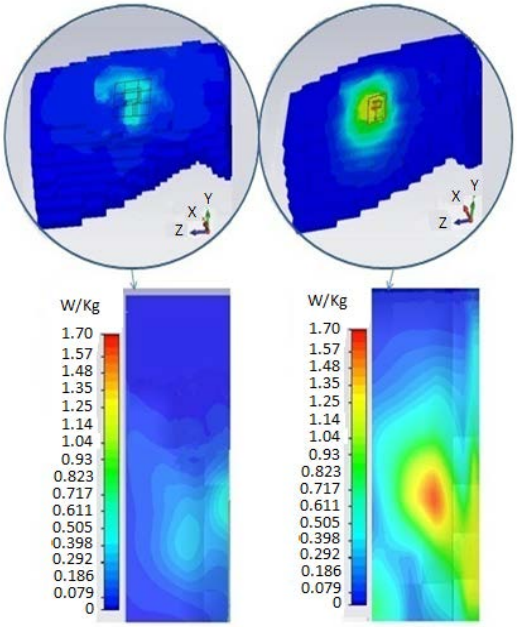

Fig. 7. SAR values for the proposed design (left) and for the same design without the AMC structure (right).

REFERENCES

[1] S. Pavlopoulos, E. Kyriacou, A. Berler, S. Dembeyiotis, and D. Koutsouris, "A Novel Emergency Telemedicine System Based on Wireless Communication Technology AMBULANCE," *IEEE Trans. on Information Technology in Biomedicine*, 2, 4, pp. 261-267, 1998.

[2] G. A. Conway and W. G. Scanlon, "Antennas for over body-surface communication at 2.45 GHz," IEEE Trans. on antennas and propag., vol. 57, no. 4, pp. 844-855, Apr. 2009.

[3] Y. Ouyang, D. Love, and W. Chapell, "Body Worn Distributed MIMO System," IEEE Trans. on vehicular Tech., vol. 58, no. 4, May. 2009.

[4] P. Salonen, J. Kim, and Y. Rahmat-Samii, "Dual-Band E-Shaped Patch Wearable Textile Antenna," IEEE Antennas and Propagation Society Symposium, vol. 1, pp. 466-469, 2004.

[5] L. Liu, S. Zhu, and R. Langley, "Dual-Band Triangular Patch Antenna with Modified Ground Plane," Electronic letters, vol. 43, no. 3, Feb. 2007.

[6] B. Sanz-Izquierdo and J. C. Batchelor, "WLAN Jacket Mounted Antenna," Antenna Technology, pp. 57-60, Jun. 2007.

[7] H. N. Saito, K. Takahashi, M. Ito, K., "Characteristics of Cavity Slot Antenna for Body-Area Networks," IEEE Trans. on Antennas and Propag., vol. 57, no. 4, pp. 837-843, 2009.

[8] W. Rowe and R. B.Waterhouse, "Reduction of Backward Radiation for CPW Fed Aperture Stacked Patch Antennas on Small Ground Planes," *IEEE Trans. Antennas Propag*., vol. 51, no. 6, Jun. 2003.

[9] S. D. Targonski and D. M. Pozar, "Aperture-Coupled Microstrip Antennas using Reflector Elements for Wireless Communications," in Proc. IEEE-APS Antennas and Propagation for Wireless Communications, Nov. 1998, pp. 163–166.

[10] M. T. Islam, M. R. I. Faruque, and N. Misran, "Reduction of Specific Absorption Rate (SAR) in the Human Head with Ferrite Material and Metamaterial," Progress In Electromagnetics Research C, vol. 9, 4758, 2009.

[11] CST Microwave Studio, www.CST.com

[12] Ansoft's HFSS, www.ansoft.com

[13] H. R. Khaleel, H. M. Al Rizzo, D. G. Rucker, and Y. Al-Naiemy, "Flexible Printed Monopole Antennas for WLAN Applications," IEEE APS-URSI international symposium on antennas and propagation, Spokane, WA, July 2011.

[14] F. Yang, V. Demir, D. A. Elsherbeni, A. Z. Elsherbeni, and A. A. Eldek, "Enhancement of Printed Dipole Antennas Characteristics using Semi-EBG Ground Plane," Journal of Electromagnetic Waves and Applications (JEMWA), vol. 20, no. 8, pp. 993-1006, 2006.

[15] D. Sievenpiper, L. J. Zhang, R. F. J. Broas, N. G. Alexopolous, and E. Yablonovitch, "High-Impedance Electromagnetic Surfaces with a Forbidden Frequency Band," IEEE Trans. Microw. Theory Tech, vol. 47, pp. 2059–2074, Nov. 1999.

[16] http://www.vr-laboratory.com

[17] www.fcc.gov/cgb/sar

[18] M. R. I. Faruque, M. T. Islam, and N. Misran, “Evaluation of EM Absorption in Human Head with Metamaterial Attachment,” The Applied Computational Electromagnetics Society (ACES) Journal, vol. 25, Dec. 2010.

[19] W. Huang and A. A. Kishk, “Compact Antenna Designs for Wearable and Portable Medical System,” The Applied Computational Electromagnetics Society (ACES) Journal,” vol. 26, no. 4, pp. 295–302, Apr. 2011.

[20] M. Fallah, A. A. Heydari, F. H. Kashani, and A. R. Mallahzadeh, “Design and SAR Reduction of the Vest Antenna using Metamaterial for Broadband Applications,” The Applied Computational Electromagnetics Society (ACES) Journal,” vol. 26, no. 2, pp. 141-152, February 2011.

[21] C. Furse, “A Survey of Phased Arrays for Medical Applications,” The Applied Computational Electromagnetics Society (ACES) Journal,” vol. 21, no. 3, pp. 365-379, Nov. 2006.

[22] P. Kildal and A. Kishk, “EM Modeling of Surfaces with Stop or Go Characteristics – Artificial Magnetic Conductors and Soft and Hard Surfaces,” The Applied Computational Electromagnetics Society (ACES) Journal,” vol. 18, no. 1, pp. 32-40, March 2003.

[23] Institute of Electrical and Electronics Engineers, IEEE Standard for Information technology Telecommunications and information exchange between systems, Local and metropolitan area networks. Part 2 Wireless LAN Medium Access Control (MAC) and Physical Layer (PHY) specifications.

[24] A. Alomainy, Y. Hao, X. Hu, C. G. Parini, and P. S. Hall, “UWB On-Body Radio Propagation and System Modelling for Wireless Body-Centric Networks,” Proc. Inst. Elect. Eng. Communications-Special Issue on Ultra Wideband Systems, Technologies and Applications, vol. 153, no. 1, Feb. 2006.

[25] Y. Hao, A. Alomainy, P. S. Hall, Y. I. Nechayev, C. G. Parini, and C. C. Constantinou, “Antennas and Propagation for Body Centric Wireless Communications,” IEEE/ACES Int. Conference on Wireless Communications and Applied Computational Electromagnetics, Honolulu, HI, Apr. 3-7, 2005.

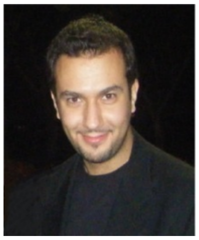

Haider R. Khaleel received the B.Sc. degree in Control and Systems Engineering from the University of Technology Baghdad-Iraq, and the M.Sc. degree in Electrical and Computer Engineering from New York Institute of Technology (highest honors) in 2003 and 2006, respectively. He is currently working towards a Ph.D. degree in the Systems Engineering department at the University of Arkansas at Little Rock. He has been a Graduate Research and Teaching Assistant in the Applied Science Department at the University of Arkansas at Little Rock since August 2008. His main research interests include Metamaterial based antennas, wearable and implantable antennas, development of flexible electromagnetic materials, and antennas for MIMO systems.

Hussain M. Al-Rizzo received his B.Sc. in Electronics and Communications (1979) (High Honors), Postgraduate Diploma in Electronics and Communications (1981) (High Honors) and M.SC. in Micowave Communication Systems (1983)from the University of Mosul, Mosul, Iraq. From May 1983 to October 1987, he was working with the Electromagnetic Wave Propagation Department, Space and Astronomy Research Center, Scientific Research Council, Baghdad, Iraq. In December 1987, he joined the Radiating Systems Research Laboratory, Electrical and Computer Engineering Department, University of New Brunswick, Fredericton, NB, Canada where he obtained his Ph.D. (1992) in Computational Electromagnetics, Wireless Communications, and the Global Positioning System. For his various academic achievements he won the nomination by the University of New Brunswick as the best doctoral graduate in science and engineering. Since 2000, he joined the Systems Engineering Department, University Arkansas at Little Rock where he is currently a Professor of Systems Engineering. He has published over 40 peer-reviewed journal papers, 70 conference presentations, and several patents. His research areas include implantable antennas and wireless systems, smart antennas, WLAN deployment and load balancing, electromagnetic wave scattering by complex objects, design, modeling and testing of high-power microwave applicators, design and analysis of microstrip antennas for mobile radio systems, precipitation effects on terrestrial and satellite frequency re-use communication systems, and field operation of NAVSTAR GPS receivers.

Daniel G. Rucker received his Bachelors of Science in Systems Engineering from the University of Arkansas at Little Rock in Spring 2007. He was accepted by the National Science Foundation (NSF) for a Research Experience for Undergraduates program in the summer of 2006 at the Arecibo Observatory in Puerto Rico. There he worked on digital electronics and radar control. Following this work, he shifted his undergraduate research to microstrip antennas for biomedical devices at UALR. Currently, he is pursuing a Ph.D. in Applied Science at the University of Arkansas at Little Rock. His current research areas are microstrip antennas, low power wireless sensor systems, and systems engineering design. In the area of microstrip antennas, his work is focused on implantable and wearable microstrip antennas for biomedical applications.

A Novel Integrated Corrugated Waveguide Bandpass Filter

Hassan Aghayari [1], Nader Komjani [2], and Nima Molaei Garmjani [2]

[1] Department of communication Engineering
Saeb University, Abhar, Iran
hassanaghayari@gmail.com

[2] Department of Electrical Engineering
Iran University of Science & Technology (IUST), Tehran, IRAN
n_komjni@iust.ac.ir, n.molaei@ieee.org

Abstract **─** This paper presents the approach for the design of a X-band bandpass filter using substrate integrated corrugated waveguide (SICW). The SICW filter which is proposed in this paper, is totally realized in a single-layer dielectric substrate with two sequences of metallic vias with the different diameters, and fabricated using a standard PCB process. This proposed filter has the same dispersion characteristics as a waveguide filter, while its dimensions are very shorter than it. A transition circuit between the SICW and 50 Ω microstrip lines was designed for excitation of the filter.

Index Terms **─** Microstrip bandpass filter, substrate integrated corrugated waveguide (SICW).

I. INTRODUCTION

The waveguide filter is one of the key sections of communication systems with noticeable features such as low insertion loss, high quality factor, and more power transition capability. However, the waveguide equipment has few disadvantages such as expensive fabricating process, difficulty to be integrated in planar circuits because of their large size and non-planar structure. The corrugated H-Plane waveguide filter [1] is the conventional type of these filters which are fabricated using with corrugated sections as direct coupled half wave resonators.

Recently, a novel planar structure technique, called substrate integrate waveguide (SIW) is introduced. This technique has many advantages of printed circuits such as small size, low cost, and easily integration with the microwave and millimeter wave integrated circuits. Many passive and active components based on SIW technique such as mixer [2], coupler [3], phase shifter [4], six ports [5], a circulator [6], diplexer [7], and antennas [8, 9] have been reported recently.

In this paper, a novel design based on the substrate integrated corrugated waveguide (SICW) is represented for realization of waveguide bandpass filter in substrate. SICW consist of two rows of metallic vias, each one operate as one of side walls of waveguide. The other strings of metallic vias with different diameters which are perpendicular to previous ones, act as resonators of waveguide. All results in this paper are obtained using a Ansoft HFSS simulator. A simulated result for the frequency response of conventional corrugated H-Plane waveguide filter and proposed SICW H-Plane filter are in a good agreement as show in this paper.

II. CORRUGATED H-PLANE WAVEGUIDE FILTER

The corrugated H-Plane waveguide filter [1] is one type of these filters which are fabricated using corrugated sections in its H-Plane as direct coupled half wave resonators. This method is based on distributed step impedance bandpass filters that are formulated in [10]. Chebyshev response is considered in this method. Lumped element prototype of bandpass filter and its

Submitted On: July 9, 2011
Accepted On: Dec 18, 2011

equivalent distributed prototype is shown in Fig. 1. (a), (b).

This approach consists of a cascading of impedance inverters connected by transmission lines. Fig. 1(b) shows the impedance inverters K_{ij} and parallel-resonant circuits of bandpass filter are demonstrated in Fig. 1(a), which are made of the above mentioned inverters.

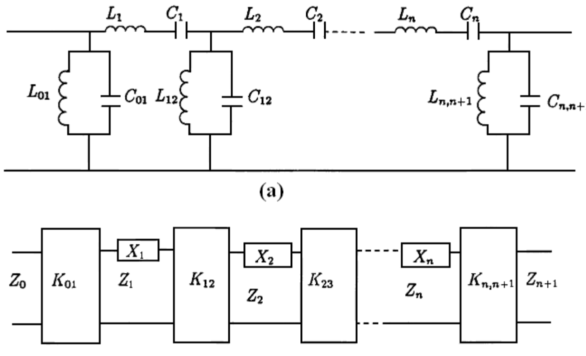

(a)

(b)

Fig. 1. Equivalent models of the corrugated waveguide filter, (a) parallel-resonant circuits, (b) impedance inverters [1].

The six steps of the procedure of designing corrugated H-plane waveguide bandpass filters are as follows [10]:

1. The guide wavelength of midband λ_{g0} is calculated from this equation:

$$\lambda_{gL} \sin\left(\frac{\pi\lambda_{g_0}}{\lambda_{gL}}\right) + \lambda_{gH} \sin\left(\frac{\pi\lambda_{g_0}}{\lambda_{gH}}\right) = 0, \qquad (1)$$

where λ_{gL} and λ_{gH} are the guide wavelengths for cut off frequencies of the lower f_L and upper f_H, respectively. In case of a narrow-band, we have:

$$\lambda_{g_0} = \frac{\lambda_{gL} + \lambda_{gH}}{2}. \qquad (2)$$

2. Scaling parameter α is determined from:

$$\alpha = \frac{\lambda_{g_0}}{\lambda_{gL} \sin\left(\frac{\pi\lambda_{g_0}}{\lambda_{gL}}\right)}. \qquad (3)$$

3. The impedance inverter values K_{ij} and the impedance of the distributed element Z are obtained from:

$$Z_n = \frac{2\alpha \sin\left[\frac{(2n-1)\pi}{2N}\right]}{y} - \frac{1}{4y\alpha}\left\{\frac{y^2 + \sin^2\left(\frac{n\pi}{N}\right)}{\sin\frac{(2n+1)\pi}{2N}}\right\} - \frac{1}{4\alpha}\left\{\frac{y^2 + \sin^2\left[\frac{(n-1)\pi}{N}\right]}{\sin\frac{(2n-3)\pi}{2N}}\right\}, \quad n = 1,2,\ldots,N, \qquad (4)$$

and

$$K_{n,n+1} = \frac{\sqrt{y^2 + \sin^2\left(\frac{n\pi}{N}\right)}}{y}, \quad n = 0,\ldots,N, \qquad (5)$$

where

$$y = \sinh\left[\frac{1}{N}\sinh^{-1}\frac{1}{\varepsilon}\right], \qquad (6)$$

and N is the number of resonators.

4. The characteristic impedances of the resonators are the same and by scaling the impedance Z_n to oneness, the K-inverters are normalized by:

$$K_{n,n+1} = \frac{k_{n,n+1}}{\sqrt{Z_n Z_{n+1}}}, \quad n = 0,\ldots,N, \qquad (7)$$

and

$$Z_0 = Z_{n+1} = 1. \qquad (8)$$

5. The asymmetrical impedance inverter is used for presentation of filter structure. The values of the impedance inverters shown in Fig. 2 are realized from following [10]:

$$\begin{aligned} &\mathrm{K} = \sqrt{\mathrm{Z_1 Z_2}\left(\sqrt{\mathrm{L}} - \sqrt{\mathrm{L}-1}\right)} \\ &\mathrm{L} = 1 + \frac{1}{4}\left\{(\mathrm{a}-\mathrm{d})^2 + (\mathrm{b}-\mathrm{c})^2\right\} \\ &\mathrm{a} = \mathrm{A}\sqrt{\frac{\mathrm{Z_2}}{\mathrm{Z_1}}}, \ \mathrm{b} = \frac{\mathrm{B}}{\sqrt{\mathrm{Z_1 Z_2}}} \\ &\mathrm{c} = \mathrm{C}\sqrt{\mathrm{Z_1 Z_2}}, \ \mathrm{d} = \mathrm{D}\sqrt{\frac{\mathrm{Z_1}}{\mathrm{Z_2}}}. \end{aligned} \qquad (9)$$

In this equation, a, b, c, and d are normalized elements of the ABCD matrix, and Z_1 and Z_2 are normalized guide impedances of the tapered waveguide resonator sections.

The electrical length is calculated by:

$$\begin{cases} \tan 2\phi_1 = \dfrac{2(bd - ac)}{(a^2 - d^2) + (b^2 - c^2)} \\ \tan 2\phi_2 = \dfrac{2(ab - cd)}{(d^2 - a^2) + (b^2 - c^2)} \end{cases}, \qquad (10)$$

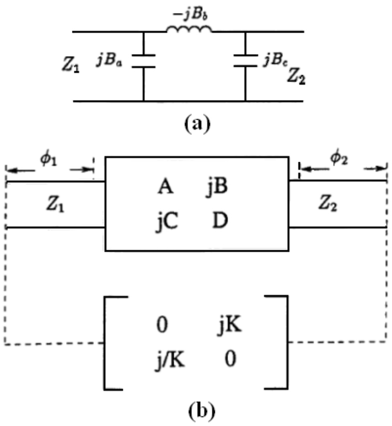

Fig. 2. (a) Equivalent circuit of an asymmetrical iris, (b) equivalent impedance inverter [1].

where the angles φ_1 and φ_2 are expressed in radians.

6. Finally, the physical length of the resonator is obtained from following:

$$l_i = \frac{\lambda_{g_0}}{2\pi}\left[\pi + \frac{(\phi_1 + \phi_{i+1})}{2}\right] . \tag{11}$$

The mentioned method is used to design a corrugated H-plane waveguide filter with the bandpass extending from 10.31 to 10.33 GHz and a 12.4 dB return loss. The width and height of the standard X-band waveguide are 22.86 mm and 10.16 mm, respectively. The thickness of the waveguide is considered as 2 mm. Its side and top view are shown in Fig. 3.

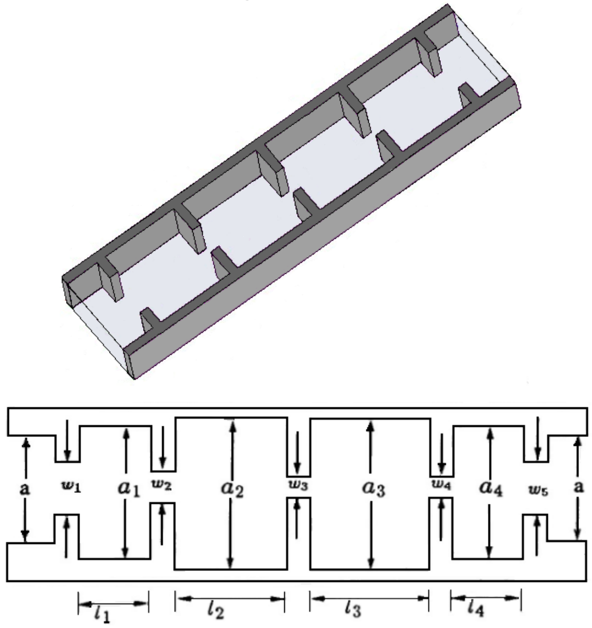

Fig. 3. Side and top view of corrugated standard waveguide filter.

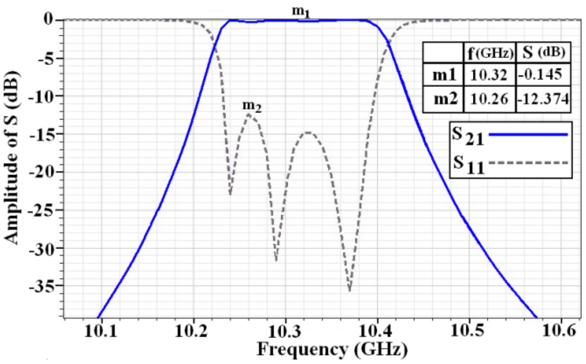

Fig. 4. Simulation result of corrugated standard waveguide filter.

Demonstrated dimension in Fig. 3 are shown in Table 1 where all dimensions shown in millimeters.

Table 1: The parameters of Fig. 3

Parameter	Value	Parameter	Value
$l_1=l_4$	16.283	$w_2=w_4$	6.206
$l_2=l_3$	17.715	w_3	5.79
$w_1=w_5$	10.055	$a_1=a_2=a_3=a_4$	22.86

Simulation results of the designed filter are shown in Fig. 4 which is obtained by Ansoft HFSS.

III. SUBSTRATE INTEGRATED WAVEGUIDE

Substrate integrated waveguide is a new type of planar structure which is based on a low-cost printed circuit board (PCB) process similar to microstrip, stripline, or coplanar waveguides. The SIW is implemented on a substrate using arrays of metallic vias which take the roll of the side walls of waveguide. The transmission to planar structures such as microstrip, stripline, or coplanar waveguide is designed and integrated on the same substrate. SIW components can be integrated together without any transmission circuit. The performance of the SIW component, such as insertion loss, quality factor, and power transmission, is better than the performance of microstrip, stripline, or coplanar waveguide.

However, the analysis of via structure of the SIW component is much more complicated than the conventional waveguide devices. Characteristics of the SIW component can be achieved using a generalized BI-RME method [12].

It was assumed that a TE_{10}-like mode in the SIW has similar dispersion characteristics to TE_{10} mode of a dielectric filled rectangular waveguide with an equivalent width. This equivalent width is known as effective width of the SIW (see Fig. 5). Other the important parameters of SIW are the diameter of vias (D) and the distance between them (b).

The SIW parameters of Fig. 5 can be approximated as follows [13, 14]:

$$\left[W = a_{rwg} + \frac{D^2}{0.95b} \right] . \qquad (12)$$

The practical conditions which shall be considered are as follow:

$(b - D) \leq 0.2\lambda$ and $(b - D)/D \leq 0.5$.

If (b-D) is greater than 0.2λ, the power leakage between adjacent vias will increase. If the diameter of via holes (D) is over the range, the reflection loss of the SIW filter will be great.

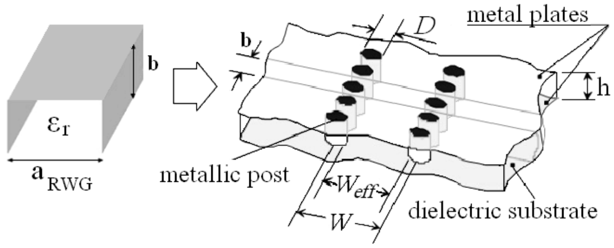

Fig. 5. Filled waveguide to substrate mapping and SIW parameters [8].

Since the field distribution in SIW component is similar to the conventional rectangular waveguide, it is possible to use the same equation to calculate the cut-off frequency of the SIW:

$$f_c^{mn} = \frac{1}{2\pi\sqrt{\mu\varepsilon}} \cdot \sqrt{\left(\frac{m\pi}{a}\right)^2 + \left(\frac{n\pi}{b}\right)^2} . \qquad (13)$$

Equation (5) can be writing as follows:

$$f_c^{10} = \frac{1}{2\pi a} \cdot \frac{1}{\sqrt{\mu_0 \varepsilon_0}} \cdot \frac{1}{\sqrt{\varepsilon_r}} . \qquad (14)$$

IV. SUBSTRATE INTEGRATED CORRUGATED WAVEGUIDE FILTER

Figure 6 shows the arrangement of a substrate integrated corrugated waveguide (SICW). The SICW filter is designed based on the "Taconin TLY(tm)" subtracted with following characteristics:

$$h = 0.81mm,\ \varepsilon_r = 2.2,\ \tan\delta = 0.0009$$

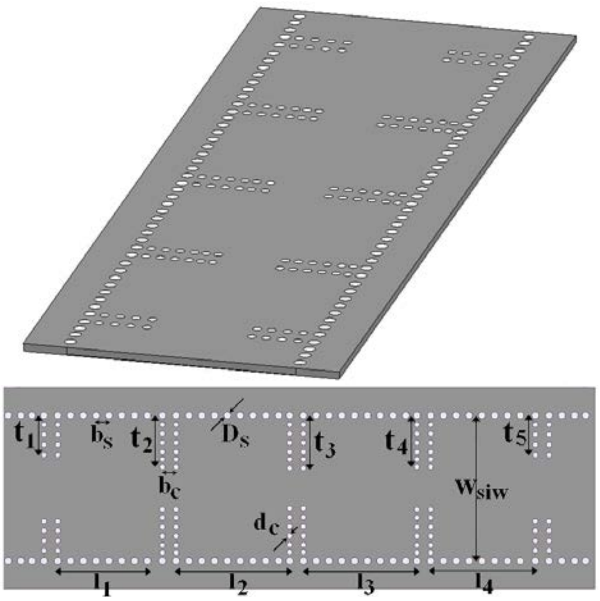

Fig. 6. Side and top view of substrate integrated corrugated waveguide filter.

Table 2: The parameters of the SICW filter

Parameter	Value	Parameter	Value
t_1	4.33	l_1	12.94
t_2	5.63	l_2	13.91
t_3	5.77	l_3	13.91
t_4	5.63	l_4	12.94
t_5	4.33	Wsiw	15.93
D_s	0.8	bs	1.5
d_c	0.6	bc	1.5

The diameter of the side vias (D_S) and the corrugated section vias (d_S) is chosen 0.8 mm and 0.6 mm, respectively. Other parameters of Fig. 6 are shown in Table 2 where all dimensions shown in millimeters. According to the Table 1, it is recognized that width, height, and length of the filter are reduced noticeably.

V. EXCITATION MECHANISM OF SICW

Different structure maybe proposed for the excitation of the SIW structures. A conventional type is made of a tapered microstrip line between the SIW section and 50 Ω microstrip lines. This plane is shown in Fig. 7.

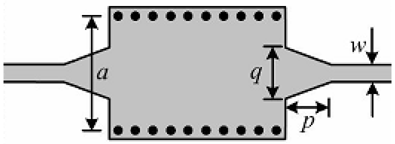

Fig. 7. Transmission SIW to microstrip lines.

The width of SICW (q) is achieved from input impedance, and the width of excitation port (w) is calculated based on the 50 Ω microstrip lines [15]. The length of transmission line (p) is optimized by the Ansoft HFSS. The above mentioned parameters are as follows:

$$q = 13.6\,mm,\ w = 2.25\,mm,\ p = 13.5\,mm$$

Top views of the proposed SICW filter are illustrated in Fig. 8.

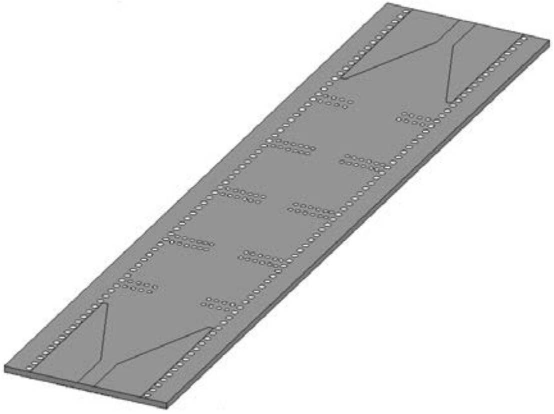

Fig. 8. Top view of SICW filter with transmission to microstrip line.

The designed SICW filter is simulated by Ansoft HFSS in bandwidth of 10.15-10.45 GHz and the results are shown in Fig. 9.

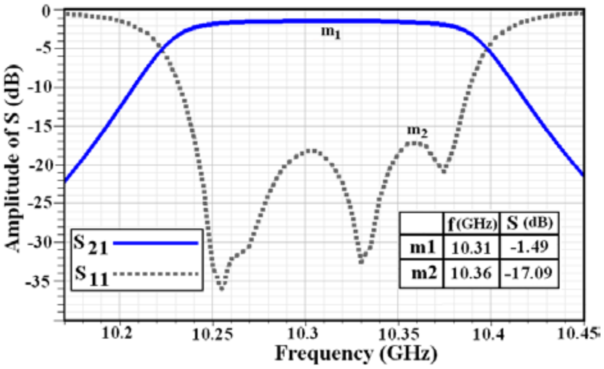

Fig. 9. Simulation result of designed SICW filter.

According to Fig. 9, return and insertion loss are better than 17.1dB and 1.49 dB, respectively.

VI. EXPRIMENTAL RESULT

The proposed filter is fabricated and the Fig. 10 shows this prototype.

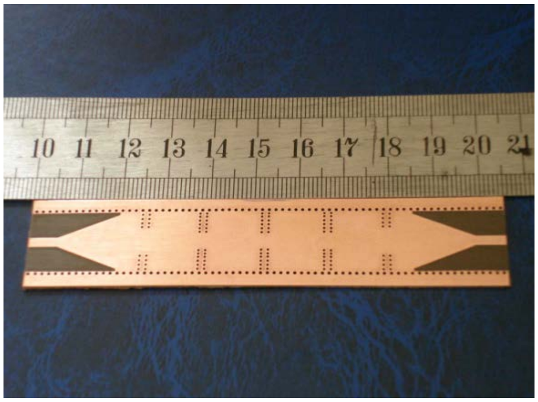

Fig. 10. Fabricated SICW filter.

The scattering parameters of the fabricated filter are measured by Agilent 8720-B Vector Network Analyzer (VNA) and the results are shown in Fig. 11.

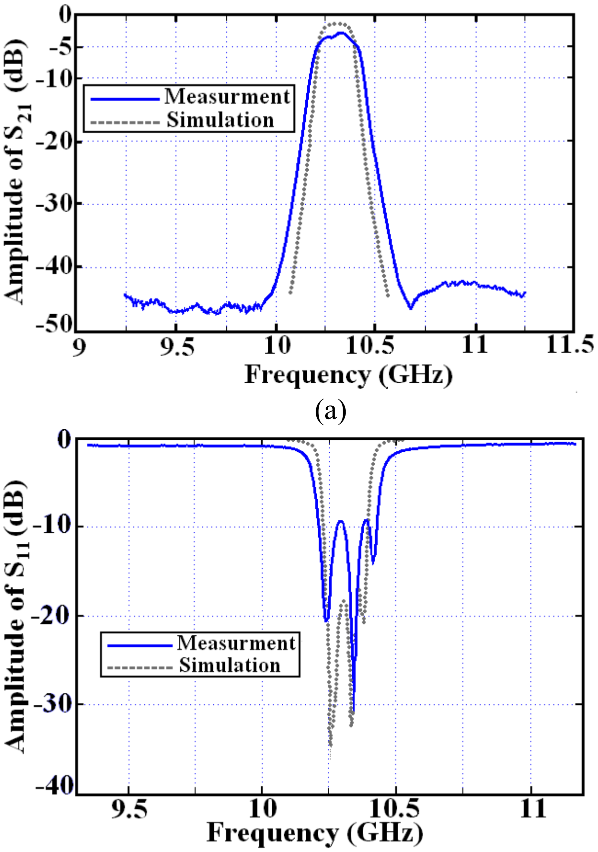

(a)

(b)

Fig. 11. Measurement and simulation result of SICW filter, (a) insertion loss, (b) return loss.

As it is observed in Fig. 11(a), insertion loss of the fabricated model is 2.4 dB at the center frequency, which is about 1 dB higher than the simulation results. In addition, return loss of the fabricated model is 17 dB, which is close to simulation results, as seen in Fig. 11(b). By comparing Fig. 11(a) and (b), we observe a good accordance between them.

VII. CONCLUSION

A novel single-layer planar X-band SICW filters is presented in this paper. The prototype of this filter is designed, simulated, and fabricated using a PCB process and measured with a VNA. This proposed SICW filter is totally developed by metallic vias with different diameters on a single-layer substrate, and has the same dispersion characteristics as a waveguide filter, while its dimensions are very smaller than it. The width and height of standard waveguide is 22.86 mm and 10.16 mm while the width and height of SCIW is 22 mm and 0.81 mm, respectively; this shows a reduction ratio of about 12.5 in the height of the filter. This approach has some advantages such as compact size, low weight, and low cost. So, it is a suitable choice for designing microwave and millimeter-wave planar circuits.

REFERENCES

[1] R. Balasubramanian and P. Pramanick, “Computer Aided Design of H_Plane Tapered Corrugated Waveguide Bandpass Filter,” *Department of Electrical Engineering*, 57 Campus Drive, University of Saskatchewan, Canada S7N 5A9, April 1998.

[2] J. X. Chen, Z. C. Hao, H. Li, K.-Wu, "Development of a Low Cost Microwave Mixer using a Broad-band Substrate Integrated Waveguide (SIW) Coupler," *IEEE Microwave and Wireless Comm.*, vol. 16, no. 2, February 2006.

[3] Z. C. Hao, W. Hong, J. X. Chen, H. X. Zhou, and K.-Wu, "Single-Layer Substrate Integrated Waveguide Directional Couplers," *IEEE Proc-Microw-Antenna Propagation*, vol. 153, no. 5, October 2006.

[4] K. Sellal, L. Talbi, T. Denindni, and J. Leble, "A New Substrate Integrated Waveguide Phase Shifter," *Proceeding of the 36th European Microwave Conference*, Manchester UK, September 2006.

[5] X. Xu, R. G. Bosisio, and K.-Wu, "A New Six-Port Junction Based on Substrate Integrated Waveguide Technology," *IEEE Trans. On Microwave Theory and Tech.*, vol. 53, no. 7, July 2005.

[6] D. William, Orazio, and K.-Wu, "Substrate Integrated Waveguide Circulators Suitable for Millimeter-Wave Integration," *IEEE Trans. On Microw. Theory and Tech.*, vol. 54, no. 10, October 2006.

[7] H. J. Tang, W. Hong, J. X. Chen, G. Q. Luo, and K.-Wu, "Development of Millimeter-Wave Planar Diplexers Based on Complementary Characters of Dual-Mode Substrate Integrated Waveguide Filters With Circular and Elliptic Cavities," *IEEE Trans. On Microw. Theory and Tech.*, vol. 55, no. 4, April 2007.

[8] L. Yang, W. Hong, G. Hao, J. Chen, K.-Wu, T. J. Cui, "Simulation and Experiment on SIW Slot Array Antenna," *IEEE Microw. And Wireless Comm.*, vol. 14, no. 9, September 2004.

[9] G. Q. Luo, W. Hong, H. J. Tang, J. X. Chen , X. X. Yin, Z. Q. Kuai, and K.-Wu, "Filtenna Consisting of Horn Antenna and Substrate Integrated Waveguide Cavity FSS," *IEEE Trans. On Antennas and Propagation*, vol. 55, no. 1, January 2007.

[10] L. Q. Bui, D. Ball, and T. Itoh, “Broad-Band Millimeter-Wave E-Plane Bandpass Filters,” *IEEE Transactions on Microwave Theory and Techniques*, MTT321984, 16551658.

[11] G. Matthaei, L. Yong, and E. M. T. Jones, *Microwave Filters, Impedance Matching Network, and Coupling Structures*. Boston, MA, Artech House, 1980.

[12] G. Conciauro, M. Guglielmi, and R. Sorrentino, *Advance Modal Analysis: CAD Techniques for Waveguide Components and Filters*. NewYork, Wiley, 2000.

[13] H. LI, W. Hong, T. J. Cui, and K. Wu, "Propagation Characteristics of Substrate Integrated Waveguide based on LTCC", *IEEE MTT-S Tech. Dig.*, vol. 3, Jun. 2003.

[14] Y. Cassivi, L. Perregrini, P. Arcioni, M. Bressan, K. Wu, and G. Conciauro, "Dispersion Characteristics of Substrate Integrated Rectangular Waveguide," *IEEE Microw. Wireless Compo. Lett.*, vol. 12, no. 9, pp. 333-335, Sep. 2002.

[15] N. M. Garmjani and N. Komjani, “Improved Microstrip Folded Tri-Section Stepped Impedance Resonator Bandpass Filter using Defected Ground Structure,” *Applied Computational Electromagnetic Society (ACES) Journal*, vol. 25, no. 11, pp. 975 – 983, November 2010.

[16] E. Mehrshahi and M. Salehi, “A Simple Technique for Propagation Characteristics of Substrate Integrated Waveguide,” *Applied Computational Electromagnetic Society (ACES) Journal*, vol. 25, no. 8, pp. 690–695, August 2010.

[17] F. Giuppi, A. Georgiadis, M. Bozzi, S. Via, A. Collado, and L. Perregrini, "Hybrid Electromagnetic and Non-Linear Modeling and Design of SIW Cavity-Backed Active Antennas," *Applied Computational Electromagnetic (ACES) Journal*, vol. 25, no. 8, pp. 682 – 689, August 2010.

[18] L. Sh. Wu, X. L. Zhou, W. Y. Yin, Ch. T. Liu, L. Zhou, J. F. Mao, and H. L. Peng, "A New Type of Periodically Loaded Half-Mode Substrate Integrated Waveguide and Its Applications," *IEEE Transactions on Microwave Theory and Techniques*, vol. 58, iss. 4, pp. 882-893.

[19] H. Kong and Macau "Substrate Integrated Waveguide with Corrugated Wall," *Asia Pacific Microwave Conference 2008* (China APMC 2008), 16-19 Dec 2008.

Hassan Aghayari was born in Abhar, Iran, in 1984. He received the B.S. degree in Electrical Engineering from the University of Gilan, Iran, in 2006, the M.S. degree in Communication Engineering from Iran University of Science and Technology, Tehran, Iran, in 2009. His current research interests are substrate integrated waveguide (SIW). Currently, he is the director of the Department of communication Engineering, Saeb university, Abhar, Iran.

Nader Komjani was born in Tehran, Iran, in 1965. He received the B.S., M.S. and Ph.D. degrees in Communication Engineering from Iran University of Science and Technology in 1988, 1991 and 2000, respectively. From 1991 to 1994, he joined the Iranian Science Organization of Science and Technology. His current research interests are in Phased Array Antennas, UWB and multi-band microstrip antenna, and numerical methods in electromagnetic. Currently, he is assistant professor and the Director of the Antenna Lab. in the Electrical Engineering Department, Iran University of Science and Technology.

Nima Molaei Garmjani was born in Tehran, Iran, in 1982. He received the B.S. degree in Electrical Engineering from Azad University, Iran, in 2006, the M.S. degree in Communication Engineering from Iran University of Science and Technology, Tehran, Iran, in 2009. His research interests include the design and analysis of microwave filter circuits and microstrip stepped impedance resonators (SIR).

A Novel SWB Small Rhombic Microstrip Antenna with Parasitic Rectangle into Slot of the Feed Line

M. Mighani [1], M. Akbari [2], and N. Felegari [3]

[1] Faculty of Engineering, Department of Electrical Engineering
Aeronautical University, Tehran, Iran
Mojtaba.mighani@gmail.com

[2] Faculty of Engineering, Department of Electrical Engineering
Urmia University, Urmia, Iran
Akbari.telecom@gmail.com

[3] Department of Electrical Engineering, Songhor Branch
Islamic Azad University, Kermanshah- Iran
N.felegari@gmail.com

Abstract **─** In this letter, a rhombic monopole antenna with a parasitic rectangle into slot of the feed line is proposed to broaden impedance bandwidth. The antenna has a compact size with 19 × 16mm^2 which has been printed on a FR4 substrate with thickness of 1mm. The measurements show that the antenna has reflection coefficient better than -10dB from 2.9 up to 29GHz. Meanwhile, the measured patterns and gain are presented later in the paper.

Index Terms **─** Rhombic microstrip monopole antenna, super wide band (SWB), ultra wide band (UWB).

I. INTRODUCTION

On February 14, 2002, in the United States, the Federal Communications Commission (FCC) dedicated the 3.1-10.6GHz spectrum for commercial application of UWB technology [1]. The ultra-wideband (UWB) antenna is a key component of UWB technology and wireless communication. With the development of high-speed integrated circuits and the requirement of the miniaturization and integration, the research and application of UWB planar antennas have been growing rapidly.

The UWB technology creates constructive solutions for future wireless communication systems due to various advantages such as high immunity to multi path interference, small emission power and high data rate, large bandwidth, low cost for short range access and remote sensing applications. Various wideband antennas have been interesting subjects in antenna designs and have found important applications in military and civilian systems which can be mentioned to UWB and SWB.

There are two major differences between them; SWB antenna is a key component of electronic counterwork equipment in the information warfare; while the ultra-wideband (UWB) antenna is widely used in impulse radar and communication systems. Another difference is their actual frequency range; frequency range of an indoor UWB communication antenna is from 3.1 to 10.6GHz with a ratio bandwidth of 3.4:1, while ratio bandwidth of the SWB antenna is more than 10:1 [2].

Nowadays, various planar antennas with capability of SWB have been presented. SWB antennas must meet different requirements like broad impedance bandwidth, constant gain on desirable band, and small electrical size. With development of UWB and SWB technologies, the antennas have found different shapes such as rectangular, elliptical, triangular, polygonal, and fractal [3-14].

In this letter, a small rhombic monopole antenna with a novel microstrip feed-line for the

Submitted On: Oct 27, 2011
Accepted On: Jan 26, 2012

SWB application is proposed. The presented antenna with nearly low size and broad bandwidth was successfully fabricated. The measured results show acceptable agreement with the simulated results. The rest of the paper describes the antenna design in Section II. The discussion on results is presented in Section III, followed by conclusive comments in Section IV.

II. ANTENNA DESIGN

The geometrical configuration of the proposed antenna is depicted in Figure 1.

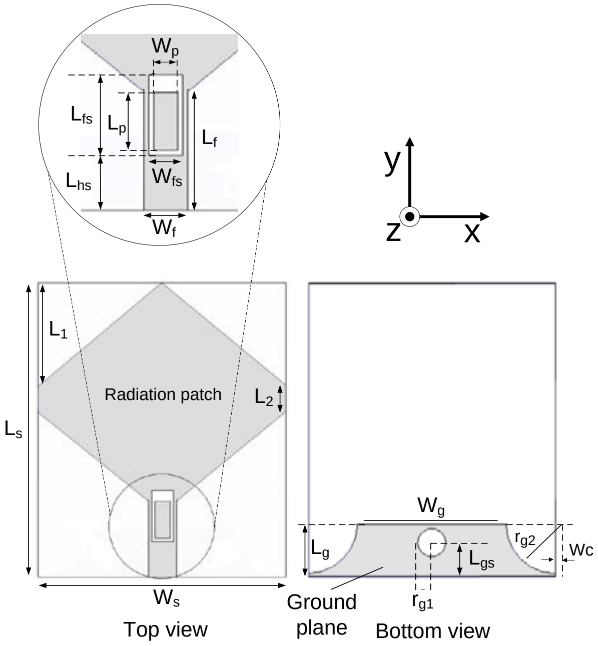

Fig. 1. Geometry of the antenna.

The parameters values are summarized in Table 1.

Table 1: Parametric values of the fabricated antenna (unit: mm)

W_s	L_s	L_1	L_2	W_c	L_f
16	19	6.67	1.64	0.3	5
W_{fs}	L_{fs}	L_{hs}	W_g	r_{g2}	L_g
1.4	3.3	2.3	10	3.2	3.4
W_f	W_p	L_p	r_{g1}	L_{gs}	ε_r
1.8	1	2.1	0.9	2.2	4.4

The antenna consists of a rhombic patch and a partial ground which there is a rectangular slot on the feed line and a circular slot on the ground, right behind the feed line. Meanwhile, there is a parasitic component in the rectangular slot that has effect on the bandwidth. The antenna has been printed on both sides of an FR4 microwave substrate with a thickness of 1 mm and dielectric constant of 4.4. The total size (L_s×W_s) of the proposed antenna is 19×16mm^2 which is almost compact. Note that the radiation patch is connected to the feed line with characteristic impedance 50 ohm which has a length and width of 5mm and 1.8 mm respectively. The proposed antenna is located in the x-y plane and the normal direction is parallel to the z-axis. It should be mentioned that the patch was rectangle basically, and then some modifications were performed on the rectangular patch, feed line, and ground plane. In order to increase the impedance bandwidth of the antenna, the following measures have been applied.

(a) Transforming the rectangular patch into a rhombic patch by etching four corners of the rectangle.
(b) Etching the upper corners of the ground in the form of a circular arc with radios of r_{g2}.
(c) Etching a circular slot with radios of r_{g1} from the ground plane.
(d) Etching a rectangular slot with width of W_{fs} and length of L_{fs} from the feed line.
(e) Adding a rectangular parasitic element with width of W_p and length of L_p into the rectangular slot in the feed line.

By selecting the optimal parameters mentioned in Table 1, the proposed antenna can be tuned to operate within the UWB and SWB bands. Figure 2 exhibits a photograph of the fabricated antenna.

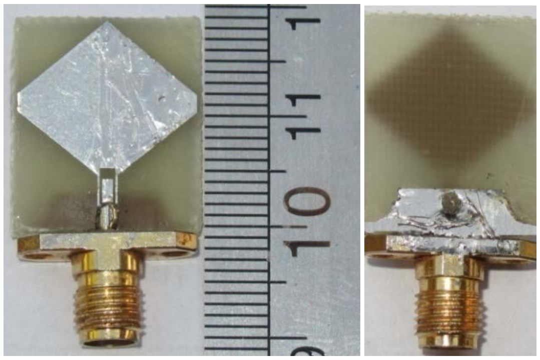

Fig. 2. Photograph of the fabricated antenna.

III. RESULTS AND DISCUSSION

In this section, simulated and measured results of the proposed rhombic monopole antenna are presented. Note that the simulated reflection coefficient results are obtained by using Ansoft HFSS11 [15]. As mentioned before, the proposed antenna used a novel technique to increase bandwidth. This technique uses a rectangular slot into the feed line which is caused to enhance the bandwidth of the middle and upper band. Figure 3 exhibits effect of the width of rectangular slot into the feed line on the reflection coefficient characteristics. If the reflection coefficient characteristics of the antennas #1 and #4 are compared with each other, it is exactly apparent that the band width of the proposed antenna from 7 up to 30GHz has been improved by this technique.

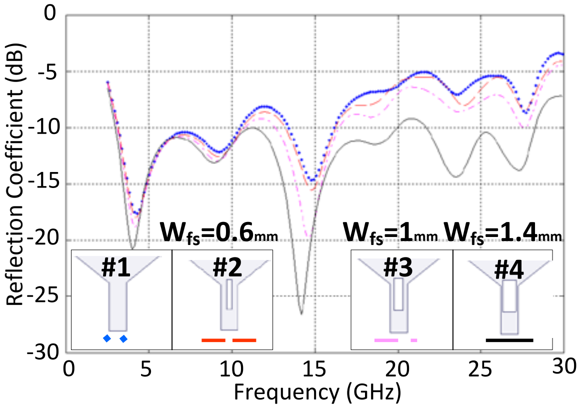

Fig. 3. Effect of the width of rectangular slot into the feed line on the reflection coefficient characteristics.

Another technique to increase the bandwidth for the upper band above 20GHz is by using a rectangle parasitic element in the rectangular slot of the feed line. As shown in Figure 4 with changing of the length of L_p the bandwidth of the proposed antenna from 22 up to 28GHz has been improved more than 5dB. The current distribution on the ground and patch of the proposed antenna at 6; the resonant frequencies is exhibited respectively in Figures 5 and 6. From Figure 5, we can conclude that three parts of the ground have an important role to create the resonances, which consist of the top edge of ground (W_g), circular arcs (r_{g2}), and around the circular slot. With regard to Figure 5 at all resonant frequencies except 9 GHz, width of the top edge of the ground (W_g) has a major effect. The most influence of the circular arc is at three frequencies of 9, 23.75, and 27.25GHz. Of course, this leads to confirm that the performance of the antenna is a bit dependent to the circular arc ratios of the ground plane, but it has a high depends to its width in the other words, the portion of the ground plane close to the patch acts as the part of the radiating structure [16, 17].

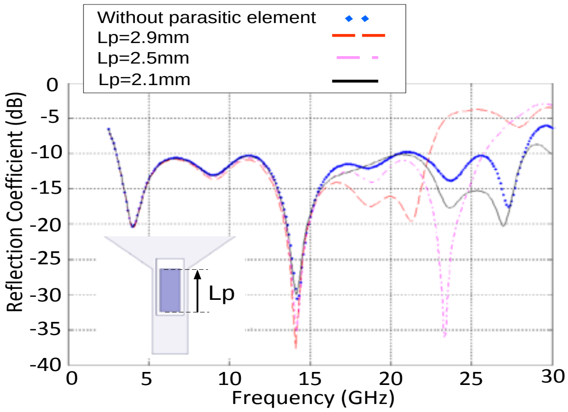

Fig. 4. Effect of the length of the parasitic rectangle (L_p) into rectangular slot on the reflection coefficient characteristics.

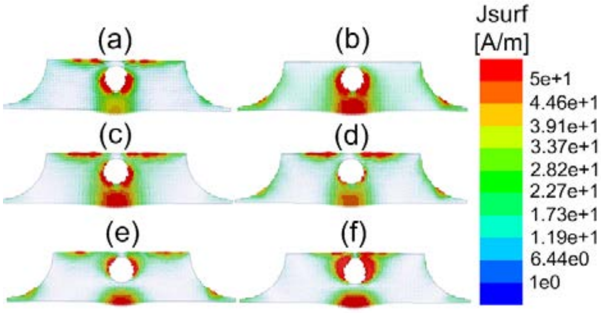

Fig. 5. Simulated current distribution on the ground at frequencies (a) 4GHz, (b) 9GHz, (c) 14.25GHz, (d) 18.5GHz, (e) 23.75GHz, (f) 27.25GHz.

However, it also leads to a disadvantage, i.e., when this type of antenna is integrated with printed circuit board, the RF circuit cannot be very close to the ground plane. Another point is that the existence of circular slot on the ground almost for all resonant frequencies is effective especially at frequencies of 9, 14.25, and 27.25GHz. The simulated current distributions on the patch at six resonant frequencies for the optimal design are presented in Figure 6. The current is mainly distributed along the edge of the rhombic patch, which indicates that the first resonant frequency is associated with the dimension of the rhombic patch. Its first resonance is about 4GHz, and the $2\times W_s/\lambda=0.22$ where λ is the wavelength corresponding to the first resonant frequency, lower than the determined that $2\times W_s/\lambda$ equivalent about 0.25 [18]. Other order harmonics of the antenna in Figure 6 is completely clear.

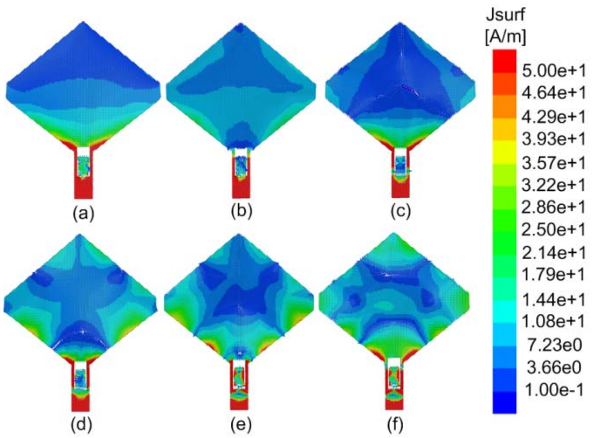

Fig. 6. Simulated current distribution on the patch at frequencies (a) 4GHz, (b) 9GHz, (c) 14.25GHz, (d) 18.5GHz, (d) 23.75GHz, (d) 27.25GHz.

The measured gain of the antenna is shown in Figure 7. The minimum gain is appeared at the initial frequencies due to the compact size of the antenna, but the maximum gain is between frequencies of 9 up to 10GHz with values of nearly 4.5dBi.

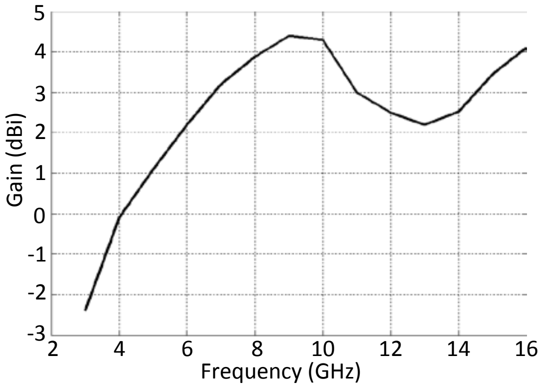

Fig.7. Measured gain of the proposed antenna.

The reflection coefficient of the antenna has been measured by using an Agilent E8363B network analyzer in its full operational span (50MHz - 40GHz). The results of measured and simulated reflection coefficient of the presented antenna are exhibited in Figure 8. The simulated results have been accomplished by the two software, HFSS and CST [19]. Regarding to Figure 8, the resonant frequencies have a good agreement with each other except initial band which its reason is being ideal of materials in CST simulator. The measured results also are almost similar to the expected results, so the results of the reflection coefficient are acceptable.

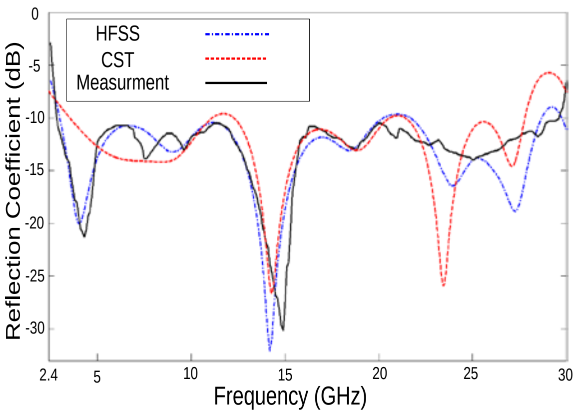

Fig.8. Simulated and measured reflection coefficient of the proposed antenna.

The key in the UWB antenna design is to obtain a good linearity of the phase of the radiated field because the antenna should be able to transmit the electrical pulse with minimal distortion. Usually, the group delay is used to evaluate the phase response of the transfer function because it is defined as the rate of change of the total phase shift with respect to angular frequency. Ideally, when the phase response is strictly linear, the group delay is constant.

$$group\ delay = -\frac{d\theta(w)}{dw}\,. \qquad (1)$$

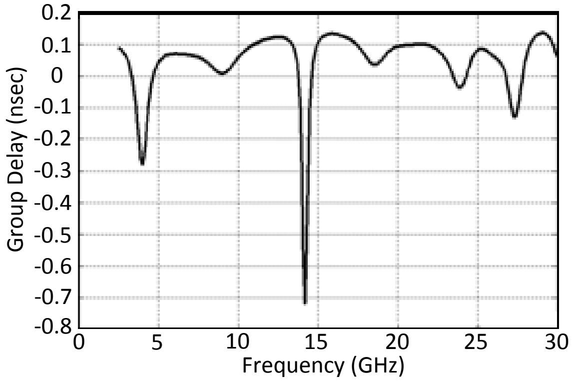

Fig. 9. Simulated group delay versus frequency for the proposed antenna.

As depicted from the Figure 9, the group delay variation of the proposed antennas at the resonant frequencies with respect to other frequencies is more. In spite of it, the group delay variation is less than 0.7ns over the frequency band from 2.5 up to 30GHz which ensure us pulse transmitted or received by the antenna will not distort seriously and will retain its shape. Therefore, the proposed antenna is suitable for modern UWB communication systems. The measured normalized radiation patterns at three frequencies of 3, 7, and 11GHz, respectively, in Figures 10 and 11 are exactly apparent. As was previously predicted, the pattern of the antenna in the H-plane is non-directional and it is nearly bi-directional in E-plane which is desirable.

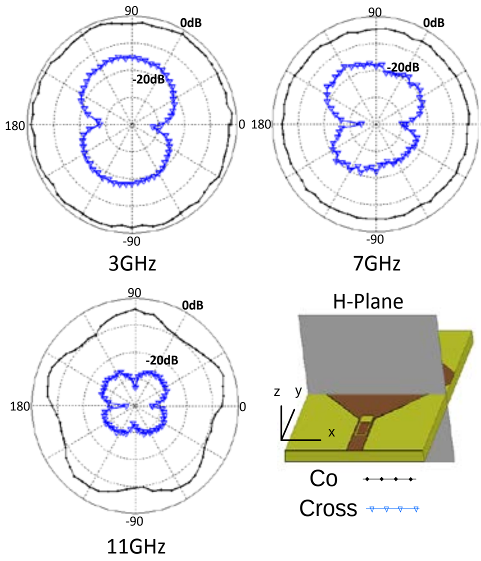

Fig.10. Measured normalized radiation patterns of the proposed antenna in H-plane.

IV. CONCLUSION

A new compact monopole microstrip antenna is proposed for the SWB and UWB applications. The proposed antenna consists of rhombic patch, partial ground, and microstrip feed-line which by using some techniques on the feed-line and ground, impedance bandwidth of the proposed antenna has been increased, in the other words; the bandwidth is from 2.9 up to 29GHz which confirms UWB and SWB characteristic of the antenna. The measurement indicates that the antenna radiation patterns are non directional in H-plane and almost bidirectional in E-plane. In addition, the antenna has nearly compact size of $19\times16\text{mm}^2$.

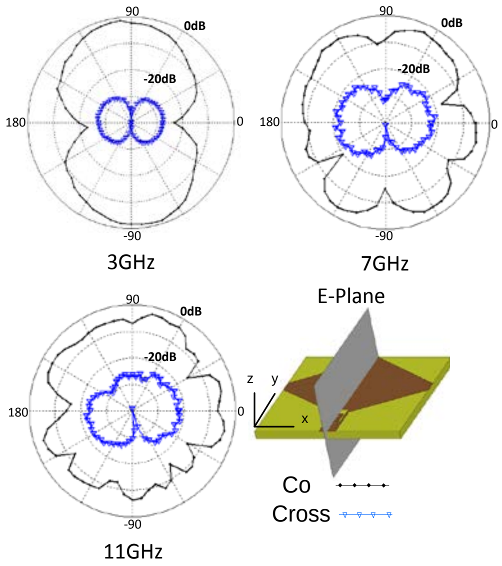

Fig.11. Measured normalized radiation pattern of the proposed antenna in E-plane.

REFERENCES

[1] Federal Communications Commission, First report and order: revision of part 15 of the commission's rules regarding ultra-wideband transmission systems, FCC 02-48, adopted February 2002, released April 2002.

[2] S. Zhong, X. Yan, and X. Liang "Compact UWB Planar Antenna Technology," *Electric and Electronic Engineering in China*, vol. 3, no. 2, pp. 136-144, 2008.

[3] X. R. Yan, S. S. Zhong, and G. Y. Wang, "Compact Hollowed Printed Monopole Antenna with Extremely Wide Bandwidth", *Microwave Opt Techn. Lett,* vol. 49, no. 11, pp. 2883-2886, Nov. 2007.

[4] Y. Dong, W. Hong, L. Liu, Y. Zhang, and Z. Kuai, "Performance Analysis of a Printed Super-Wideband Antenna," *Microwave Opt Techn. Lett*, vol. 51, no. 4, pp. 949-956, Apr. 2009.

[5] M. N. Srifi, O. El Mrabet, F. Falcone, M. S. Ayza, and M. Essaaidi, "A Novel Compact Printed Circular Antenna for Very Ultra Wideband Applications," *Microwave Opt Techn. Lett*, vol. 51, no. 4, pp.1130-1133, Apr. 2009.

[6] M. John and M. J. Ammann, "Optimization of the Impedance Bandwidth for the Printed Rectangular Monopole Antenna," *Microwave Opt. Techn. Lett*, vol. 47, no. 2, pp. 153-154, Oct. 2005.

[7] A. Azari, "Super Wideband Fractal Antenna Design," *IEEE MAPE*, Beijing, China, 2009.

[8] M. Koohestani and M. Golpour, "Very Ultra-Wideband Printed CPW-Fed Slot Antenna," *Electronics Letters*, vol. 45, no. 21, October 2009.

[9] A. Azari, "A New Ultra Wideband Fractal Monopole Antenna," *Applied Computational Electromagnetics Society (ACES) Journal*, vol. 26, no. 4, pp. 348 – 352, April 2011.

[10] E. Pittella, P. Bernardi, M. Cavagnaro, S. Pisa, and E. Piuzzi, "Design of UWB Antennas to Monitor Cardiac Activity," *Applied Computational Electromagnetics Society (ACES) Journal*, vol. 26, no. 4, pp. 267 – 274, April 2011.

[11] J. William and R. Nakkeeran, "A New UWB Slot Antenna with Rejection of WiMax and WLAN Bands," *Applied Computational Electromagnetics Society (ACES) Journal*, vol. 25, no. 9, pp. 787-793, September 2010.

[12] D. S. Javan and O. H. Ghouchani, "Cross Slot Antenna with U-Shaped Tuning Stub for Ultra Wideband Applications," *Applied Computational Electromagnetics Society (ACES) Journal*, vol. 24, no. 4, pp. 427-432, August 2009.

[13] M. Naghshvarian-Jahromi and N. Komjani-Barchloui, "Analysis of the Behavior of Sierpinski Carpet Monopole Antenna," *Applied Computational Electromagnetics Society (ACES) Journal*, vol. 24, no. 1, pp. 32-36, February 2009.

[14] R. Pillalamarri, J. R. Panda, and R. S. Kshetrimayum, "Printed UWB Circular and Modified Circular Disk Monopole Antennas," *International Journal of Recent Trends in Engineering*, iss. 1, vol. 1, pp. 12-15, May 2009.

[15] Ansoft HFSS User's manual, Ansoft Corporation, Beta Release 11.0, April 2007.

[16] J. Liang, C. C. Chiau, X. Chen, and C. G. Parini, "Analysis and Design of UWB Disc Monopole Antennas," in *Proc. Inst. Elect. Eng. Seminar on Ultra Wideband Communications Technologies and System Design*, Queen Mary, University of London, U.K., pp. 103-106, Jul. 2004.

[17] J. Liang, C. C. Chiau, X. Chen, and C. G. Parini "Printed Circular Disc Monopole Antenna for Ultra Wideband Applications," Electron. Lett., vol. 40, no. 20, pp. 1246-1247, Sep. 2004.

[18] J. Liang, L. Guo, C. C. Chiau, X. Chen, and C. G. Parini, "Study of CPW-Fed Circular Disc Monopole Antenna," *IEE Proceedings Microwaves, Antennas & Propagation*, vol. 152, no. 6, pp. 520-526, December 2005.

[19] CST Microwave studio, ver. 2008. Computer simulation technology, Framingham, MA, 2008.

Mojtaba Mighani was born in Mashhad, Iran, in September 23, 1983. He received B.Sc. degree in Electrical and Electronic Engineering from Aeronautical University, Tehran, Iran, in 2005 and M.Sc. degrees in Electrical and Telecommunication Engineering from KNTU university of technology, Tehran, Iran. He is currently working toward the Ph.D. degree in communication Engineering. Since 2007, he has taught courses in communication circuits, microwave engineering, antenna theory, and fields and waves in Aeronautical University, Tehran, Iran. His research interests include antenna theory, microwave active circuits and RF communication links.

Mohammad Akbari was born on February 3, 1983 in Tehran, Iran. He received his B.Sc. degree in Engineering- Telecommunication from University of Bahonar, Kerman, Iran, in 2007 and M.Sc. degrees in Electrical Engineering-Telecommunication from University of Urmia, Urmia, Iran, in 2011. His primary research interests are in antenna design, filters, and microwave components. Since 2011 He has taught courses in microwave engineering, antenna theory, and Fields & Waves, and electromagnetic in Aeronautical University, Tehran, Iran.

Nader Felegari was born in songhor,Iran 1984. He received his B.S. degree of Electrical Engineering and his M.S. degree of Communication Engineering from the Urmia University, Iran. His primary research interests are in antenna design.

2012 INSTITUTIONAL MEMBERS

DTIC-OCP LIBRARY
8725 John J. Kingman Rd, Ste 0944
Fort Belvoir, VA 22060-6218

AUSTRALIAN DEFENCE LIBRARY
Northcott Drive
Canberra, A.C.T. 2600 Australia

BEIJING BOOK CO, INC
701 E Linden Avenue
Linden, NJ 07036-2495

DARTMOUTH COLLEGE
6025 Baker/Berry Library
Hanover, NH 03755-3560

DSTO EDINBURGH
AU/33851-AP, PO Box 830470
Birmingham, AL 35283

SIMEON J. EARL – BAE SYSTEMS
W432A, Warton Aerodome
Preston, Lancs., UK PR4 1AX

ENGINEERING INFORMATION, INC
PO Box 543
Amsterdam, Netherlands 1000 Am

ETSE TELECOMUNICACION
Biblioteca, Campus Lagoas
Vigo, 36200 Spain

GA INSTITUTE OF TECHNOLOGY
EBS-Lib Mail code 0900
74 Cherry Street
Atlanta, GA 30332

TIMOTHY HOLZHEIMER
Raytheon
PO Box 1044
Rockwall, TX 75087

HRL LABS, RESEARCH LIBRARY
3011 Malibu Canyon
Malibu, CA 90265

IEE INSPEC
Michael Faraday House
6 Hills Way
Stevenage, Herts UK SG1 2AY

INSTITUTE FOR SCIENTIFIC INFO.
Publication Processing Dept.
3501 Market St.
Philadelphia, PA 19104-3302

LIBRARY – DRDC OTTAWA
3701 Carling Avenue
Ottawa, Ontario, Canada K1A OZ4

LIBRARY of CONGRESS
Reg. Of Copyrights
Attn: 407 Deposits
Washington DC, 20559

LINDA HALL LIBRARY
5109 Cherry Street
Kansas City, MO 64110-2498

MISSOURI S&T
400 W 14th Street
Rolla, MO 56409

MIT LINCOLN LABORATORY
Periodicals Library
244 Wood Street
Lexington, MA 02420

NATIONAL CHI NAN UNIVERSITY
Lily Journal & Book Co, Ltd
20920 Glenbrook Drive
Walnut, CA 91789-3809

JOHN NORGARD
UCCS
20340 Pine Shadow Drive
Colorado Springs, CO 80908

OSAMA MOHAMMED
Florida International University
10555 W Flagler Street
Miami, FL 33174

NAVAL POSTGRADUATE SCHOOL
Attn:J. Rozdal/411 Dyer Rd./ Rm 111
Monterey, CA 93943-5101

NDL KAGAKU
C/0 KWE-ACCESS
PO Box 300613 (JFK A/P)
Jamaica, NY 11430-0613

OVIEDO LIBRARY
PO BOX 830679
Birmingham, AL 35283

DAVID PAULSEN
E3Compliance
1523 North Joe Wilson Road
Cedr Hill, TX 75104-1437

PENN STATE UNIVERSITY
126 Paterno Library
University Park, PA 16802-1808

DAVID J. PINION
1122 E Pike Street #1217
SEATTLE, WA 98122

KATHERINE SIAKAVARA
Gymnasiou 8
Thessaloniki, Greece 55236

SWETS INFORMATION SERVICES
160 Ninth Avenue, Suite A
Runnemede, NJ 08078

YUTAKA TANGE
Maizuru Natl College of Technology
234 Shiroya
Maizuru, Kyoto, Japan 625-8511

TIB & UNIV. BIB. HANNOVER
DE/5100/G1/0001
Welfengarten 1B
Hannover, Germany 30167

UEKAE
PO Box 830470
Birmingham, AL 35283

UNIV OF CENTRAL FLORIDA
4000 Central Florida Boulevard
Orlando, FL 32816-8005

UNIVERSITY OF COLORADO
1720 Pleasant Street, 184 UCB
Boulder, CO 80309-0184

UNIVERSITY OF KANSAS – WATSON
1425 Jayhawk Blvd 210S
Lawrence, KS 66045-7594

UNIVERSITY OF MISSISSIPPI
JD Williams Library
University, MS 38677-1848

UNIVERSITY LIBRARY/HKUST
Clear Water Bay Road
Kowloon, Honk Kong

CHUAN CHENG WANG
8F, No. 31, Lane 546
MingCheng 2nd Road, Zuoying Dist
Kaoshiung City, Taiwan 813

THOMAS WEILAND
TU Darmstadt
Schlossgartenstrasse 8
Darmstadt, Hessen, Germany 64289

STEVEN WEISS
US Army Research Lab
2800 Powder Mill Road
Adelphi, MD 20783

YOSHIHIDE YAMADA
NATIONAL DEFENSE ACADEMY
1-10-20 Hashirimizu
Yokosuka, Kanagawa,
Japan 239-8686

APPLIED COMPUTATIONAL ELECTROMAGNETICS SOCIETY JOURNAL
http://aces.ee.olemiss.edu

INFORMATION FOR AUTHORS

PUBLICATION CRITERIA

Each paper is required to manifest some relation to applied computational electromagnetics. **Papers may address general issues in applied computational electromagnetics, or they may focus on specific applications, techniques, codes, or computational issues.** While the following list is not exhaustive, each paper will generally relate to at least one of these areas:

1. **Code validation.** This is done using internal checks or experimental, analytical or other computational data. Measured data of potential utility to code validation efforts will also be considered for publication.

2. **Code performance analysis.** This usually involves identification of numerical accuracy or other limitations, solution convergence, numerical and physical modeling error, and parameter tradeoffs. However, it is also permissible to address issues such as ease-of-use, set-up time, run time, special outputs, or other special features.

3. **Computational studies of basic physics.** This involves using a code, algorithm, or computational technique to simulate reality in such a way that better, or new physical insight or understanding, is achieved.

4. **New computational techniques** or new applications for existing computational techniques or codes.

5. **"Tricks of the trade"** in selecting and applying codes and techniques.

6. **New codes, algorithms, code enhancement, and code fixes.** This category is self-explanatory, but includes significant changes to existing codes, such as applicability extensions, algorithm optimization, problem correction, limitation removal, or other performance improvement. **Note: Code (or algorithm) capability descriptions are not acceptable, unless they contain sufficient technical material to justify consideration.**

7. **Code input/output issues.** This normally involves innovations in input (such as input geometry standardization, automatic mesh generation, or computer-aided design) or in output (whether it be tabular, graphical, statistical, Fourier-transformed, or otherwise signal-processed). Material dealing with input/output database management, output interpretation, or other input/output issues will also be considered for publication.

8. **Computer hardware issues.** This is the category for analysis of hardware capabilities and limitations of various types of electromagnetics computational requirements. Vector and parallel computational techniques and implementation are of particular interest.

Applications of interest include, but are not limited to, antennas (and their electromagnetic environments), networks, static fields, radar cross section, inverse scattering, shielding, radiation hazards, biological effects, biomedical applications, electromagnetic pulse (EMP), electromagnetic interference (EMI), electromagnetic compatibility (EMC), power transmission, charge transport, dielectric, magnetic and nonlinear materials, microwave components, MEMS, RFID, and MMIC technologies, remote sensing and geometrical and physical optics, radar and communications systems, sensors, fiber optics, plasmas, particle accelerators, generators and motors, electromagnetic wave propagation, non-destructive evaluation, eddy currents, and inverse scattering.

Techniques of interest include but not limited to frequency-domain and time-domain techniques, integral equation and differential equation techniques, diffraction theories, physical and geometrical optics, method of moments, finite differences and finite element techniques, transmission line method, modal expansions, perturbation methods, and hybrid methods.

Where possible and appropriate, authors are required to provide statements of quantitative accuracy for measured and/or computed data. This issue is discussed in "Accuracy & Publication: Requiring, quantitative accuracy statements to accompany data," by E. K. Miller, *ACES Newsletter,* Vol. 9, No. 3, pp. 23-29, 1994, ISBN 1056-9170.

SUBMITTAL PROCEDURE

All submissions should be uploaded to ACES server through ACES web site (http://aces.ee.olemiss.edu) by using the upload button, journal section. Only pdf files are accepted for submission. The file size should not be larger than 5MB, otherwise permission from the Editor-in-Chief should be obtained first. Automated acknowledgment of the electronic submission, after the upload process is successfully completed, will be sent to the corresponding author only. It is the responsibility of the corresponding author to keep the remaining authors, if applicable, informed. Email submission is not accepted and will not be processed.

EDITORIAL REVIEW

In order to ensure an appropriate level of quality control, papers are peer reviewed. They are reviewed both for technical correctness and for adherence to the listed guidelines regarding information content and format.

PAPER FORMAT

Only camera-ready electronic files are accepted for publication. The term **"camera-ready" means that the material is neat, legible, reproducible, and in accordance with the final version format listed below.**

The following requirements are in effect for the final version of an ACES Journal paper:

1. The paper title should not be placed on a separate page.

The title, author(s), abstract, and (space permitting) beginning of the paper itself should all be on the first page. The title, author(s), and author affiliations should be centered (center-justified) on the first page. The title should be of font size 16 and bolded, the author names should be of font size 12 and bolded, and the author affiliation should be of font size 12 (regular font, neither italic nor bolded).

2. An abstract is required. The abstract should be a brief summary of the work described in the paper. It should state the computer codes, computational techniques, and applications discussed in the paper (as applicable) and should otherwise be usable by technical abstracting and indexing services. The word "Abstract" has to be placed at the left margin of the paper, and should be bolded and italic. It also should be followed by a hyphen (—) with the main text of the abstract starting on the same line.

3. All section titles have to be centered and all the title letters should be written in caps. The section titles need to be numbered using roman numbering (I. II. ….)

4. Either British English or American English spellings may be used, provided that each word is spelled consistently throughout the paper.

5. Internal consistency of references format should be maintained. As a guideline for authors, we recommend that references be given using numerical numbering in the body of the paper (with numerical listing of all references at the end of the paper). The first letter of the authors' first name should be listed followed by a period, which in turn, followed by the authors' complete last name. Use a coma (,) to separate between the authors' names. Titles of papers or articles should be in quotation marks (" "), followed by the title of journal, which should be in italic font. The journal volume (vol.), issue number (no.), page numbering (pp.), month and year of publication should come after the journal title in the sequence listed here.

6. Internal consistency shall also be maintained for other elements of style, such as equation numbering. Equation numbers should be placed in parentheses at the right column margin. All symbols in any equation have to be defined before the equation appears or right immediately following the equation.

7. The use of SI units is strongly encouraged. English units may be used as secondary units (in parentheses).

8. Figures and tables should be formatted appropriately (centered within the column, side-by-side, etc.) on the page such that the presented data appears close to and after it is being referenced in the text. When including figures and tables, all care should be taken so that they will appear appropriately when printed in black and white. For better visibility of paper on computer screen, it is good to make color figures with different line styles for figures with multiple curves. Colors should also be tested to insure their ability to be distinguished after black and white printing. Avoid the use of large symbols with curves in a figure. It is always better to use different line styles such as solid, dotted, dashed, etc.

9. A figure caption should be located directly beneath the corresponding figure, and should be fully justified.

10. The intent and meaning of all text must be clear. For authors who are not masters of the English language, the ACES Editorial Staff will provide assistance with grammar (subject to clarity of intent and meaning). However, this may delay the scheduled publication date.

11. Unused space should be minimized. Sections and subsections should not normally begin on a new page.

ACES reserves the right to edit any uploaded material, however, this is not generally done. It is the author(s) responsibility to provide acceptable camera-ready files in pdf and MSWord formats. Incompatible or incomplete files will not be processed for publication, and authors will be requested to re-upload a revised acceptable version.

COPYRIGHTS AND RELEASES

Each primary author must execute the online copyright form and obtain a release from his/her organization vesting the copyright with ACES. Both the author(s) and affiliated organization(s) are allowed to use the copyrighted material freely for their own private purposes.

Permission is granted to quote short passages and reproduce figures and tables from and ACES Journal issue provided the source is cited. Copies of ACES Journal articles may be made in accordance with usage permitted by Sections 107 or 108 of the U.S. Copyright Law. This consent does not extend to other kinds of copying, such as for general distribution, for advertising or promotional purposes, for creating new collective works, or for resale. The reproduction of multiple copies and the use of articles or extracts for commercial purposes require the consent of the author and specific permission from ACES. Institutional members are allowed to copy any ACES Journal issue for their internal distribution only.

PUBLICATION CHARGES

All authors are allowed for 8 printed pages per paper without charge. Mandatory page charges of $75 a page apply to all pages in excess of 8 printed pages. Authors are entitled to one, free of charge, copy of the printed journal issue in which their paper was published. Additional reprints are available for $ 50. Requests for additional re-prints should be submitted to the managing editor or ACES Secretary.

Corresponding author is required to complete the online form for the over page charge payment right after the initial acceptance of the paper is conveyed to the corresponding author by email.

ACES Journal is abstracted in INSPEC, in Engineering Index, DTIC, Science Citation Index Expanded, the Research Alert, and to Current Contents/Engineering, Computing & Technology.